UNIVERSIDADE ESTADUAL DE CAMPINAS
INSTITUTO DE MATEMÁTICA, ESTATÍSTICA E
COMPUTAÇÃO CIENTÍFICA
DEPARTAMENTO DE MATEMÁTICA APLICADA

TESE DE DOUTORADO

Caos em sistemas abertos e gravitação

Autor: ADILSON ENIO MOTTER
Orientador: PROF. DR. PATRICIO ANÍBAL LETELIER SOTOMAYOR

Título: Caos em sistemas abertos e gravitação.

Este exemplar corresponde à redação final da tese devidamente corrigida e defendida por **Adilson Enio Motter** e aprovada pela comissão julgadora.

Campinas, 1 de março de 2002.

Prof. Dr. Patricio Aníbal Letelier Sotomayor
Orientador

Banca Examinadora:
Prof. Dr. Patricio Aníbal Letelier Sotomayor (orientador) - IMECC/UNICAMP
Prof. Dr. Alberto Vazquez Saa - IMECC/UNICAMP
Prof. Dr. Celso Grebogi - IF/USP
Prof. Dr. George Emanuel Avraam Matsas - IFT/UNESP
Prof. Dr. Gerson Francisco - IFT/UNESP
Prof. Dr. Samuel Rocha de Oliveira (suplente) - IMECC/UNICAMP
Profa. Dra. Kyoko Furuya (suplente) - IFGW/UNICAMP

Tese apresentada ao Instituto de Matemática, Estatística e Computação Científica, Unicamp, como requisito parcial para a obtenção do Título de Doutor em Matemática Aplicada.

Tese de Doutorado defendida em 1 de março de 2002
e aprovada pela Banca Examinadora composta pelos seguintes professores:

Prof. Dr. Patricio Aníbal Letelier Sotomayor

Prof. Dr. Alberto Vazquez Saa

Prof. Dr. Celso Grebogi

Prof. Dr. George Emanuel Avraam Matsas

Prof. Dr. Gerson Francisco

Nunca perder de vista o gráfico de uma vida humana, que não se compõe,
digam o que disserem, de uma horizontal e duas perpendiculares,
mas de três linhas sinuosas, prolongadas até o infinito,
incessantemente reaproximadas e divergindo sem cessar...
Marguerite Yourcenar, Memórias de Adriano

Dedico esta tese à Luciana.

Agradecimentos

Agradeço,

em primeiro lugar, ao Prof. Dr. Patricio Letelier a orientação, na acepção plena da palavra, e ao Prof. Dr. Ying-Cheng Lai a colaboração e financiamento nos EUA;

aos Profs. Drs. André Ribeiro, Márcio Rosa, Marco Antônio, Marcus de Aguiar e Renato Pedrosa, bem como aos Profs. Drs. que compuseram a banca examinadora, as sugestões e referências;

ao Instituto de Matemática Estatística e Computação Científica, que através do seu diretor, prof. Dr. José Boldrini, e do seu coordenador de pós-graduação, prof. Dr. José Martinez, tornou possível a realização deste projeto;

aos pós-doutorandos Alessandro, Eduardo e Takashi as colaborações e conversas inspiradoras; ao Alessandro também a hospitalidade em Tempe;

aos colegas Alexandre Fontes, Luiz Alberto, Luis Gregório, Mauricio, Maximiliano e Rafael as discussões estimulantes;

aos funcionários dos Institutos de Física e Matemática, em especial à Fátima e ao Márcio, o pronto atendimento às nossas necessidades;

por fim, à Fapesp e à minha família o apoio financeiro e não financeiro, respectivamente.

Resumo

Estudamos a formação de emaranhados homoclínicos em movimentos geodésicos associados a órbitas não limitadas de potenciais do tipo monopólo mais quadrupólo. Analisamos a dinâmica de espalhamentos caóticos, onde consideramos métodos para o cálculo de dimensões fractais, leis de escala em bifurcações topológicas e efeitos de pequenas dissipações em processos não hiperbólicos. Introduzimos técnicas para o estudo do caos a partir de transientes caóticos. Investigamos a natureza invariante, por reparametrizações temporais, do caos em cosmologias mixmaster (Bianchi IX) e da não integrabilidade em cosmologias de Friedmann-Robertson-Walker.

Abstract

Homoclinic crossings are studied in geodesic motions associated with unbounded orbits of monopole plus quadrupolelike potencials. The dynamics of chaotic scatterings is analyzed: we consider methods to compute fractal dimensions, scaling laws in topological bifurcations, and effects of small dissipations in nonhyperbolic processes. Techniques to study chaos, based on the analysis of chaotic transients, are introduced. The invariant nature of chaos in mixmaster cosmologies (Bianchi IX) and nonintegrability in Friedmann-Robertson-Walker cosmologies is investigated under time reparametrizations.

Sumário

Introdução **3**

1 Elementos de sistemas dinâmicos **7**

1.1 Sistemas Hamiltonianos 7

1.2 Caos em sistemas fechados 18

1.3 Caos em sistemas abertos 23

2 Elementos de relatividade geral **29**

2.1 Equações da relatividade geral 29

2.2 Cosmologia relativística 32

2.3 Caos nas equações de Einstein e da geodésica 38

3 Caos em sistemas abertos e gravitação **41**

3.1 Emaranhados homoclínicos em sistemas abertos 41

3.2 Espalhamento caótico 43

3.3 Fractais em sistemas abertos × caos em sistemas fechados 46

3.4 Caos em cosmologia 47

Conclusão **51**

A Homoclinic crossing in open systems:
Chaos in periodically perturbed monopole + quadrupolelike potentials 59

B Hausdorff dimension of repellers
in low sensitive systems 79

C Cusp-scaling behavior in fractal dimension
of chaotic scattering 89

D Dissipative chaotic scattering 101

E Arbitrariness in defining fractal basins:
Relations between open and closed systems 111

F A fractal method for chaos
in conservative closed systems of several dimensions 131

G Mixmaster chaos 143

H FRW cosmologies between chaos and integrability 155

Introdução

O estudo do problema de três corpos em mecânica celeste levou Poincaré à descoberta, no final do século XIX, do caos em fenômenos homoclínicos [1]. Desde então foram estudados inúmeros sistemas que apresentam comportamento caótico, e acredita-se hoje que, em sistemas dinâmicos, caos seja a regra e não a exceção. Como conseqüência, caos tem se tornado uma área multidisciplinar de crescente interesse em disciplinas tão diversas como engenharia, biologia, economia, química e ciências sociais [2]. Em física, uma área particularmente influenciada por estes avanços é a física estatística [3].

Depois de Poincaré, problemas de gravitação continuaram a contribuir de forma significativa para a compreensão da complicada dinâmica dos sistemas caóticos. Exemplos são os influentes trabalhos de Hénon e Heiles no modelamento de galáxias [4] e de Laskar no estudo do sistema solar [5]. A dinâmica da relatividade geral é intrinsecamente não linear, e como tal é extremamente rica. É natural, portanto, investigar a existência, natureza e implicações do caos neste contexto. Esta é uma linha recente de pesquisa e apresenta muito interesse tanto do ponto de vista físico quanto matemático [6].

Nesta tese estudamos caos *clássico* (não quântico) em sistemas *abertos* (movimentos não confinados a uma região finita do espaço de fase), contextualizado principalmente em cosmologia e em problemas astrofísicos de gravitação newtoniana e relatividade geral. Para tanto usamos, entre outras, técnicas fractais de espalhamento caótico. Como conseqüência alguns dos resultados centrais do nosso trabalho dizem respeito exclusivamente a espalhamento caótico. Em gravitação newtoniana consideramos questões que, apesar do longo histórico de pesquisa na área, continuavam não respondidas mesmo para sistemas tão simples como o problema de Kepler perturbado. Em relatividade geral e cosmologia, o problema central que analisamos diz respeito à aparente incompatibilidade entre caos e teorias invariantes por mudanças de coordenadas espaço-*temporais*. Neste contexto, devido à inexistência de um tempo absoluto, têm sido ambíguas as respostas à fundamental questão de se determinado sistema é caótico ou não. Desmistificamos este problema e, em particular, mostramos que o paradigmático modelo cosmológico mixmaster é mesmo caótico.

A apresentação está dividida em duas partes. A primeira, formada pelos Capítulos 1 e 2, é uma introdução de caráter monográfico a sistemas dinâmicos e relatividade geral. A segunda, composta do Capítulo 3 e dos Apêndices A-H, consiste dos resultados originais da tese. Os Apêndices são reproduções de artigos publicados ou submetidos para publicação em periódicos internacionais. O Capítulo 3 traz uma discussão dos principais resultados e implicações destes trabalhos.

No Capítulo 1, apresentamos conceitos básicos de sistemas dinâmicos e técnicas para o estudo do caos. Consideramos questões como integrabilidade e caos em sistemas abertos e fechados, em particular em sistemas hamiltonianos. Discutimos o teorema KAM, seções de Poincaré, teorema de Smale-Birkhoff, método de Melnikov, expoentes de Lyapunov, conjuntos fractais, espalhamento caótico etc. No segundo Capítulo, introduzimos elementos básicos de relatividade geral e cosmologia matemática. Apresentamos as equações fundamentais da relatividade geral e discutimos a classificação de Bianchi das cosmologias espacialmente homogêneas, bem como os modelos cosmológicos de Friedmann-Robertson-Walker. Introduzimos o problema do caos neste contexto e apresentamos uma breve revisão de trabalhos anteriores. Analisamos os casos em que a dinâmica é determinada pela equação da geodésica, como em movimentos de partículas numa dada geometria, e pelas equações de Einstein, como na evolução de modelos cosmológicos.

No Apêndice A, estudamos a formação de emaranhados homoclínicos associados a órbitas não ligadas de potenciais gravitacionais. Analisamos perturbações periódicas de potenciais do tipo monopólo mais quadrupólo. Classicamente estes sistemas modelam o movimento de partículas em torno de centros atratores deformados, como estrelas e galáxias. Em relatividade geral, modelam partículas-teste em torno de um buraco negro de Schwarzschild. Compactamos a parte relevante do espaço de fase com a introdução de coordenadas adequadas. Estudamos as equações resultantes através do método de Melnikov e do teorema homoclínico de Smale-Birkhoff – os quais observamos continuarem válidos apesar da não hiperbolicidade do ponto fixo homoclínico – e do método de seções de Poincaré.

Nos Apêndices B, C e D, consideramos problemas de espalhamento caótico. Discutimos métodos para calcular a dimensão de repelores em sistemas com três ou mais graus de liberdade cujo conjunto invariante futuro tem codimensão maior que um. Neste caso, o método usual de incertezas não se aplica. Estudamos também o comportamento da dimensão do conjunto invariante em bifurcações topológicas de sistemas com dois e três graus de liberdade. Obtemos uma lei de escala e mostramos que, como função da energia, a dimensão apresenta um mínimo em forma de *cusp* no ponto de bifurcação. Por fim, investigamos espalhamento caótico em regime dissipativo. Mostramos que a dinâmica de processos não hiperbólicos sofre uma metamorfose quando sujeita a pequenas dissipações típicas de sistemas reais.

Nos Apêndices E e F, analisamos relações entre a existência de caos num sistema fechado e a presença de estruturas fractais num sistema aberto associado. Para tanto, o sistema aberto é definido a partir do sistema fechado pela introdução de saídas ou regiões de escape. Observamos que conjuntos invariantes fractais em geral implicam em dinâmica caótica no sistema original e podem, portanto, ser usados como indicadores de caos. Esta observação é o ponto de partida para a implementação de um método capaz de localizar regiões caóticas em sistemas conservativos com três ou mais graus de liberdade. Esta técnica é manifestamente invariante por troca de coordenadas espaço-temporais, o que a torna viável em sistemas relativísticos.

Nos Apêndices G e H, estudamos o problema do caos em cosmologia. Consideramos o sistema mixmaster, que tem servido como modelo para um intenso debate sobre a não invariança do caos nas equações de Einstein. Usando uma variação da técnica discutida no Apêndice F, mostramos que o sistema é de fato caótico em relação a qualquer escolha de coordenadas. Estudamos também a cosmologia fechada de Friedmann-Robertson-Walker conformemente acoplada a um campo escalar massivo, para a qual resultados conflitantes haviam sido encontrados em relação a diferentes parâmetros temporais. Mostramos que, qualquer que seja a parametrização temporal, o sistema é não caótico, porém, não integrável. Estes resultados podem ser conciliados com a não invariança dos expoentes de Lyapunov, que é a origem da polêmica em relação a não invariança do caos em cosmologia.

Concluímos que, quando satisfeitas as hipóteses necessárias para que os expoentes de Lyapunov sejam interpretáveis como indicadores de caos, expoentes positivos devem permanecer positivos sob reparametrizações espaço-temporais. Portanto, diferentemente do que se acreditava, caos é uma propriedade do sistema físico, e não do sistema de coordenadas, também em relatividade geral.

1

Elementos de sistemas dinâmicos

Muitas vezes em física tratamos de problemas modelados por sistemas de equações da forma

$$\frac{d\boldsymbol{x}}{dt} = \boldsymbol{F}(\boldsymbol{x}, t), \tag{1.1}$$

onde $\boldsymbol{x} = (x_1, x_2, ..., x_m)$ e $\boldsymbol{F} = (F_1, F_2, ..., F_m)$, ou por mapas da forma

$$\boldsymbol{y}^{(k+1)} = \boldsymbol{M}(\boldsymbol{y}^{(k)}), \tag{1.2}$$

onde $\boldsymbol{y} = (y_1, y_2, ..., y_m)$ e $\boldsymbol{M} = (M_1, M_2, ..., M_m)$, os quais constituem objetos de estudo de *sistemas dinâmicos*. Neste Capítulo apresentamos conceitos básicos de caos em sistemas dinâmicos. As principais referências são [7, 8, 9, 10, 11].

1.1 Sistemas Hamiltonianos

Os sistemas hamiltonianos correspondem ao caso particular de (1.1) em que $m = 2n$ e existem coordenadas $\boldsymbol{x} = (\boldsymbol{q}, \boldsymbol{p})$ tais que

$$\boldsymbol{F} = (\boldsymbol{\nabla}_{\boldsymbol{p}} H, -\boldsymbol{\nabla}_{\boldsymbol{q}} H), \tag{1.3}$$

para uma certa função $H = H(\boldsymbol{q}, \boldsymbol{p}, t)$, onde $\boldsymbol{q} = (q_1, q_2, ..., q_n)$ e $\boldsymbol{p} = (p_1, p_2, ..., p_n)$. Apesar da severa restrição imposta a $\boldsymbol{F}$, a Eq. (1.3) representa uma vasta classe de sistemas fisicamente interessantes, incluindo a mecânica clássica não dissipativa, da qual tomamos emprestada boa parte da nomenclatura aqui empregada.

O espaço das coordenadas $\boldsymbol{x}$ é o espaço de fase, $\boldsymbol{q}$ são as coordenadas generalizadas, $\boldsymbol{p}$ são os momenta generalizados, n é o número de graus de liberdade e H é a função hamiltoniana. Quando $\boldsymbol{F}$ é definida pela relação (1.3), a Eq. (1.1) se reduz às equações de Hamilton. Variáveis dinâmicas $\boldsymbol{q}$ e $\boldsymbol{p}$ que se relacionam através das equações de Hamilton são ditas canônicas.

Transformações entre pares de coordenadas canônicas são chamadas transformações canônicas. Estas podem ser feitas de forma sistemática a partir de funções geratrizes. Um exemplo de função geratriz é $S = S(\boldsymbol{q}, \bar{\boldsymbol{p}}, t)$, a qual define a transformação $(\boldsymbol{q}, \boldsymbol{p}) \rightarrow (\bar{\boldsymbol{q}}, \bar{\boldsymbol{p}})$ dada implicitamente por

$$\bar{\boldsymbol{q}} = \boldsymbol{\nabla}_{\bar{\boldsymbol{p}}} S(\boldsymbol{q}, \bar{\boldsymbol{p}}, t), \quad \boldsymbol{p} = \boldsymbol{\nabla}_{\boldsymbol{q}} S(\boldsymbol{q}, \bar{\boldsymbol{p}}, t). \tag{1.4}$$

As Eqs. (1.4) podem ser resolvidas para $\boldsymbol{q}$ e $\boldsymbol{p}$, tal que a hamiltoniana passa a ser escrita como

$$\bar{H}(\bar{\boldsymbol{q}}, \bar{\boldsymbol{p}}, t) = H(\boldsymbol{q}(\bar{\boldsymbol{q}}, \bar{\boldsymbol{p}}, t), \boldsymbol{p}(\bar{\boldsymbol{q}}, \bar{\boldsymbol{p}}, t), t) + \frac{\partial}{\partial t} S(\boldsymbol{q}(\bar{\boldsymbol{q}}, \bar{\boldsymbol{p}}, t), \bar{\boldsymbol{p}}, t). \tag{1.5}$$

Na formulação canônica, volumes do espaço de fase são preservados sob evolução temporal, o que segue de $\boldsymbol{\nabla}_{\boldsymbol{x}} \cdot \boldsymbol{F} = 0$. Este resultado, conhecido como teorema de Liouville, tem várias implicações. Uma delas é a ausência de atratores no espaço de fase. Outra é o teorema de recorrência de Poincaré. Quando H não depende explicitamente do tempo e todas as órbitas estão limitadas a uma região finita do espaço de fase, este teorema afirma que: sob evolução temporal, alguns dos pontos de uma pequena região de volume V do espaço de fase necessariamente retornam ao volume inicial a tempos suficientemente longos, qualquer que seja V.

Uma função das variáveis dinâmicas que não depende explicitamente do tempo, $f = f(\boldsymbol{q}, \boldsymbol{p})$, é uma integral de movimento se permanecer constante ao longo das trajetórias, ou seja,

$$\frac{d}{dt} f(\boldsymbol{q}(t), \boldsymbol{p}(t)) = 0. \tag{1.6}$$

No espaço de fase, os conjuntos de nível de uma integral de movimento, $f(\boldsymbol{q},\boldsymbol{p})=$ cte, definem superfícies de dimensão $2n-1$ às quais as órbitas ficam confinadas. As integrais de movimento $\{f_1, f_2, ..., f_k\}$ são ditas independentes se os vetores normais $\{\boldsymbol{\nabla}_{\boldsymbol{x}}f_1, \boldsymbol{\nabla}_{\boldsymbol{x}}f_2, ...,$ $\boldsymbol{\nabla}_{\boldsymbol{x}}f_k\}$ são linearmente independentes. Quando o sistema possui k integrais de movimento independentes, as trajetórias ficam confinadas à interseção de k superfícies transversais, restringindo o movimento a uma superfície $(2n-k)$-dimensional. Se H não depende explicitamente do tempo, a própria hamiltoniana mantém-se constante – igual à constante de energia E – e o sistema é conservativo. Por ora nos concentramos neste caso.

O problema de encontrar soluções gerais de um sistema hamiltoniano pode ser reestabelecido como o de encontrar uma transformação canônica $(\boldsymbol{q},\boldsymbol{p})=(\boldsymbol{q}(\bar{\boldsymbol{q}},\bar{\boldsymbol{p}}),\boldsymbol{p}(\bar{\boldsymbol{q}},\bar{\boldsymbol{p}}))$ que leve $H(\boldsymbol{q},\boldsymbol{p})$ a uma hamiltoniana $\bar{H}=\bar{H}(\bar{\boldsymbol{p}})$, que não depende das coordenadas generalizadas. Quando tal transformação existe, os n momenta $\{\bar{p}_1, \bar{p}_2, ..., \bar{p}_n\}$ são integrais de movimento e as coordenadas $\bar{\boldsymbol{q}}$ evoluem linearmente com o tempo. Além disso, estas integrais de movimento estão em involução pois satisfazem $\{\bar{p}_j, \bar{p}_k\}=0$ para todo j,k, onde

$$\{f,g\}=\boldsymbol{\nabla}_{\boldsymbol{q}}f\cdot\boldsymbol{\nabla}_{\boldsymbol{p}}g-\boldsymbol{\nabla}_{\boldsymbol{p}}f\cdot\boldsymbol{\nabla}_{\boldsymbol{q}}g \tag{1.7}$$

denota o parênteses de Poisson entre as funções $f(\boldsymbol{q},\boldsymbol{p})$ e $g(\boldsymbol{q},\boldsymbol{p})$. Neste processo é preciso resolver uma equação a derivadas parciais de primeira ordem com n variáveis, a equação de Hamilton-Jacobi:

$$H(\boldsymbol{q},\boldsymbol{\nabla}_{\boldsymbol{q}}S)=\bar{H}(\bar{\boldsymbol{p}})\equiv E, \tag{1.8}$$

onde a incógnita $S=S(\boldsymbol{q},\bar{\boldsymbol{p}})$ é a função geratriz a ser determinada. Se esta equação possui solução, os novos momenta podem ser escolhidos como combinações das n constantes arbitrárias de integração, e o sistema é dito integrável.

Pode ser mostrado que as superfícies do espaço de fase nas quais as órbitas limitadas de um sistema integrável estão confinadas são topologicamente equivalentes a toros n-dimensionais. Neste caso os momenta $\bar{\boldsymbol{p}}$ podem ser escolhidos como as variáveis de ação

$\boldsymbol{I} = (I_1, I_2, ..., I_n)$,

$$I_j = \frac{1}{2\pi} \oint_{\gamma_j} \boldsymbol{p} \cdot d\boldsymbol{q}, \tag{1.9}$$

onde $\gamma_1, \gamma_2, ..., \gamma_n$ são curvas fechadas irredutíveis e independentes no toro. As coordenadas canonicamente conjugadas a $\boldsymbol{I}$ são as variáveis de ângulo $\boldsymbol{\theta} = (\theta_1, \theta_2, ..., \theta_n)$, cuja evolução temporal é dada por

$$\theta_j(t) = \theta_{0j} + \omega_j t \mod 2\pi. \tag{1.10}$$

A forma das trajetórias em cada toro depende da particular relação existente entre as freqüências ω_j.

Perturbação de sistemas integráveis

A questão que segue é o que acontece com a estrutura de toros do espaço de fase quando uma hamiltoniana integrável $H_0(\boldsymbol{I})$ é perturbada por um termo pequeno $\varepsilon H_1(\boldsymbol{\theta}, \boldsymbol{I})$:

$$H(\boldsymbol{\theta}, \boldsymbol{I}) = H_0(\boldsymbol{I}) + \varepsilon H_1(\boldsymbol{\theta}, \boldsymbol{I}). \tag{1.11}$$

Devido ao *problema dos pequenos denominadores*, a teoria clássica de perturbações é incapaz de fornecer uma resposta satisfatória a respeito da integrabilidade de H, ou seja, se existem novas variáveis de ângulo e ação $(\bar{\boldsymbol{\theta}}, \bar{\boldsymbol{I}})$ tais que $H = H(\bar{\boldsymbol{I}})$. A solução deste problema foi encontrada, no entanto, por Kolmogorov, Arnold e Moser, e ficou conhecida como *teorema KAM*.

Para H_0 suficientemente diferenciável e não degenerada $(\det(\partial\omega_j/\partial I_k) \neq 0$, onde $\omega_j = \partial H_0/\partial I_j)$, o teorema KAM afirma essencialmente que: "Se as freqüências ω_j são *suficientemente incomensuráveis* o toro correspondente é apenas deformado. Caso contrário o toro é destruído, e as trajetórias passam a ter acesso a uma região de maior dimensão no espaço de fase. Ainda, a medida de Lebesgue das regiões destruídas vai a zero quando a perturbação é reduzida a zero."

O conceito de "suficientemente incomensurável" é um tanto técnico (veja, por exemplo, [11]). Este depende de ε e está associado ao grau de imprecisão com que determinadas relações entre as freqüências ω_j são aproximadas por números racionais. No outro extremo estão os toros ressonantes, aqueles cujas freqüências satisfazem $\boldsymbol{m} \cdot \boldsymbol{\omega} = 0$ para alguma $m-$upla de inteiros $\boldsymbol{m}$. Toros ressonantes formam um conjunto denso no espaço de fase do sistema não perturbado. Estes toros são tipicamente destruídos pela perturbação.

Para ilustrar a dinâmica nas regiões em que os toros são destruídos convém considerar uma hamiltoniana com dois graus de liberdade, $H(\theta_1, \theta_2, I_1, I_2) = H_0(I_1, I_2) + \varepsilon H_1(\theta_1, \theta_2, I_1, I_2)$. Neste caso, o fluxo está restrito a três dimensões para cada valor fixo da energia. Um mapa de seção de Poincaré $\boldsymbol{M}(\theta_1^{(k)}, I_1^{(k)}) = (\theta_1^{(k+1)}, I_1^{(k+1)})$ pode então ser definido pelos pontos (θ_1, I_1) de sucessivas interseções das trajetórias com a superfície $\theta_2 =$ cte (I_2 é determinado pela condição de conservação de energia):

$$\theta_1^{(k+1)} = \theta_1^{(k)} + 2\pi R(I_1^{(k)}) + \varepsilon f(\theta_1^{(k)}, I_1^{(k)}) \mod 2\pi, \tag{1.12}$$

$$I_1^{(k+1)} = I_1^{(k)} + \varepsilon g(\theta_1^{(k)}, I_1^{(k)}), \tag{1.13}$$

onde εf e εg são os termos de perturbação, e $R = \omega_1/\omega_2$. Quando $\varepsilon = 0$, os toros correspondem a circunferências concêntricas invariantes no mapa de seção, como ilustrado na Fig. 1.1(a). Em particular, toros ressonantes correspondem a circunferências preenchidas por órbitas periódicas. Na presença da perturbação, o teorema de Poincaré-Birkhoff afirma que a destruição de um toro ressonante leva genericamente à criação de pontos periódicos instáveis (hiperbólicos) e marginalmente estáveis (elípticos), como mostrado na Fig. 1.1(b).

Os pontos elípticos são circundados por ilhas de novos toros criados pela perturbação. Aos pontos hiperbólicos estão associadas variedades estáveis e instáveis, cujos pontos são atraídos e repelidos pelos pontos periódicos, respectivamente. Estas variedades se interceptam em infinitos pontos formando uma complicada estrutura chamada emaranhado heteroclínico, que é a origem da dinâmica caótica discutida nas próximas Seções. O teorema de Poincaré-Birkhoff pode então ser repetidamente aplicado aos toros ressonantes das pequenas ilhas criadas pela perturbação, para mostrar que o mesmo tipo de formação, com emaranhados e ilhas, está presente em escalas menores e menores.

A Fig. 1.1 refere-se ao caso de dois graus de liberdade. A destruição de toros leva naturalmente a uma dinâmica complicada também no caso de vários graus de liberdade. Há uma diferença, no entanto. No caso $n \geq 3$, um toro $n-$dimensional não é capaz de dividir uma superfície de energia $(2n-1)-$dimensional em duas partes, uma interna e outra externa a ele. Como conseqüência, os toros destruídos pela perturbação podem formar uma única região conectada. Em certos casos, órbitas desta região podem chegar arbitrariamente próximas a todos os pontos energeticamente acessíveis, dando origem ao fenômeno conhecido como difusão de Arnold [12]. Este fenômeno pode ser visto como uma versão perturbativa da hipótese da ergodicidade, segundo a qual sistemas de muitas partículas ocupam com igual probabilidade qualquer estado acessível do espaço de fase.

Emaranhados homoclínicos

A estabilidade das órbitas periódicas de um mapa de seção $\boldsymbol{M}$ é definida a partir dos autovalores do sistema linearizado. Os pontos de uma órbita de período j são necessariamente pontos fixos do mapa $\boldsymbol{M}^j$. Este mapa preserva área, e como tal apresenta apenas três possibilidades para os autovalores λ_1 e λ_2 da matriz jacobiana $\boldsymbol{DM}^j$: (a) $\lambda_1 = \lambda_2^{-1} \neq \pm 1$, onde λ_1 e λ_2 são reais; (b) $\lambda_1 = \lambda_2^* = \exp(i\alpha)$, onde $\alpha \neq 0$ é real, e * denota conjugação complexa; (c) $\lambda_1 = \lambda_2^{-1} = \pm 1$. (a) e (b) correspondem respectivamente aos pontos hiperbólicos e elípticos, mencionados anteriormente, e (c) representa o caso degenerado dos pontos fixos parabólicos. Assim como os pontos elípticos, os pontos parabólicos são

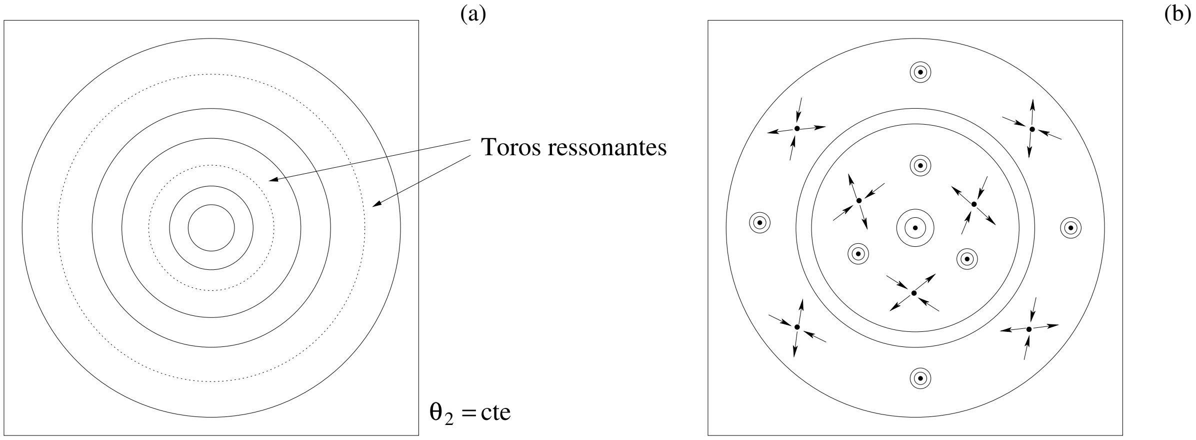

Figura 1.1: (a) Seção de Poincaré de um sistema integrável. (b) Perturbação de um sistema integrável.

marginalmente estáveis. Exemplos de tais pontos são aqueles em toros ressonantes.

O *teorema das variedades invariantes* afirma que, associado a um ponto fixo hiperbólico $\boldsymbol{x}$ de um mapa suave e inversível, existe uma única variedade suave $W^s(\boldsymbol{x})$ de pontos que tendem exponencialmente ao ponto fixo sob iterações do mapa (variedade estável), e outra variedade $W^u(\boldsymbol{x})$ com a mesma propriedade em relação ao mapa inverso (variedade instável). Pontos fixos hiperbólicos são estruturalmente estáveis, no sentido que, sob pequenas perturbações, são transformados em pontos fixos de mesma natureza próximos aos originais. O mesmo não acontece com pontos parabólicos, que quando perturbados podem se transformar em pontos elípticos, hiperbólicos ou aperiódicos, como ocorre na destruição de toros ressonantes. Além disso, as variedades invariantes associadas a pontos hiperbólicos se deformam suavemente sob a ação de perturbações suaves.

Da definição das variedades invariantes segue que não podem existir pontos de interseção entre duas variedades de mesmo tipo – estável com estável ou instável com instável. Podem existir, no entanto, interseções entre uma variedade estável $W^s(\boldsymbol{x}_1)$ e uma variedade instável $W^u(\boldsymbol{x}_2)$. Se este for o caso, todas as imagens $\boldsymbol{M}^i(\tilde{\boldsymbol{x}})$ e pré-imagens $\boldsymbol{M}^{-i}(\tilde{\boldsymbol{x}})$ de um ponto de interseção $\tilde{\boldsymbol{x}} \in W^s(\boldsymbol{x}_1) \cap W^u(\boldsymbol{x}_2)$ são também pontos de interseção. Como resultado, a interseção entre as variedades estável e instável se dá necessariamente num número infinito de pontos. Tais pontos são chamados de homoclínicos quando $\boldsymbol{x}_1 = \boldsymbol{x}_2$ e heteroclínicos quando $\boldsymbol{x}_1 \neq \boldsymbol{x}_2$. Como mencionado, pontos heteroclínicos são os responsáveis pela dinâmica complicada que emerge da destruição de toros ressonantes.

Um emaranhado de interseções homoclínicas transversais é ilustrado na Fig. 1.2, onde os lóbulos A e $\boldsymbol{M}(A)$ possuem mesma área quando o mapa é conservativo. O infinito número de lóbulos entrelaçados implica em grande sensibilidade a condições iniciais, no sentido que a distância entre órbitas inicialmente próximas cresce rapidamente sob iterações do mapa. No caso em que $\boldsymbol{M}$ é um difeomorfismo no plano (não necessariamente conservativo), o teorema homoclínico de Smale-Birkhoff afirma que interseções homoclínicas transversais resultam na existência de um conjunto invariante de $\boldsymbol{M}^k$, para algum k, com dinâmica simbólica equivalente à do conjunto invariante do mapa de ferradura de Smale, cujas propriedades são bem conhecidas. Resultados semelhantes podem ser estabelecidos no caso heteroclínico.

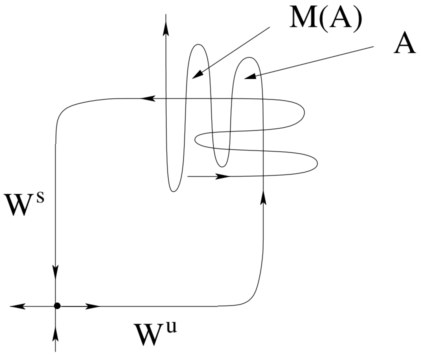

Figura 1.2: Emaranhado homoclínico.

A dinâmica do conjunto invariante Λ do mapa de ferradura de Smale é definida da seguinte forma. Cada ponto $\boldsymbol{a} \in \Lambda$ é representado por uma seqüência bi-infinita de dois símbolos,

$$\boldsymbol{a} = ...a_{-3}a_{-2}a_{-1} \cdot a_0a_1a_2..., \tag{1.14}$$

onde $a_j \in \{0, 1\}$, e a ação do mapa é definida pela translação dos símbolos à esquerda:

$$S(\boldsymbol{a}) = ...a_{-2}a_{-1}a_0 \cdot a_1a_2a_3... \ . \tag{1.15}$$

Este mapa possui um número contável, porém infinito, de órbitas periódicas, um número incontável de órbitas não periódicas e uma órbita densa em Λ. (No espaço dos símbolos a métrica é usualmente definida por $d(\boldsymbol{a}, \boldsymbol{b}) = \sum |a_j - b_j|/2^{|j|}$.) Os pontos periódicos formam um conjunto denso em Λ, e o seu número cresce exponencialmente com o período.

O teorema de Smale-Birkhoff tem várias implicações não triviais. Em particular, no caso em que $\boldsymbol{M}$ é um mapa de seção de Poincaré de uma hamiltoniana H, a existência de uma órbita densa no conjunto invariante de $\boldsymbol{M}^k$ implica na não integrabilidade de H.

Método de Melnikov

Uma situação freqüente em sistemas integráveis é aquela em que existe um ponto fixo hiperbólico cujas variedades estável e instável se interceptam formando um *laço homoclínico*

[14], como mostrado na Fig. 1.3(a). Esta configuração é não genérica, uma vez que os ramos coincidentes das variedades invariantes tornam-se, em geral, diferentes na presença de perturbações, levando a uma mudança metamórfica na dinâmica do sistema. Nesta Seção é discutido um método, conhecido como método de Melnikov [13], que pode ser usado para verificar o aparecimento de interseções homoclínicas transversais quando sistemas integráveis são submetidos a perturbações.

Consideramos um sistema hamiltoniano conservativo com um grau de liberdade submetido a uma perturbação periódica no tempo,

$$H(q,p,t) = H_0(q,p) + \varepsilon H_1(q,p,t), \tag{1.16}$$

onde $H_1(q,p,t+2\pi/\omega) = H_1(q,p,t)$. Assumimos que H_0 é integrável e possui um ponto fixo hiperbólico cujas variedades invariantes se interceptam ao longo de um laço homoclínico Γ, como na Fig. 1.3(a). As equações deste sistema podem ser escritas em forma autônoma (sem dependência explícita no tempo) em $I\!R^2 \times S^1$:

$$\frac{d\boldsymbol{x}}{dt} = \boldsymbol{F}_0(\boldsymbol{x}) + \varepsilon \boldsymbol{F}_1(\boldsymbol{x},\theta), \tag{1.17}$$

$$\frac{d\theta}{dt} = 1, \tag{1.18}$$

onde $\boldsymbol{F}_1(\boldsymbol{x},\theta + 2\pi/\omega) = \boldsymbol{F}_1(\boldsymbol{x},\theta)$. No espaço $(\boldsymbol{x},\theta)$, o ponto fixo torna-se uma órbita periódica γ_0 com variedades estável $W^s(\gamma_0)$ e instável $W^u(\gamma_0)$ que se interceptam em $\Gamma \times S^1$. Quando $\varepsilon \neq 0$, γ_0 transforma-se numa nova órbita periódica γ_ε, próxima à original, e as variedades invariantes $W^{s,u}(\gamma_0)$ deformam-se suavemente nas novas variedades $W^{s,u}(\gamma_\varepsilon)$. O método de Melnikov baseia-se em medir distâncias entre $W^s(\gamma_\varepsilon)$ e $W^u(\gamma_\varepsilon)$ a fim de localizar possíveis interseções transversais.

Seja Σ_{θ_0} a seção definida por $\theta = \theta_0$ (mod $2\pi/\omega$), e $\boldsymbol{M}_{\varepsilon,\theta_0} : \Sigma_{\theta_0} \to \Sigma_{\theta_0}$ o correspondente mapa de Poincaré. Considere nesta seção as interseções entre a reta normal a $\Gamma \times \{\theta_0\}$ no ponto $\boldsymbol{x}_0 \in \Sigma_{\theta_0}$ e as variedades $W^{s,u}(\gamma_\varepsilon)$. Denote por $\boldsymbol{A}^{s,u}$ os pontos de interseção mais próximos de $\boldsymbol{x}_0$. Definimos

$$\Delta_\varepsilon(t,\theta_0) = \boldsymbol{F}_0(\boldsymbol{x}_0(t-\theta_0)) \wedge [\boldsymbol{x}^u(t;\theta_0,\varepsilon) - \boldsymbol{x}^s(t;\theta_0,\varepsilon)], \tag{1.19}$$

onde $\boldsymbol{x}^{s,u}(t;\theta_0,\varepsilon)$ são as soluções das Eqs. (1.17)-(1.18) que passam por $\boldsymbol{A}^{s,u}$ em $t=\theta_0$, e $\boldsymbol{x}_0(t)$ é a solução do sistema não perturbado que passa por $\boldsymbol{x}_0$ em $t=0$. O produto cunha em (1.19) é definido por $\boldsymbol{A}\wedge\boldsymbol{B}=A_1B_2-A_2B_1$. Uma vez que $\boldsymbol{F}_0$ é tangente a Γ, $\Delta_\varepsilon(\theta_0,\theta_0)/|\boldsymbol{F}_0(\boldsymbol{x}_0)|$ é a distância entre $W^s(\gamma_\varepsilon)$ e $W^u(\gamma_\varepsilon)$ normal a $(\Gamma\times S^1)\cap\Sigma_{\theta_0}$ no ponto $\boldsymbol{x}_0$, como mostrado na Fig. 1.3(b).

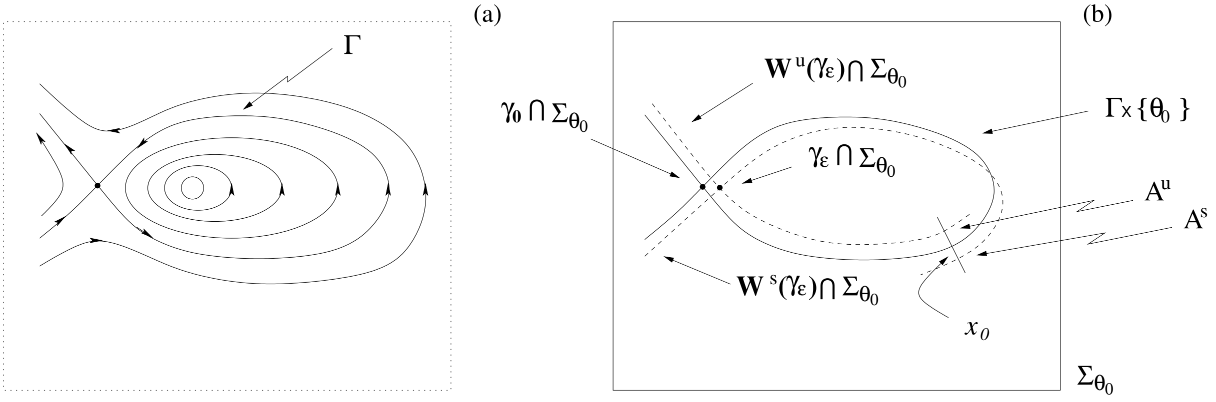

Figura 1.3: (a) Laço homoclínico Γ. (b) Variedades invariantes do mapa $\boldsymbol{M}_{\varepsilon,\theta_0}$.

Em primeira ordem em ε tem-se $\boldsymbol{x}^{s,u}(t;\theta_0,\varepsilon)=\boldsymbol{x}_0(t-\theta_0)+\boldsymbol{x}_1^{s,u}(t;\theta_0,\varepsilon)$, e a Eq. (1.19) transforma-se em

$$\Delta_\varepsilon(t,\theta_0)=\varepsilon\boldsymbol{F}_0(\boldsymbol{x}_0(t-\theta_0))\wedge[\boldsymbol{x}_1^u(t;\theta_0,\varepsilon)-\boldsymbol{x}_1^s(t;\theta_0,\varepsilon)], \tag{1.20}$$

onde $\boldsymbol{x}_1^{s,u}$ satisfaz

$$\frac{d\boldsymbol{x}_1^{s,u}(t,\theta_0)}{dt}=\boldsymbol{DF}_0(\boldsymbol{x}_0(t-\theta_0))\cdot\boldsymbol{x}_1^{s,u}(t;\theta_0,\varepsilon)+\boldsymbol{F}_1(\boldsymbol{x}_0(t-\theta_0),t). \tag{1.21}$$

A Eq. (1.20) pode ser dividida em duas partes, definidas como $\Delta^{s,u}(t,\theta_0)=\boldsymbol{F}_0(\boldsymbol{x}_0(t-\theta_0))\wedge\boldsymbol{x}_1^{s,u}(t;\theta_0,\varepsilon)$. No caso em que a matriz jacobiana de $\boldsymbol{F}_0$ tem traço nulo em Γ, como ocorre quando $\boldsymbol{x}=(q,p)$ são coordenadas canônicas, $\Delta^{s,u}$ satisfaz

$$\frac{d\Delta^{s,u}(t,\theta_0)}{dt}=\boldsymbol{F}_0(\boldsymbol{x}_0(t-\theta_0))\wedge\boldsymbol{F}_1(\boldsymbol{x}_0(t-\theta_0),t). \tag{1.22}$$

Uma relação integral para $\Delta_\varepsilon(\theta_0, \theta_0) = \varepsilon\,[\Delta^u(\theta_0, \theta_0) - \Delta^s(\theta_0, \theta_0)]$ é então obtida a partir da integração de $\Delta^u(t, \theta_0)$ e $\Delta^s(t, \theta_0)$ nos intervalos $(-\infty, \theta_0)$ e $(+\infty, \theta_0)$, respectivamente:

$$\Delta_\varepsilon(\theta_0, \theta_0) = \varepsilon \int_{-\infty}^{+\infty} \boldsymbol{F}_0(\boldsymbol{x}_0(t)) \wedge \boldsymbol{F}_1(\boldsymbol{x}_0(t), t + \theta_0) dt. \tag{1.23}$$

A função de Melnikov é definida como

$$M(\theta_0) = \int_{-\infty}^{+\infty} \boldsymbol{F}_0(\boldsymbol{x}_0(t)) \wedge \boldsymbol{F}_1(\boldsymbol{x}_0(t), t + \theta_0) dt. \tag{1.24}$$

Do teorema da função inversa segue que se $M(\theta_0)$ possui zeros simples, então $W^s(\gamma_\varepsilon) \cap \Sigma_{\theta_0}$ e $W^u(\gamma_\varepsilon) \cap \Sigma_{\theta_0}$ possuem interseções transversais para ε suficientemente pequeno; se, por outro lado, $|M(\theta_0)| \geq \alpha > 0$ para alguma constante α, então existe $\varepsilon_0 > 0$ tal que não há interseções para $0 < \varepsilon \leq \varepsilon_0$. O método de Melnikov consiste em estudar os zeros de $M(\theta_0)$.

A função de Melnikov (1.24) também pode ser escrita como

$$M(\theta_0) = \frac{1}{\varepsilon} \int_{-\infty}^{+\infty} \frac{dH_0}{dt}(\boldsymbol{x}_0(t), t + \theta_0) dt, \tag{1.25}$$

onde a dependência com a perturbação está implícita na evolução temporal de H_0, ou ainda

$$M(\theta_0) = \int_{-\infty}^{+\infty} \{H_0, H_1\}(\boldsymbol{x}_0(t), t + \theta_0) dt, \tag{1.26}$$

onde $\{.,.\}$ indica o parênteses de Poisson (1.7).

A mesma formulação do método de Melnikov pode ser aplicada a hamiltonianas conservativas com dois graus de liberdade mediante redução hamiltoniana. Uma hamiltoniana com dois graus de liberdade da forma $H = H(q, p, \theta, I)$ satisfazendo $d\theta/dt = \partial H/\partial I \neq 0$, onde $\theta = \theta \bmod 2\pi$, pode ser reduzida, em cada superfície de energia, a uma hamiltoniana com um grau de liberdade e dependência periódica no tempo. Neste caso, a equação $H(q, p, \theta, I) = E$ pode ser resolvida para I,

$$I = -K(q, p, \theta; E), \tag{1.27}$$

e as equações de movimento passam a ser escritas como

$$\frac{dq}{d\theta} = \frac{\partial K}{\partial p}(q, p, \theta; E) \tag{1.28}$$

$$\frac{dp}{d\theta} = -\frac{\partial K}{\partial q}(q, p, \theta; E). \tag{1.29}$$

K é a hamiltoniana e θ é o tempo conjugado no sistema reduzido.

As Eqs. (1.24)-(1.26) envolvem a hipótese $Tr(\boldsymbol{DF}_0) = 0$, que é satisfeita por sistemas hamiltonianos desde que se tenha o laço homoclínico em coordenadas canônicas. No Apêndice A estudamos um caso em que esta e outras hipóteses aqui assumidas, tal como a hiperbolicidade do ponto fixo, são violadas. Uma derivação alternativa apresentada naquele Apêndice mostra que o mesmo resultado se sustenta em condições mais gerais.

1.2 Caos em sistemas fechados

Foi visto que a dinâmica de órbitas limitadas em sistemas hamiltonianos pode apresentar dois comportamentos distintos. Quando a hamiltoniana é integrável, as órbitas estão confinadas a toros $n-$dimensionais e as variáveis dinâmicas são funções quase-periódicas do tempo, definidas pelo conjunto de n freqüências dos toros. Neste caso a evolução temporal é muito simples e dizemos que a dinâmica é *regular*. Quando toros são destruídos por uma perturbação, órbitas típicas passam a explorar uniformemente uma região de maior dimensão no espaço de fase, e o sistema passa a apresentar sensibilidade a condições iniciais. A evolução do sistema torna-se, portanto, tremendamente complicada quando comparada ao caso integrável. Dizemos que a dinâmica neste caso é *caótica*. Estas considerações referem-se à particular situação em que o sistema é hamiltoniano e o caos resulta da perturbação de um sistema integrável. O conceito de caos é, no entanto, muito mais geral e aplica-se também a regimes não perturbativos e a sistemas não hamiltonianos. Nesta Seção discutimos as características do movimento caótico no contexto de sistemas dinâmicos em geral.

Parte das definições da Seção 1.1 generalizam-se naturalmente para sistemas não hamiltonianos. É o caso de espaço de fase, integrais de movimento, órbitas periódicas, variedades invariantes, pontos homoclínicos etc. Consideramos sistemas do tipo (1.1) escritos em forma autônoma e mapas da forma (1.2). Nestes sistemas nos concentramos em conjuntos invariantes sob evolução temporal, limitados a uma região finita do espaço de fase.

Não existe uma definição universalmente aceita de caos. Uma definição tentativa é, por exemplo, aquela proposta por Devaney [15], segundo a qual um conjunto invariante do espaço de fase é caótico se: (i) apresenta um conjunto denso de órbitas periódicas; (ii) é topologicamente transitivo (por exemplo, possui uma órbita densa); (iii) tem dependência sensível às condições iniciais. Mas definições diferentes podem ser encontradas. Outros autores, por exemplo Ott [8], definem como caóticos os sistemas que apresentam algum expoente de Lyapunov positivo. Por isto nos limitamos a discutir propriedades características do caos em vez da definição propriamente dita.

Expoentes de Lyapunov

A propriedade mais marcante que distingue o movimento caótico do regular é a sua grande sensibilidade a condições iniciais. Trajetórias caóticas inicialmente próximas em geral afastam-se exponencialmente com o tempo: $\delta\boldsymbol{x}(t) = \delta\boldsymbol{x}_0 \exp(ht)$, $h > 0$. Tendo em vista que a condição inicial de um sistema físico real pode ser determinada apenas dentro de uma certa precisão, esta propriedade implica na impredictibilidade do estado do sistema depois de um intervalo de tempo maior que uma escala característica que depende de $1/h$. A mesma observação vale para simulações numéricas, onde erros de arredondamento levam ao cálculo de trajetórias que se afastam rapidamente das trajetórias verdadeiras.

O afastamento exponencial das órbitas é quantificado pelos expoentes de Lyapunov, que no caso de mapas são definidos por

$$h_j = \lim_{k\to\infty} \frac{1}{k} \ln |\boldsymbol{DM}^k(\boldsymbol{x}_0) \cdot \boldsymbol{u}_{0j}|, \tag{1.30}$$

onde $\boldsymbol{u}_{0j}$ é a orientação do deslocamento inicial. Um mapa $m-$dimensional possui m expoentes de Lyapunov independentes que são determinados por diferentes escolhas de $\boldsymbol{u}_{0j}$. Órbitas caóticas possuem pelo menos um expoente de Lyapunov positivo. Expoentes de Lyapunov são invariantes por trocas suaves de coordenadas.

Existem, obviamente, hipóteses para que (1.30) esteja bem definido e não dependa do ponto inicial $\boldsymbol{x}_0$ para órbitas típicas. Uma vez que os expoentes de Lyapunov podem ser vistos como quantidades estatísticas, uma destas hipóteses é a existência de uma medida invariante finita. No caso de mapas unidimensionais com medida natural $\mu = \mu(x)$, por exemplo, a relação (1.30) pode ser escrita como

$$h = \int \ln |\frac{dM}{dx}(x)| d\mu. \tag{1.31}$$

A medida natural é definida pela fração de tempo que órbitas típicas gastam na vizinhança de cada ponto da região acessível.

Outra hipótese, já assumida, é de que o conjunto invariante ocupe uma região limitada no espaço de fase. Como resultado, trajetórias vizinhas não podem se afastar exponencialmente por tempo indeterminado, como acontece com o mapa $M(x) = 2x$ para $x \in (-\infty, \infty)$. Isto leva ao fenômeno de 'esticamento e dobra' característico de sistemas caóticos, o qual pode ser observado em mapas tão simples como $M(x) = 2x \bmod 1$ para $x \in [0, 1]$, cujo expoente de Lyapunov é $h = \ln 2$.

Entropias

Suponhamos que duas trajetórias são calculadas exatamente, porém observadas apenas com uma resolução finita. Quando as condições iniciais são suficientemente próximas, as órbitas parecem inicialmente indistinguíveis. Devido à divergência exponencial, as trajetórias caóticas tornam-se distinguíveis depois de iteradas por tempo suficiente. Neste sentido pode-se pensar que a dinâmica caótica produz informação. A entropia métrica é uma medida da taxa de informação produzida pela divergência exponencial das trajetórias caóticas. Em sistemas hamiltonianos típicos, a entropia métrica h_M é igual à soma dos expoentes de Lyapunov positivos,

$$h_M = \sum_{h_j > 0} h_j. \tag{1.32}$$

h_M é positiva em dinâmicas caóticas e zero em dinâmicas regulares. A entropia métrica é invariante por trocas bijetoras de coordenadas.

Conjuntos caóticos são em geral densos em órbitas periódicas instáveis. Órbitas caóticas podem ser vistas como construídas por seqüências de órbitas periódicas. Uma trajetória caótica típica segue uma órbita periódica de sua vizinhança até ser repelida e passar a seguir uma órbita periódica diferente, e assim sucessivamente. A entropia topológica é uma medida do crescimento do número de órbitas periódicas instáveis com o período. No caso de mapas, a entropia topológica h_T pode ser escrita como

$$h_T = \lim_{k\to} \frac{1}{k} \ln N(k), \tag{1.33}$$

onde $N(k)$ denota o número de pontos fixos de $\boldsymbol{M}^k$. Por exemplo, no mapa de ferradura de Smale temos $N(k) \approx 2^k$, donde $h_T = \ln 2$. A entropia topológica é positiva em sistemas caóticos. Esta quantidade é invariante por trocas contínuas de coordenadas.

Mixing e ergodicidade

Quando a dinâmica é caótica, a evolução de um pequeno volume tende a se espalhar uniformemente por toda a região acessível. Isto faz com que regiões inicialmente separadas 'misturem-se' sob evolução temporal, dando origem ao fenômeno de *mixing*. Em termos de uma medida invariante μ, um conjunto invariante R apresenta mixing se

$$\frac{\mu(R_1)}{\mu(R)} = \lim_{T\to\infty} \frac{\mu(R_2 \cap R_1(T))}{\mu(R_2)} \tag{1.34}$$

para quaisquer subconjuntos de medida positiva R_1, $R_2 \subset R$. $R_1(T)$ denota a evolução temporal de R_1 no tempo T, que pode ser contínuo ou discreto.

Um conjunto invariante que apresenta mixing não pode ser decomposto em dois subconjuntos invariantes de medida positiva. Esta propriedade, conhecida como propriedade ergódica, implica na igualdade entre a média temporal e a média espacial de uma função definida no espaço de fase. Então, se f é uma função das variáveis dinâmicas,

$$\lim_{t\to\infty} \frac{1}{t} \int_0^t f(\boldsymbol{x}(t))dt = \int_R f(\boldsymbol{x})d\mu, \tag{1.35}$$

onde $\boldsymbol{x}(t)$ é uma trajetória típica (ergódica) em R. No caso de mapas, a integral é substituída por um somatório no lado esquerdo de (1.35).

Considere, por exemplo, sistemas hamiltonianos conservativos com dois graus de liberdade onde μ é a medida natural. Órbitas regulares são ergódicas (isto é, satisfazem a Eq. (1.35)) sobre toros 2-dimensionais cuja relação de freqüências ω_1/ω_2 é irracional. Órbitas caóticas, por outro lado, são ergódicas em regiões de dimensão três. Esta diferença pode ser observada em mapas de seção de Poincaré, como mostrado na Fig. 1.4, onde órbitas regulares estão confinadas a curvas fechadas, e órbitas caóticas preenchem regiões 2-dimensionais do plano.

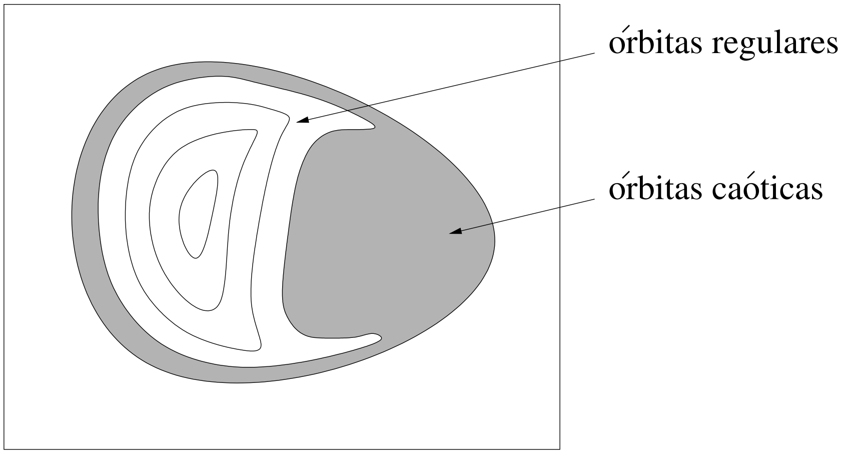

Figura 1.4: Ilustração de uma seção de Poincaré.

Espectro de freqüências

Funções das variáveis dinâmicas calculadas ao longo de trajetórias caóticas variam de forma irregular. No caso de tempo contínuo, isto significa que a transformada de Fourier de uma função $f(\boldsymbol{x}(t))$,

$$F(\omega) = \int_{-\infty}^{+\infty} f(\boldsymbol{x}(t)) \exp(i\omega t) dt, \tag{1.36}$$

não apresenta picos discretos que correspondam a combinações de freqüências fundamentais. Órbitas regulares, por outro lado, muitas vezes apresentam tais picos.

Esta diferença pode ser observada, por exemplo, em sistemas hamiltonianos. As órbitas regulares estão confinadas a toros e são, portanto, periódicas ou quase-periódicas. A Eq. (1.36) integrada ao longo destas órbitas resulta em

$$F(\omega) = \sum_{(k_1,\ldots,k_n)\in\mathbb{Z}^n} a_{k_1\ldots k_n} \delta(\omega - k_1\omega_1 - \ldots - k_n\omega_n), \tag{1.37}$$

onde δ representa a função delta de Dirac, e w_j as freqüências do toro correspondente. As órbitas caóticas podem acessar regiões de dimensão maior que n e não possuem variáveis de ângulo e ação. Por isto apresentam um espectro de freqüências essencialmente contínuo.

Movimentos quase-periódicos são comuns também em órbitas regulares de sistemas dissipativos. A mesma distinção pode então ser observada em sistemas não hamiltonianos.

1.3 Caos em sistemas abertos

Muitos sistemas apresentam um conjunto caótico não atrator (repelor) tal que uma órbita próxima a este conjunto pode gastar um longo tempo na sua vizinhança antes de ser capturada por um conjunto atrator (caótico ou não) ou espalhada ao infinito. A órbita experimenta um transiente caótico no sentido que se comporta como caótica durante o intervalo de tempo em que se encontra próxima ao conjunto não atrator. Como conseqüência uma pequena alteração na condição inicial desta órbita pode levar a uma grande mudança no seu estado final. Em processos de espalhamento, por exemplo, o ângulo de espalhamento pode depender sensivelmente do parâmetro de impacto inicial. Esta sensibilidade é medida em temos da dimensão fractal da variedade estável do repelor, que é tipicamente um conjunto fractal de medida zero.

Conjuntos e dimensões fractais

Curvas e superfícies ordinárias apresentam uma escala característica abaixo da qual não possuem estrutura. Conjuntos fractais, por outro lado, caracterizam-se por apresentar estruturas em escalas arbitrariamente pequenas. Um exemplo de fractal é o conjunto de Cantor *um terço*, construído no intervalo $[0,1]$ pelo seguinte processo: primeiro remove-se o subintervalo de comprimento $1/3$ no meio do intervalo original, em seguida removem-se subintervalos de comprimento $1/3^2$ no meio de cada um dos dois subintervalos restantes, e assim sucessivamente. Embora tenha comprimento total zero, o conjunto resultante admite uma aplicação bijetora ao intervalo $[0,1]$. Além disso, vizinhanças de qualquer ponto do conjunto de Cantor são iguais ao conjunto todo. Esta propriedade, chamada auto-similaridade, é aproximadamente satisfeita por muitos fractais. Quantitativamente, um fractal é caracterizado por sua *dimensão fractal*. A dimensão fractal é uma generalização a valores não inteiros da dimensão ordinária e que assume os valores usuais no caso de curvas e superfícies suaves. Conjuntos fractais em geral apresentam dimensão fractal não inteira.

Existem diferentes definições de dimensão fractal. Uma particularmente importante é a dimensão *box-counting*, introduzida da seguinte maneira. Suponhamos que o conjunto a ser medido se encontre num espaço $n-$dimensional. Cobre-se o espaço com uma grade de $n-$cubos de aresta ε. Conta-se o número $N(\varepsilon)$ de cubos necessários para cobrir o conjunto. A dimensão box-counting é então dada por

$$D = \lim_{\varepsilon \to 0} \frac{\ln N(\varepsilon)}{\ln \varepsilon^{-1}}. \tag{1.38}$$

O conjunto de Cantor um terço, por exemplo, é coberto por $N(\varepsilon_k) = 2^k$ intervalos de comprimento $\varepsilon_k = 3^{-k}$, donde $D = \ln 2/\ln 3$. No caso de uma curva não fractal, temos $N(\varepsilon) \sim \varepsilon^{-1}$, e assim $D = 1$, como esperado. Outra dimensão fractal importante é a dimensão de Hausdorff, discutida no Apêndice B. Em fractais típicos, as dimensões box-counting e de Hausdorff em geral produzem os mesmos valores.

Espalhamento, captura e escape caótico

Usualmente, num processo de espalhamento, partículas são arremessadas contra um potencial localizado, interagem com este potencial e são espalhadas ao infinito. Quando as condições iniciais são tomadas na região de espalhamento o mesmo processo recebe o nome de escape. Se o estado assintótico é num atrator, dizemos que se trata de um processo de captura. Em todos os casos o processo é caótico quando o sistema apresenta sensibilidade a condições iniciais determinada pela presença de um repelor caótico. Espalhamento, captura e escape caótico são processos dinamicamente idênticos no sentido que órbitas típicas chegam a estados finais bem definidos depois de serem repelidas por um conjunto caótico (veja Apêndice E). Não nos preocupamos aqui com a evolução assintótica do sistema, que pode ser regular ou caótica, e sim com o transiente caótico devido ao repelor.

Para entender a formação dos conjuntos invariantes (repelor e suas variedades estável e instável), tomamos como modelo o mapa de ferradura de Smale $\boldsymbol{M}$, esquematizado na Fig. 1.5(a). Sob ação de $\boldsymbol{M}$ o quadrado Q é esticado verticalmente, comprimido horizontalmente e dobrado em forma de ferradura. Os pontos a', b', c' e d' são imagens de a, b, c e d, respectivamente. Suponhamos que os pontos acima da linha ab e abaixo da linha cd sejam levados a estados finais diferentes, digamos A e B. Estes estados podem representar atratores ou direções de escape. O conjunto de pontos levados a A (a B) é chamado bacia de A (de B). Os pontos fora de Q não são os únicos nas bacias de A e de B. A pré-imagem da região III', por exemplo, pertence à bacia de A. O mesmo ocorre com as regiões I' e V' em relação a B. A Fig. 1.5(b) mostra as regiões que deixam Q depois de uma iteração do mapa.

Uma nova aplicação do mapa leva tiras horizontais das regiões $\boldsymbol{M}^{-1}(II')$ e $\boldsymbol{M}^{-1}(IV')$ para fora de Q, como mostrado na Fig. 1.5(c). Este processo repete-se indefinidamente com todas as pré-imagens das regiões I', III' e V', até que quase todos os pontos abandonam Q no limite de infinitas iterações. O conjunto de pontos que permanece em Q (conjunto invariante futuro),

$$\Lambda_f = Q \cap M(Q) \cap M^2(Q) \ldots , \tag{1.39}$$

é um fractal de medida zero formado por um número incontável de linhas horizontais. Analogamente, o conjunto de pontos que permanece em Q sob infinitas aplicações de $\boldsymbol{M}^{-1}$ (conjunto invariante passado),

$$\Lambda_p = Q \cap M^{-1}(Q) \cap M^{-2}(Q) \ldots , \tag{1.40}$$

consiste de um conjunto fractal de linhas verticais. O mapa $\boldsymbol{M}^{-1}$ é definido por uma construção semelhante à da Fig. 1.5(a), porém com a "ferradura" em posição horizontal.

O repelor caótico é então formado pelos pontos de interseção entre (1.39) e (1.40):

$$\Lambda = \Lambda_f \cap \Lambda_p. \tag{1.41}$$

Este é o conjunto invariante cuja dinâmica simbólica foi discutida na Seção 1.1 em conexão com o teorema de Smale-Birkhoff. No sistema estudado no Apêndice A, esta dinâmica aparece junto à separatriz entre órbitas limitadas e órbitas espalhadas ao infinito.

Os conjuntos Λ_f e Λ_p correspondem, respectivamente, às variedades estável e instável de Λ. A variedade estável forma a parte fractal da fronteira entre as bacias de A e de B.

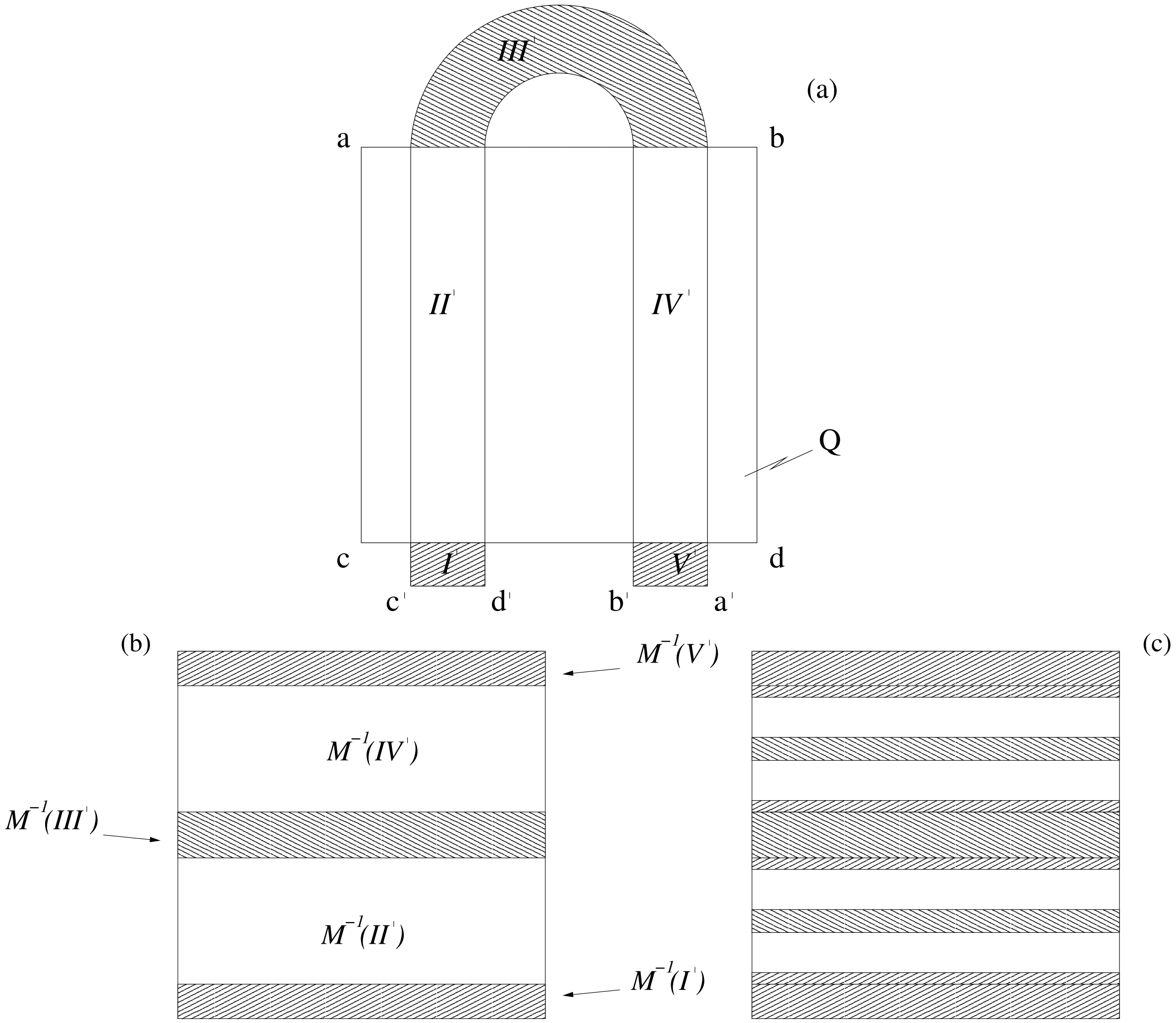

Figura 1.5: (a) Mapa de ferradura de Smale. (b),(c) Pontos que abandonam Q em uma e duas iterações, respectivamente.

Esta fronteira também contém um conjunto não fractal formado por um número contável de linhas horizontais não invariantes. A dimensão da fronteira é igual à dimensão de Λ_f. A sensibilidade a condições iniciais é caracterizada de forma natural pela dimensão fractal da fronteira.

Considere uma distribuição uniforme de pontos iniciais em Q. Se a posição destes pontos é conhecida apenas com precisão ε, a condição final de pontos a uma distância menor que ε da fronteira não está completamente determinada. Estes pontos, que podem pertencer tanto à bacia de A quanto à bacia de B, são chamados incertos. Seja $F(\varepsilon)$ a fração de pontos incertos, e D a dimensão da fronteira. Pode ser mostrado que, para ε pequeno, $F(\varepsilon)$ segue a seguinte lei de escala [16]:

$$F(\varepsilon) \sim \varepsilon^{\alpha}, \tag{1.42}$$

onde $\alpha = 2 - D$. Fazendo $\alpha = n - D$, a relação (1.42) permanece válida em sistemas cuja fronteira está em subespaços de dimensão n.

Fronteiras não fractais têm dimensão $D = n - 1$, e a fração de pontos incertos varia linearmente com ε. Para dobrar a precisão na determinação das bacias basta dobrar a precisão na determinação dos pontos iniciais. Quando a fronteira é fractal, por outro lado, $D > n - 1$ e $\alpha < 1$. Suponhamos, por exemplo, que $\alpha = 0.1$. Para reduzir a fração de pontos incertos por um fator 2 é preciso aumentar a precisão das condições iniciais por 2^{10}. Fronteiras fractais são portanto um obstáculo à determinação da condição final do sistema, tanto em experimentos quanto em simulações numéricas.

Esta sensibilidade a condições iniciais manifesta-se através de um conjunto fractal de singularidades em funções de espalhamento e em funções tempo de escape. Uma função de espalhamento descreve o estado final do sistema (ângulo de espalhamento, por exemplo) como função das condições iniciais (parâmetro de impacto, por exemplo). Uma função tempo de escape descreve o tempo que as trajetórias permanecem próximas ao repelor como função das condições iniciais. O conjunto de singularidades destas funções é formado pela interseção do subespaço de condições iniciais com a variedade estável do repelor.

Em dinâmica, conjuntos fractais são também chamados estranhos. No exemplo acima vimos que o repelor caótico é estranho. A recíproca é em geral verdadeira: repelores estranhos são caóticos. (O mesmo não acontece com relação a atratores, uma vez que são comuns atratores caóticos não estranhos, bem como atratores estranhos não caóticos [17].) Esta relação entre geometria e dinâmica é a base do método para localização de caos apresentado no Apêndice F.

A relação (1.42) pode ser usada para estimar numericamente a dimensão da fronteira. Trata-se do método de incertezas, que se baseia em estudar uma amostra de pontos gerados randomicamente na região que contém a fronteira. Para cada ponto randômico $\boldsymbol{x}$ toma-se um ponto $\boldsymbol{x}_\varepsilon$ a uma distância ε de $\boldsymbol{x}$, e determina-se numericamente a condição final de ambos. O ponto $\boldsymbol{x}$ é rotulado incerto sempre que $\boldsymbol{x}$ e $\boldsymbol{x}_\varepsilon$ são levados a condições finais diferentes. A fração $f(\varepsilon)$ de pontos incertos assim definidos é em geral proporcional a $F(\varepsilon)$. A dimensão é então obtida a partir do gráfico linearizado $\ln f(\varepsilon) \times \ln \varepsilon$. Espera-se que esta dimensão, chamada dimensão de incertezas, resulte igual à dimensão box-counting em sistemas típicos.

Variações deste método são discutidas nos Apêndices B, E e F. No Apêndice B também discutimos problemas de espalhamento em que a dimensão da variedade estável é menor que $n-1$, e o método acima não se aplica.

2

Elementos de relatividade geral

A gravitação newtoniana é uma teoria de interação à distância intrinsecamente linear descrita por um potencial escalar, o potencial gravitacional Φ, que no caso de uma distribuição de massa ρ é determinado pela equação de Poisson,

$$\boldsymbol{\nabla}^2\Phi = 4\pi G\rho. \tag{2.1}$$

As equações de movimento de uma partícula-teste de massa m são naturalmente formuladas em relação a um referencial inercial em termos da hamiltoniana

$$H(\boldsymbol{r},\boldsymbol{p},t) = \frac{|\boldsymbol{p}|^2}{2m} + m\Phi(\boldsymbol{r},t), \tag{2.2}$$

onde t, o tempo canonicamente conjugado a H, é *o tempo absoluto.* A relatividade geral, por outro lado, é uma teoria geométrica não linear (as equações de campo não satisfazem o princípio da superposição), formulada numa variedade espaço-temporal onde o tempo é uma variável dinâmica que depende do observador. Neste Capítulo apresentamos conceitos fundamentais de relatividade geral e cosmologia relativística. As referências básicas são [6, 18, 19, 20, 21].

2.1 Equações da relatividade geral

Segundo o princípio da equivalência da relatividade geral, junto a pontos não singulares sempre existe uma transformação de coordenadas capaz de anular o campo gravitacional localmente, tal que o espaço-tempo, composto de três coordenadas espaciais e uma temporal, é localmente aproximado pelo espaço-tempo de Minkowski da relatividade especial. A incorporação do campo gravitacional na relatividade é então feita descrevendo-o através da curvatura do espaço-tempo realizado como uma variedade 4-dimensional pseudo-riemanniana com assinatura $(-,+,+,+)$, a mesma da métrica de Minkowski.

Neste Capítulo convencionamos que índices gregos vão de 0 a 3, índices latinos vão de 1 a 3 e índices repetidos são somados de acordo com a convenção de Einstein. Escolhemos unidades nas quais $G = 1$ e $c = 1$, onde G é a constante gravitacional, e c é a velocidade da luz no vácuo.

O produto entre dois vetores, bem como a distância entre pontos vizinhos do espaço-tempo, são definidos por um tensor simétrico de ordem 2, o tensor métrico (ou simplesmente métrica):

$$ds^2 = g_{\alpha\beta} dx^\alpha dx^\beta, \tag{2.3}$$

onde $g_{\alpha\beta}$ são funções das coordenadas x^μ que parametrizam a variedade. Tal como no caso de Minkowski, ds^2 pode assumir valores positivos, negativos e nulos. A métrica define propriedades locais do espaço-tempo. As propriedades globais dependem também da escolha de uma topologia compatível com (2.3).

A equação de movimento de uma partícula-teste num campo gravitacional definido pela métrica (2.3) pode ser obtida a partir do princípio variacional

$$\delta \int ds = 0. \tag{2.4}$$

O resultado é a equação da geodésica que, para uma escolha adequada do parâmetro τ, pode ser escrita como

$$\frac{d^2 x^\alpha}{d\tau^2} + \Gamma^\alpha_{\beta\gamma} \frac{dx^\beta}{d\tau} \frac{dx^\gamma}{d\tau} = 0, \tag{2.5}$$

onde $\Gamma^\alpha_{\beta\gamma}$ é o símbolo de Christoffel:

$$\Gamma^\alpha_{\beta\gamma} = \frac{1}{2} g^{\alpha\delta} \left(\frac{\partial g_{\delta\beta}}{\partial x^\gamma} + \frac{\partial g_{\delta\gamma}}{\partial x^\beta} - \frac{\partial g_{\beta\gamma}}{\partial x^\delta} \right). \tag{2.6}$$

$g^{\alpha\beta}$ denota as componentes contravariantes do tensor métrico, obtidas pela inversão da matriz $(g_{\alpha\beta})$.

A Eq. (2.5) pode também ser derivada a partir de uma hamiltoniana conservativa,

$$H = \frac{1}{2} g^{\alpha\beta} p_\alpha p_\beta, \tag{2.7}$$

onde $p^\alpha = m dx^\alpha / d\tau$ no caso de partículas de massa $m > 0$ e $p^\alpha = dx^\alpha / d\tau$ no caso de partículas de massa zero. No primeiro caso o parâmetro τ, chamado parâmetro afim, pode ser identificado com o tempo próprio da partícula. Deve ser observado, no entanto, que a Eq. (2.5) corresponde a uma escolha bastante particular da parametrização das geodésicas. No caso geral temos

$$\frac{d^2 x^\alpha}{dt^2} + \Gamma^\alpha_{\beta\gamma} \frac{dx^\beta}{dt} \frac{dx^\gamma}{dt} = \lambda \frac{dx^\alpha}{dt}, \tag{2.8}$$

onde λ é função de x^μ, dx^μ/dt e d^2x^μ/dt^2, e a formulação hamiltoniana (2.7) deixa de ser válida.

A métrica, por sua vez, é descrita pelas equações de Einstein,

$$R_{\alpha\beta} - \frac{1}{2} g_{\alpha\beta} R = 8\pi T_{\alpha\beta}, \tag{2.9}$$

onde:

$$R_{\alpha\beta} = R^\gamma_{\alpha\gamma\beta} \quad \text{e} \quad R = g^{\alpha\beta} R_{\alpha\beta} \tag{2.10}$$

são o tensor de Ricci e o escalar de curvatura, respectivamente;

$$R^\alpha_{\beta\gamma\delta} = \Gamma^\mu_{\beta\delta} \Gamma^\alpha_{\mu\gamma} - \Gamma^\mu_{\beta\gamma} \Gamma^\alpha_{\mu\delta} + \frac{\partial \Gamma^\alpha_{\beta\delta}}{\partial x^\gamma} - \frac{\partial \Gamma^\alpha_{\beta\gamma}}{\partial x^\delta} \tag{2.11}$$

são as componentes de Riemann do tensor curvatura; $T_{\alpha\beta}$ é o tensor energia-momento. Em termos variacionais a Eq. (2.9) é escrita como

$$\delta \int d^4x \sqrt{-g}\, \mathcal{L}_G = 8\pi\, \delta \int d^4x \sqrt{-g}\, \mathcal{L}_M, \tag{2.12}$$

onde $g = \det(g_{\alpha\beta})$, $\mathcal{L}_G = R$ é a densidade lagrangiana gravitacional, e $\mathcal{L}_M$ é a densidade lagrangiana dos demais campos de matéria.

As equações de Einstein descrevem a interação entre o campo gravitacional, representado pelos termos de curvatura no lado esquerdo da Eq. (2.9), e a distribuição de energia e matéria representada pelo tensor de energia-momento. Estas equações admitem soluções não triviais mesmo quando $T_{\alpha\beta}$ é identicamente nulo. Do ponto de vista matemático, (2.9) forma um conjunto de equações diferenciais parciais não lineares acopladas. Em geral estas equações podem ser resolvidas apenas numericamente. Soluções analíticas são obtidas somente em casos particulares, tipicamente quando o sistema apresenta alguma simetria. Na próxima Seção são discutidos casos intermediários em que as equações de campo podem ser reduzidas a equações diferenciais ordinárias.

De acordo com o princípio da covariança, as equações da relatividade geral são tensoriais e, como tais, possuem formas invariantes por mudanças de coordenadas e de base. Este aspecto da teoria reflete o próprio princípio da relatividade, segundo o qual todos os observadores, inerciais e não inerciais, são equivalentes. As equações de Einstein, em particular, são invariantes pela troca de coordenadas

$$x^\alpha \to y^\alpha, \quad y^\alpha = y^\alpha(x^\beta), \tag{2.13}$$

acompanhada da correspondente transformação nas componentes da métrica:

$$g_{\alpha\beta} \to \frac{\partial x^\gamma}{\partial y^\alpha}\frac{\partial x^\delta}{\partial y^\beta} g_{\gamma\delta}. \tag{2.14}$$

Um sistema de referência, definido por um certo conjunto de observadores, é igualmente descrito por diferentes sistemas de coordenadas. A mudança de coordenadas (2.13) pode transformar o sistema de referência ou apenas representar uma mudança na parametrização do espaço-tempo. As Eqs. (2.9)-(2.10) mantêm-se invariantes também quando escritas em relação a bases de vetores não coordenados. Neste caso as derivadas parciais transformam-se em derivadas direcionais, e as Eqs. (2.6) e (2.11) passam a depender dos comutadores da base (coeficientes de estrutura).

2.2 Cosmologia relativística

Cosmologia é o estudo da estrutura dinâmica do universo como um todo. Enquanto sistema gravitacional, o universo é um sistema relativístico por excelência. Aspectos do comportamento do universo são modelados por soluções das equações de Einstein da relatividade geral. Modelos cosmológicos são representados por famílias não necessariamente explícitas destas soluções.

Cosmologias de Bianchi

Uma classe importante de modelos cosmológicos é aquela das cosmologias espacialmente homogêneas. Tratam-se de espaços-tempos que admitem transformações isométricas nas seções espaciais, isto é, a métrica é função apenas do tempo $t \equiv x^0$: $g_{\alpha\beta} = g_{\alpha\beta}(t)$. Neste caso as equações de campo se reduzem a equações diferenciais ordinárias, tendo o tempo como variável independente.

Os modelos espacialmente homogêneos são classificados de acordo com a álgebra de Lie dos geradores dos grupos de transformação. Tal álgebra é definida em termos das constantes de estrutura C^k_{ij} como

$$[\xi_i, \xi_j] = C^k_{ij}\xi_k, \quad (i, j = 1, 2, 3) \tag{2.15}$$

onde $[.,.]$ denota a operação de comutação e ξ_i os vetores de Killing (geradores). As álgebras de Lie 3-dimensionais são divididas, segundo a classificação de Bianchi, em nove subgrupos chamados tipo I, tipo II, ..., tipo IX [22].

O caso mais simples é o da cosmologia Bianchi I, definida por $C^k_{ij} \equiv 0$. No vácuo ($T_{\alpha\beta} = 0$) esta simetria reproduz a métrica de Kasner:

$$ds^2 = -dt^2 + t^{2p_1}dx^2 + t^{2p_2}dy^2 + t^{2p_3}dz^2, \tag{2.16}$$

onde p_i satisfaz

$$\sum_i p_i = \sum_i p_i^2 = 1. \tag{2.17}$$

O modelo de Kasner representa um universo em expansão anisotrópica, com dois eixos expandindo (desvio para o vermelho) e um eixo contraindo (desvio para o azul). O elemento de volume $\sqrt{-g} = t$ cresce monotonamente, e o modelo apresenta uma singularidade cosmológica (*big bang*) em $t = 0$.

As cosmologias com dinâmica mais interessante são aquelas de tipo Bianchi VIII e Bianchi IX, definidas por $C^k_{ij} = \epsilon^k_{ij}$ e $C^k_{ij} = \hat{\epsilon}^k_{ij}$, respectivamente. O símbolo ϵ^k_{ij} denota o pseudotensor antissimétrico de Levi-Civita, e ˆ indica troca de sinal nas componentes ϵ^1_{23} e ϵ^1_{32}. Os modelos tipo VIII e IX são chamados coletivamente de cosmologias *mixmaster*. Os grupos de isometria tipo I, tipo VIII e tipo IX são isomorfos respectivamente aos grupos de translação, Lorentz e rotação em três dimensões.

As soluções de vácuo das métricas mixmaster são diagonalizáveis em relação a uma base não coordenada [23]:

$$ds^2 = -dt^2 + a^2\omega^1\omega^1 + b^2\omega^2\omega^2 + c^2\omega^3\omega^3, \tag{2.18}$$

onde a, b e c são funções de t, e ω^k são 1-formas cuja derivada exterior satisfaz $d\omega^k = \frac{1}{2}C^k_{ij}\omega^i \wedge \omega^j$. As correspondentes equações de campo são escritas como

$$\frac{d^2 \ln a^2}{d\tau^2} = (b^2 - \nu c^2)^2 - a^4, \tag{2.19}$$

$$\frac{d^2 \ln b^2}{d\tau^2} = (c^2 - \nu a^2)^2 - b^4, \tag{2.20}$$

$$\frac{d^2 \ln c^2}{d\tau^2} = (a^2 - b^2)^2 - c^4, \tag{2.21}$$

juntamente com o vínculo

$$\frac{d\ln a^2}{d\tau}\frac{d\ln b^2}{d\tau} + \frac{d\ln b^2}{d\tau}\frac{d\ln c^2}{d\tau} + \frac{d\ln c^2}{d\tau}\frac{d\ln a^2}{d\tau} = a^4 + b^4 + c^4 - 2a^2b^2 - 2\nu b^2c^2 - 2\nu c^2a^2, \tag{2.22}$$

onde $d\tau = dt/abc$. As simetrias tipo VIII e tipo IX correspondem a $\nu = -1$ e $\nu = 1$, respectivamente.

Estas cosmologias são singulares em $t = 0$. Os modelos Bianchi VIII apresentam expansão eterna, enquanto os modelos Bianchi IX colapsam a tempo t finito. Em ambos os casos a dinâmica de soluções típicas para $\tau \to -\infty$ $(t = 0)$ aproxima-se àquela de uma seqüência infinita de modelos de Kasner, definindo assim as chamadas *épocas* e *eras* de Kasner.

Cada era é composta de uma ou mais épocas. Uma época corresponde ao intervalo de tempo no qual o modelo é aproximado por (2.16), para um certo conjunto de expoentes p_i

satisfazendo (2.17). Estes expoentes podem ser escritos em termos de um único parâmetro,

$$p_1(u) = -\frac{u}{1+u+u^2}, \quad p_2(u) = \frac{1+u}{1+u+u^2}, \quad p_3(u) = \frac{u+u^2}{1+u+u^2}, \tag{2.23}$$

tal que a transição entre épocas e eras seja definida pelo seguinte mapa:

$$M(u) = \begin{cases} u-1, \ \text{se } u > 1 & \text{(mudança de época)}, \\ u^{-1}-1, \ \text{se } u < 1 & \text{(mudança de era)}. \end{cases} \tag{2.24}$$

Neste mapa consideramos o tempo orientado em direção à singularidade. Ao longo de uma era dois eixos oscilam, um contraindo e outro expandindo, enquanto o terceiro eixo contrai monotonamente, como mostrado na Fig. 2.1. Cada oscilação corresponde a uma época. Nas mudanças de era o eixo que contrai e um dos eixos que oscila trocam seus papéis. Esta dinâmica repete-se um número infinito de vezes até a singularidade.

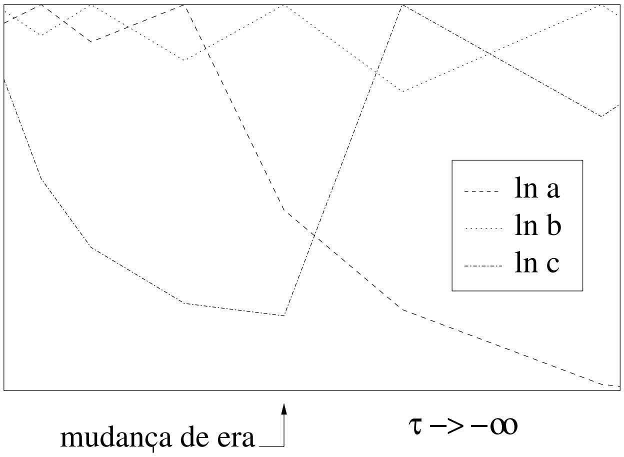

Figura 2.1: Comportamento assintótico do modelo mixmaster nas variáveis a, b e c.

As equações (2.19)-(2.22) podem também ser escritas em forma hamiltoniana, através da seguinte mudança de coordenas [24]:

$$\ln a = \Omega + \beta_+ + \sqrt{3}\beta_-, \tag{2.25}$$

$$\ln b = \Omega + \beta_+ - \sqrt{3}\beta_-, \tag{2.26}$$

$$\ln c = \Omega - 2\beta_+. \tag{2.27}$$

Estas equações correspondem à superfície de energia $\mathcal{H} = 0$ da hamiltoniana

$$4\mathcal{H} = -p_\Omega^2 + p_+^2 + p_-^2 + e^{4\Omega} V(\beta_+, \beta_-), \tag{2.28}$$

onde

$$V = \frac{1}{3} e^{-8\beta_+} - \frac{3\nu}{4} e^{-2\beta_+} \cosh 2\sqrt{3}\beta_- + \frac{2}{3} e^{4\beta_+} (\cosh 4\sqrt{3}\beta_- - 1). \tag{2.29}$$

A redução de (2.28) em relação a $H \equiv -p_\Omega$ leva a uma hamiltoniana não autônoma de dois graus de liberdade:

$$H^2 = p_+^2 + p_-^2 + e^{4\Omega} V(\beta_+, \beta_-), \tag{2.30}$$

onde $\Omega = \ln(abc)/3$ é o tempo canonicamente conjugado a H.

Próximo à singularidade ($\Omega \to -\infty$) o sistema (2.30) pode ser aproximado por um bilhar triangular em expansão. Nesta aproximação o universo corresponde a uma partícula livre sofrendo reflexões *não* especulares nas paredes do bilhar, como mostrado na Fig. 2.2. A velocidade da partícula é unitária:

$$\left(\frac{d\beta_+}{d\Omega}\right)^2 + \left(\frac{d\beta_-}{d\Omega}\right)^2 = 1; \quad \frac{dp_+}{d\Omega} = \frac{dp_-}{d\Omega} = 0. \tag{2.31}$$

A velocidade ortogonal das paredes é

$$\frac{d\beta_\perp}{d\Omega} = \frac{1}{2}, \tag{2.32}$$

e os ângulos de incidência e reflexão estão relacionados por

$$\sin(\theta_{re}) = \frac{3\sin(\theta_{in})}{5 - 4\cos(\theta_{in})}. \tag{2.33}$$

Neste cenário, cada reflexão corresponde a uma mudança de época e cada seqüência de reflexões entre dois lados do triângulo corresponde a uma era (compare as Figs. 2.1 e 2.2).

Os modelos acima representam soluções no vácuo. Próximo à singularidade a dinâmica é qualitativamente a mesma quando matéria e radiação são levadas em conta, pois neste limite os termos anisotrópicos da gravitação dominam sobre os termos não gravitacionais [20]. As oscilações do modelo mixmaster também descrevem o comportamento de modelos mais gerais, incluindo certas cosmologias *não* homogêneas na vizinhança da singularidade cosmológica [25].

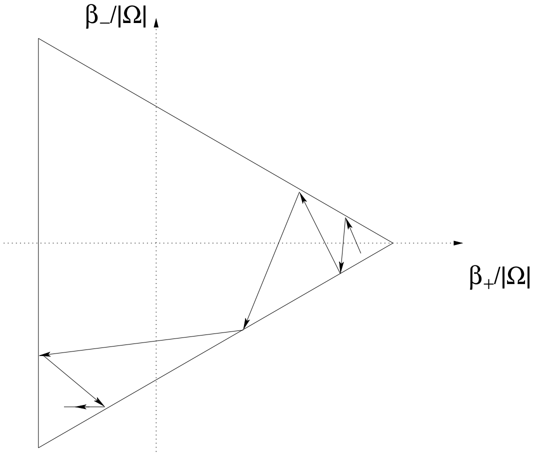

Figura 2.2: Comportamento assintótico do modelo mixmaster nas variáveis β_+, β_- e Ω.

Cosmologias de Friedmann-Robertson-Walker

Cosmologias espacialmente homogêneas *e isotrópicas* admitem, além do grupo de isometria, um grupo de isotropia isomorfo ao grupo de rotações em três dimensões. Existem três dessas cosmologias, as chamadas cosmologias de Friedmann-Robertson-Walker (FRW):

$$ds^2 = -dt^2 + a^2(t)\left[\frac{dr^2}{1-kr^2} + r^2(d\theta^2 + \sin^2\theta d\phi^2)\right]. \tag{2.34}$$

A curvatura das seções espaciais é positiva, zero e negativa, correspondendo a 3-esferas, 3-planos e 3-hiperbolóides, para $k = +1, 0$ e -1, respectivamente. Os universos de FRW começam com uma singularidade cosmológica e expandem para sempre ($k = 0, -1$) ou colapsam ($k = +1$). Estas cosmologias são casos particulares das cosmologias de Bianchi. O caso $k = +1$, por exemplo, corresponde à solução isotrópica do modelo Bianchi IX ($\beta_+ = \beta_- = 0$ quando no vácuo).

As cosmologias de FRW são compatíveis com o aparente estado de homogeneidade e isotropia do universo atual, bem como com a abundância de elementos químicos observados nas galáxias [26]. Os modelos de FRW têm servido também de ponto de partida para o estudo de acoplamentos da gravitação com campos escalares, como no caso de teorias inflacionárias.

Um exemplo simples, porém importante, é o acoplamento conforme de um campo escalar real à cosmologia fechada de FRW ($k = +1$). A densidade Lagrangiana de um campo escalar Ψ de massa m é escrita como [27]

$$\mathcal{L}_M = \left(\frac{d\Psi}{dt}\right)^2 - \frac{1}{6}R\Psi^2 - m^2\Psi^2, \tag{2.35}$$

onde o escalar de curvatura é dado por

$$R = 8\pi m^2\Psi^2. \tag{2.36}$$

Em relação ao tempo conforme, $d\eta = dt/a$, as equações de campo correspondem à superfície de energia $H = 0$ da hamiltoniana

$$H = \frac{1}{2}[-p_a^2 + p_\psi^2 - a^2 + \psi^2 + m^2a^2\psi^2], \tag{2.37}$$

onde $\psi \equiv \sqrt{4\pi/3}a\Psi$. A massa pode ser eliminada das equações de movimento através do reescalamento das variáveis dinâmicas: $a \to a/m$, $p_a \to p_a/m$, $\psi \to \psi/m$ e $p_\psi \to p_\psi/m$.

2.3 Caos nas equações de Einstein e da geodésica

O estudo de caos em relatividade geral tem seguido duas linhas principais de pesquisa. A primeira delas consiste em assumir uma dada métrica e investigar o movimento geodésico na correspondente geometria. Um exemplo é o movimento de partículas-teste em torno de um buraco negro [28, 29]. A outra linha se baseia em analisar a ocorrência de caos nas equações de Einstein. Neste caso as próprias equações de campo formam o sistema dinâmico a ser considerado, como acontece no estudo de modelos cosmológicos [30]. Os protótipos de caos em cosmologia são os modelos mixmaster e FRW acoplado a campos escalares. Ademais, existem outras linhas de pesquisa que têm despertado crescente interesse, como por exemplo a emissão de ondas gravitacionais por fontes caóticas [31].

Um buraco negro de Schwarzschild, de massa M, é descrito pela métrica

$$ds^2 = -\left(1 - 2M/r\right)dt^2 + \left(1 - 2M/r\right)^{-1}dr^2 + r^2(d\theta^2 + \sin^2\theta d\phi^2). \tag{2.38}$$

O movimento de uma partícula-teste de massa m em torno deste buraco negro se reduz ao problema unidimensional de uma partícula não relativística de massa $2m^2$ e energia

$E^2 - m^2$ movendo-se no potencial

$$V(r) = -\frac{M}{r} + \frac{L^2/2m^2}{r^2} - \frac{ML^2/m^2}{r^3}, \tag{2.39}$$

onde $E \equiv -p_t$ e $L \equiv p_\phi$ são integrais de movimento. O potencial (2.39) é integrável e apresenta um laço homoclínico próximo ao centro atrator para $1/16 < (mM/L)^2 < 1/12$. Perturbações do buraco negro por ondas gravitacionais levam genericamente à formação de emaranhados homoclínicos na vizinhança do laço original [32, 33]. No Apêndice A, estudamos o aparecimento de caos no regime $(mM/L)^2 \leq 1/16$.

A ocorrência de caos nas equações de Einstein foi primeiro detectada no modelo mixmaster, através do mapa de retorno ao intervalo $[0, 1]$ da aproximação (2.24):

$$G(u) = \frac{1}{u} - \left[\frac{1}{u}\right], \tag{2.40}$$

onde $[x]$ denota a parte inteira de x. Este mapa, chamado mapa de Gauss, é caótico visto que possui expoente de Lyapunov positivo, $h = \pi^2/6(\ln 2)^2$ [34]. Um intenso debate em torno da não invariança do caos em relatividade geral [6, 35, 36, 37, 38, 39, 40, 41, 42] teve origem quando foi mostrado que os expoentes de Lyapunov da dinâmica contínua (2.19)-(2.22) são nulos [43]. Notamos que o mesmo pode ser observado em certas discretizações da dinâmica, incluindo o mapa (2.24) compactado através da mudança de coordenadas $x = (1 + u)^{-1}$:

$$M(x) = \begin{cases} x/(1-x), & \text{se} \quad 0 \leq x < 1/2, \\ (1-x)/x, & \text{se} \quad 1/2 < x \leq 1. \end{cases} \tag{2.41}$$

Esta propriedade resulta da divergência da medida, cuja densidade invariante é $\rho(x) = x^{-1}$. No Apêndice G, utilizamos técnicas fractais que evitam tais divergências para mostrar que o modelo Bianchi IX é caótico em relação a qualquer escolha de coordenadas.

Outro paradigma de caos em cosmologia é o modelo fechado de FRW conformemente acoplado a um campo escalar real. As variáveis dinâmicas neste caso são o campo escalar ψ e o raio do universo a. Pode ser mostrado que a hamiltoniana (2.37), que descreve o modelo em relação ao tempo conforme, é caótica [27]. Na região física $a > 0$, porém, a dinâmica é não caótica [44]. No Apêndice H mostramos que, embora não caótico, o modelo é não integrável. É oportuno observar que a dinâmica pré-inflacionária pode exibir caos no caso de acoplamentos *minimais* [45].

Uma questão central no estudo da dinâmica relativística é a aparente não invariança do caos, que dependeria da parametrização das trajetórias na equação da geodésica e da escolha do eixo temporal nas equações de Einstein. Isto leva a uma arbitrariedade na escolha do parâmetro t usado para escrever o sistema dinâmico na forma (1.1), o que torna o estudo do caos em relatividade geral muito mais sutil do que em gravitação newtoniana, por exemplo. (Tal como no caso clássico, existe ainda liberdade na escolha das coordenadas e momenta que formam o espaço de fase.) Por esta razão, nos Apêndices A, G e H nos preocupamos em empregar indicadores de caos manifestamente invariantes, baseados no método de Melnikov, na análise de seções de Poincaré, em técnicas fractais e em argumentos de integrabilidade.

3

Caos em sistemas abertos e gravitação

Neste Capítulo discutimos os artigos reproduzidos nos Apêndices. Apresentamos resumos dos principais resultados, bem como extensões e perspectivas de trabalhos futuros. A discussão está dividida de acordo com os temas *emaranhados homoclínicos* (Apêndice A), *espalhamento caótico* (Apêndices B, C e D), *relações entre fractais e caos* (Apêndices E e F) e *caos em cosmologia* (Apêndices G e H).

3.1 Emaranhados homoclínicos em sistemas abertos

Empregamos o método de Melnikov para estudar centros atratores modelados por monopólo mais quadrupólo,

$$H_0(r,p) = p^2/2 + 1/2r^2 - 1/r - \beta/r^3, \tag{3.1}$$

perturbados periodicamente por termos multipolares internos,

$$\varepsilon H_1(r,p,t) = \varepsilon r^{-n} \cos(\Omega t) \quad (n \geq 2). \tag{3.2}$$

Analisamos a dinâmica próxima à separatriz entre as órbitas ligadas e não ligadas de H_0. Para tanto compactamos a região de interesse do espaço de fase mediante a troca de coordenadas $r = u^{-2}$. Observamos que a separatriz forma um laço homoclínico associado ao ponto $(u,p) = (0,0)$ para $0 \leq \beta < 1/16$, e um laço heteroclínico associado aos pontos $(u,p) = (0,0)$ e $(u,p) = (2,0)$ para $\beta = 1/16$. O ponto fixo $(0,0)$ é degenerado (não hiperbólico), tal que, localmente, as trajetórias nos laços invariantes são atraídas ou repelidas algebricamente por este ponto.

Hiperbolicidade do ponto fixo é uma hipótese básica da formulação usual do método de Melnikov e do teorema de Smale-Birkhoff. Contornamos este obstáculo adaptando os resultados das Refs. [46, 47, 48], válidos para pontos fixos degenerados do problema newtoniano de três corpos. Com isto mostramos que, para ε suficientemente pequeno, o sistema perturbado apresenta cruzamentos transversais entre as variedades invariantes dos pontos $(0, 0)$ e $(2, 0)$. Como resultado, composições de mapas de seções de Poincaré deste sistema possuem conjuntos invariantes com dinâmica simbólica equivalente àquela do mapa de ferradura de Smale.

Utilizamos o método de seções de Poincaré para estudar qualitativamente a destruição das superfícies KAM. Órbitas caóticas encontram-se próximas ao laço destruído, enquanto órbitas predominantemente regulares preenchem a região central. A área caótica é máxima para um valor característico de freqüências, $\Omega \sim 1$, e cresce com a ordem n e a intensidade ε da perturbação. A fração caótica do espaço de fase parece não depender do momento de quadrupólo. A dinâmica para $0 < \beta < 1/16$ é qualitativamente a mesma do problema de Kepler perturbado ($\beta = 0$).

O sistema (3.1) é importante por descrever movimentos geodésicos em torno de buracos negros de Schwarzschild e por modelar corpos celestes não esféricos, como estrelas e centros de galáxias. A mesma análise aplica-se também a potenciais mais gerais.

Uma extensão importante deste trabalho seria o estudo de potenciais médios gerados por distribuições de massa em rotação,

$$V(r, \theta, t) = V_0(r) + \varepsilon V_1(r, \theta - \omega t), \tag{3.3}$$

que podem ser usados para descrever o movimento de rotação de galáxias e de grupos globulares [49]. Neste caso, argumentos de analiticidade podem ser usados para mostrar que os cruzamentos homoclínicos transversais persistem em regimes não perturbativos [47].

Emaranhados homoclínicos implicam na existência de órbitas que permanecem a uma distância finita do centro atrator para $t \to -\infty$, mas que vão ao infinito para $t \to +\infty$. A presença deste tipo de órbita daria origem a um novo mecanismo para explicar a perda de massa por grupos globulares [49] e a existência de estrelas intergalácticas [50]. Neste modelo, estrelas periféricas a grupos e galáxias escapariam devido à rotação interna de multipólos não axissimétricos.

3.2 Espalhamento caótico

No contexto de espalhamento caótico, estudamos métodos para o cálculo de dimensões fractais, leis de escala em bifurcações topológicas e transformações da dinâmica causadas por pequenas dissipações.

Espalhamento multidimensional

Discutimos procedimentos para o cálculo da dimensão de conjuntos invariantes em sistemas de espalhamento em que o método de incertezas descrito na Seção 1.3 não se aplica. O modelo considerado consiste de uma partícula refletida por quatro esferas rígidas idênticas localizadas nos vértices de um tetraedro regular. A dimensão do repelor diminui com o raio R das esferas, tal que a codimensão da variedade estável torna-se maior que um para R suficientemente pequeno. Neste regime, a dimensão da fronteira entre diferentes direções de escape é maior que a dimensão da variedade estável e não pode ser usada para estimar a dimensão do repelor.

Consideramos a interseção entre o conjunto invariante futuro (variedade estável) e um plano de condições iniciais. Uma das técnicas consiste em partir da soma de Hausdorff,

$$K_n(d) = \sum_j |c_{n,j}|^d, \tag{3.4}$$

onde $|\ .\ |$ denota o diâmetro, e $c_{n,j}$ os conjuntos conexos de pontos iniciais cujas órbitas permanecem na região de espalhamento depois de n reflexões. A dimensão é calculada a partir do ponto de interseção de $K_n(d)$ para diferentes valores de n. Outro método baseia-se em aproximar o conjunto invariante por $C_n \equiv \cup_j c_{n,j}$, para n suficientemente grande, e estimar a dimensão a partir da definição da dimensão box-counting. Introduzimos também a dimensão de *auto-similaridade*, baseada na aproximação do conjunto invariante por uma estrutura auto-similar. Esta dimensão satisfaz

$$\sum_j \lambda_j^D = 1, \tag{3.5}$$

onde λ_j são as escalas envolvidas na construção do conjunto de Cantor. No sistema considerado, todos estes métodos resultam nos mesmos valores para a dimensão fractal[1].

Foi apresentado recentemente um algoritmo que resolve estruturas fractais de codimensão menor que um, até a escala desejada, sem a necessidade de fazer uma busca exaustiva em todo o espaço [51]. Uma vez que codimensões maiores que um são freqüentes em sistemas com três ou mais graus de liberdade, seria de grande interesse prático obter uma extensão deste resultado válida neste regime.

Bifurcações topológicas

Estudamos bifurcações massivas em espalhamento caótico de dois e três graus de liberdade. Nestes processos, uma família de infinitas órbitas periódicas instáveis é subitamente destruída e substituída por outra quando o parâmetro de bifurcação passa por um valor crítico. O modelo considerado consiste de uma partícula teste espalhada por centros repulsores, onde a energia E da partícula é tomada como parâmetro de bifurcação.

Mostramos que a dimensão D do conjunto de singularidades em funções de espalhamento escala com a energia como

$$D(E) - D(E_c) \sim |E - E_c|^{D(E_c)}, \tag{3.6}$$

onde E_c é a energia de bifurcação. Como conseqüência, o gráfico *dimensão versus energia* apresenta uma *cusp* no ponto crítico. A relação (3.6) foi verificada numericamente no caso de sistemas com dois graus de liberdade.

---

[1] Existem outras maneiras de calcular a dimensão. Uma delas baseia-se na variação do método de incertezas em que são definidos como incertos os pontos iniciais que estão à distância menor que ε de pontos com tempo de escape ou ângulo de espalhamento suficientemente diferente. Outra, aplicável apenas a casos de alta simetria, consiste em reduzir o número de graus de liberdade do sistema. Por exemplo, observamos que no caso de esferas rígidas, com raio suficientemente pequeno, a dimensão do repelor (d_e) está relacionada àquela (d_d) de um sistema plano de três discos de mesmo raio: $d_e - 1 = (d_d - 1)\ln 3/\ln 2$.

Neste trabalho focamos o comportamento da dimensão fractal devido à sua importância física na caracterização de quantidades mensuráveis, como funções de espalhamento. Acreditamos que propriedades singulares também possam ser observadas nos espectros multifractais de dimensão, entropia e expoentes de Lyapunov. Esta questão merece futura investigação no contexto do formalismo termodinâmico [52].

Espalhamento dissipativo

Consideramos o efeito de pequenas dissipações em processos de espalhamento caótico. Quando a dinâmica é hiperbólica, todas as órbitas periódicas são instáveis, e como tais são robustas em relação a pequenas perturbações nos parâmetros do sistema. No caso não hiperbólico, por outro lado, uma pequena dissipação é suficiente para estabilizar órbitas periódicas marginalmente estáveis das superfícies KAM, convertendo suas vizinhanças no espaço de fase nas correspondentes bacias de atração.

Como conseqüência, o espalhamento não hiperbólico ganha características de um processo dissipativo hiperbólico. Em particular, a lei de decaimento das partículas espalhadas deixa de ser algébrica e passa a ser exponencial, e a dimensão do conjunto de singularidades em funções de espalhamento deixa de ser unitária e passa a assumir valores menores que um. Estes efeitos foram verificados numericamente para o mapa

$$\boldsymbol{M}\begin{pmatrix} x \\ y \end{pmatrix} = \begin{cases} \lambda[x-(x+y)^2/4-\nu(x+y)] \\ \lambda^{-1}[y+(x+y)^2/4] \end{cases}, \tag{3.7}$$

o qual é conservativo para $\nu = 0$ e dissipativo para $\nu > 0$. Quando $\nu = 0$, este mapa é hiperbólico para $\lambda \gtrsim 6.5$ e não hiperbólico para $\lambda \lesssim 6.5$.

O espalhamento caótico dissipativo pode modelar, por exemplo, o arraste passivo de partículas por fluxos hidrodinâmicos. Uma extensão interessante deste trabalho consistiria em explorar as conseqüências da dissipação no transporte *ativo*, onde "reações químicas" podem ocorrer durante o processo de espalhamento [54]. Os resultados podem ser importantes em modelos de formação de estrutura (galáxias, estrelas etc.).

3.3 Fractais em sistemas abertos × caos em sistemas fechados

Estudamos caos do ponto de vista de transiente caótico [55]. Em processos de espalhamento, captura e escape caótico, órbitas típicas alcançam estados assintóticos bem definidos depois de serem repelidas por um conjunto caótico não atrator. No caso de movimentos caóticos limitados a uma região finita do espaço de fase, órbitas típicas são repetidamente repelidas por órbitas periódicas instáveis ou, o que é equivalente, por repelores mergulhados no conjunto caótico. Propomo-nos a estudar a dinâmica a partir destes repelores.

Seja E uma pequena sub-região da região caótica. O repelor induzido por E corresponde ao subconjunto caótico J_E cujas órbitas não possuem pontos em comum com E. Este conjunto pode ser estudado com as técnicas usuais de espalhamento e escape caótico. Para tanto, redefinimos o sistema como um sistema de espalhamento tal que o "escape" é caracterizado pelo momento em que as trajetórias chegam a E. O conjunto E passa então a desempenhar um papel análogo ao de estados assintóticos nos processos de espalhamento usuais. A diferença é que, neste caso, a evolução temporal das trajetórias "espalhadas" é truncada a tempo finito. Neste contexto nos referimos a E como a saída do novo sistema.

Suponhamos agora que E esteja definida numa região não necessariamente caótica. Esta saída também induz um conjunto invariante não atrator, o qual pode ser caótico ou regular, dependendo da dinâmica. Tal como no caso de espalhamento potencial, esperamos que repelores estranhos sejam em geral caóticos e, reciprocamente, repelores caóticos sejam em geral estranhos. A geometria do repelor pode ser determinada a partir da dimensão de outros conjuntos de medida zero, como por exemplo a fronteira I_E da bacia de E.

Estudamos o comportamento da dimensão de I_E no limite em que o tamanho de E (volume, por exemplo) é feito arbitrariamente pequeno. Observamos que, quando a saída é definida numa região com dinâmica regular, a dimensão da fronteira é inteira e menor que a dimensão do espaço ambiente para qualquer tamanho finito de E. Por outro lado, quando E é definida numa região caótica, a dimensão de I_E aproxima-se à dimensão do espaço no limite de saídas pequenas.

Os detalhes desta aproximação dependem das propriedades do repelor. Quando sua dinâmica é não hiperbólica, por exemplo, a dimensão pode alcançar o valor máximo até mesmo para saídas de tamanho finito. No caso hiperbólico, por outro lado, a dimensão pode apresentar uma dependência complicada com o tamanho de E, podendo se aproximar do valor limite através de funções *Devil staircase* [56], as quais apresentam estrutura em escalas arbitrariamente pequenas.

É razoável supor que o comportamento descrito acima seja típico em sistemas dinâmicos em geral. A dimensão de I_E pode então ser usada como indicador de caos em regiões confinadas do espaço de fase. O resultado é um método capaz de localizar regiões caóticas e regulares em sistemas conservativos de várias dimensões, onde as componentes caóticas do espaço de fase são identificadas com as bacias de saídas adequadamente definidas.

3.4 Caos em cosmologia

Estudamos caos em cosmologia Bianchi IX e integrabilidade em cosmologias de Friedmann-Robertson-Walker.

Cosmologias mixmaster

Investigamos a cosmologia Bianchi IX, descrita pelas Eqs. (2.19)-(2.22) quando $\nu = 1$. Devido à aparente não invariança do caos em relatividade geral, os resultados existentes não eram conclusivos em relação à presença de caos no modelo. Resolvemos este problema empregando uma variação do método fractal da Seção anterior. Este método é de caráter topológico e como tal não depende da parametrização temporal do sistema. Além disso não envolve hipóteses como compacidade do espaço de fase ou existência de uma medida normalizável, condições freqüentemente não satisfeitas por modelos cosmológicos. A sugestão de utilizar fractais como indicadores invariantes de caos em cosmologia mixmaster deve-se à Ref. [42], cujos resultados estão, no entanto, comprometidos por falhas conceituais.

Introduzimos saídas que no limite assintótico são definidas por $u > u_0$, onde u é o parâmetro do mapa (2.24). Devido à simetria triangular do sistema, cada escolha de u_0 corresponde a três saídas no espaço de fase $(\ln a, \ln b, \ln c, d\ln a/d\Omega, d\ln b/d\Omega, d\ln c/d\Omega)$.

Quase todas as órbitas alcançam estas saídas. As demais formam as fronteiras das bacias de escape.

Estudamos a natureza fractal destas fronteiras. Observamos a existência de estruturas em escalas menores e menores, onde os pontos na fronteira entre duas bacias estão também na fronteira da terceira bacia (propriedade de Wada). Calculamos a dimensão fractal das fronteiras. Os valores obtidos são não inteiros que tendem à dimensão do espaço no limite de saídas pequenas. Concluímos então que o modelo Bianchi IX é mesmo caótico. Enfatizamos que este resultado não depende das coordenadas utilizadas.

O mesmo procedimento pode ser empregado na análise de outros modelos cosmológicos. Em particular temos estudado o modelo Bianchi VIII. Os resultados preliminares mostram a existência de caos de mesma natureza daquela encontrada em Bianchi IX. Além disso encontramos estruturas multifractais no mapa de fronteira do bilhar[2] (2.31)-(2.33).

Por fim, é interessante observar a forte relação que existe entre a dinâmica do mapa (2.41) e aquela do repelor caótico de um sistema de espalhamento não hiperbólico. Em ambos os casos, o maior expoente de Lyapunov do conjunto invariante total é nulo [58]. No entanto, subconjuntos invariantes no complemento de regiões vizinhas às órbitas periódicas marginalmente estáveis possuem expoentes de Lyapunov positivos. Tais subconjuntos foram estudados quando introduzimos pequenas dissipações e pequenas saídas nos mapas (3.7) e (2.41), respectivamente.

Cosmologias de Friedmann-Robertson-Walker

Estudamos a cosmologia fechada de FRW conformemente acoplada a um campo escalar massivo, como descrita pelas Eqs. (2.34)-(2.37). Autores diferentes haviam chegado a conclusões diferentes em relação à existência de caos neste modelo. Novamente, as discrepâncias vinham sendo atribuídas à diferença entre os tempos empregados.

Observamos no entanto que, em relação a qualquer parâmetro temporal bem definido, o sistema é não caótico quando considerado no intervalo de tempo limitado por um big bang

---

[2] Definimos o mapa de fronteira fixando as paredes do bilhar em expansão mediante o reescalamento das variáveis dinâmicas [57]: $\beta_+ \to \beta_+/|\Omega|$ e $\beta_- \to \beta_-/|\Omega|$. Este mapa aproxima a dinâmica assintótica de ambos os modelos, Bianchi VIII e Bianchi IX.

e um big crunch. O sistema é caótico, porém, quando analisado através de uma seqüência não física de expansões e contrações do universo. Usamos a existência de caos no domínio estendido para mostrar que o sistema é não integrável na região física – propriedade que é válida em relação a qualquer escolha de coordenadas.

O mesmo argumento pode ser utilizado para mostrar a não integrabilidade de outros acoplamentos da cosmologia fechada de FRW.

Conclusão

Empregamos extensões do método de Melnikov e do teorema homoclínico de Smale-Birkhoff para estudar fenômenos homoclínicos associados a órbitas não hiperbólicas de sistemas abertos. Discutimos técnicas para o cálculo de dimensões fractais em processos de espalhamento caótico com três ou mais graus de liberdade. Apresentamos leis de escala para a dimensão do conjunto invariante em bifurcações topológicas de espalhamento caótico. Estudamos a metamorfose do conjunto invariante em espalhamento não hiperbólico, causada pela presença de pequenas dissipações. Introduzimos uma técnica fractal para o estudo do caos baseada na transformação do sistema num sistema de escape. Utilizamos esta técnica para caracterizar de forma invariante a dinâmica caótica da cosmologia Bianchi IX. Mostramos que certos acoplamentos conformes da cosmologia fechada de Friedmann-Robertson-Walker são não integráveis, embora não caóticos.

Várias linhas de pesquisa podem ser seguidas a partir deste trabalho, algumas das quais já estão sendo investigadas. Em particular, mencionamos: formação de emaranhados homoclínicos como possível mecanismo para explicar o escape de estrelas de galáxias; tratamento termodinâmico de bifurcações topológicas em processos de espalhamento; emprego de espalhamento caótico dissipativo em modelos de formação de estrutura; estudo de outras cosmologias através de métodos fractais.

Outra via de investigação diz respeito à não invariança do caos em relatividade geral e cosmologia. Os nossos estudos mostram que, nos sistemas considerados, *é possível* caracterizar o caos de forma invariante em relação a reparametrizações temporais. Este resultado contrasta com inúmeros trabalhos que argumentam em favor da não invariança. Os argumentos apresentados nestes trabalhos baseiam-se, na sua vasta maioria, na possibilidade de fazer uma transformação no tempo capaz de anular expoentes de Lyapunov positivos. Reanalisamos a literatura e observamos que *todos* os exemplos fornecidos, incluindo o modelo mixmaster, violam uma ou mais das seguintes hipóteses: sistema escrito em forma autônoma; órbitas limitadas a uma região finita do espaço de fase; medida invariante normalizável. Nestes casos os expoentes de Lyapunov não são indicadores interpretáveis de caos. A questão que segue é se existem transformações capazes de anular expoentes de Lyapunov sem violar estas hipóteses.

Temos estudado esta questão através do sistema de equações (1.1) escrito em forma autônoma e sujeito ao seguinte grupo de transformações:

$$\begin{aligned} \boldsymbol{y} &= \boldsymbol{\psi}(\boldsymbol{x}), \\ d\tau &= \lambda(\boldsymbol{x})dt, \end{aligned}$$

onde $\boldsymbol{\psi}$ é um difeomorfismo, e λ uma função positiva continuamente diferenciável. Mostramos, num trabalho que está em fase final de preparação, que sob condições bastante gerais, expoentes de Lyapunov positivos são mapeados em expoentes positivos. Este resultado está de acordo com a existência de caos invariante no modelo Bianchi IX, pois esperamos que a natureza fractal dos repelores implique na existência de expoentes de Lyapunov positivos nestes conjuntos, qualquer que seja a parametrização temporal.

Observamos, porém, que características próprias de modelos cosmológicos, tais como não compacidade, energia cinética não positiva, singularidades, dependência explícita com o tempo e medida não normalizável, restringem severamente o uso prático de expoentes de Lyapunov nestes sistemas. No caso de Bianchi IX, por exemplo, os conjuntos com expoentes de Lyapunov positivos possuem medida de Lebesgue zero. Uma linha importante de pesquisa consiste então em procurar métodos que, assim como os métodos apresentados nesta tese, sejam capazes de tratar de sistemas com estas propriedades.

Referências Bibliográficas

---

[1] H. Poincaré, *Les Méthodes Nouvelles de la Méchanique Celeste* (Gauthier-Villars, Paris, 1899), Vols. 1-3.

[2] H. Bai-lin, *Chaos* (World Scientific, Singapore, 1982).

[3] J.R. Dorfman, *An Introduction to Chaos in Nonequilibrium Statistical Mechanics* (Cambridge University Press, Cambridge, 1999).

[4] M. Hénon and C. Heiles, 'The applicability of the third integral of motion: some numerical experiments', Astron. J. **69**, 73 (1964).

[5] J. Laskar, 'A numerical experiment on the chaotic behavior of the solar-system', Nature **338**, 73 (1989).

[6] *Deterministic Chaos in General Relativity*, eds. D. Hobill, A. Burd, and A. Coley (Plenum Press, New York, 1994).

[7] H. Goldstein, *Classical Mechanics* (Addison-Wesley, New York, 1980).

[8] E. Ott, *Chaos in Dynamical Systems* (Cambridge University Press, Cambridge, 1994)

[9] J. Guckenheimer and P. Holmes, *Nonlinear Oscillations, Dynamical Systems, and Bifurcations of Vector Fields* (Springer-Verlag, New York, 1983).

[10] D.K. Arrowsmith and C.M. Place, *An Introduction to Dynamical Systems* (Cambridge University Press, Cambridge, 1990).

[11] J. Moser, *Stable and Random Motions in Dynamical Systems* (Princeton University Press, Princeton, 1973).

[12] V.I. Arnold, 'Instability of dynamical systems with many degrees of freedom', Sov. Math. Dokl. **5**, 581 (1964).

[13] V.K. Melnikov, 'On the stability of the center for time periodic perturbations', Trans. Moscow Math. Soc. **12**, 1 (1963).

[14] A.M. Ozorio de Almeida, *Hamiltonian Systems: Chaos and Quantization* (Cambridge University Press, Cambridge, 1988).

[15] R.L. Devaney, *An Introduction to Chaotic Dynamical Systems* (Addison-Wesley, New York, 1989).

[16] C. Grebogi, S.W. McDonald, E. Ott, and J.A. Yorke, 'Final state sensitivity: an obstruction to predictability', Phys. Lett. A **99**, 415 (1983).

[17] C. Grebogi, E. Ott, S. Pelikan, and J.A. Yorke, 'Strange attractors that are not chaotic', Physica D **13**, 261 (1984).

[18] C. Möller, *The Theory of Relativity* (Oxford University Press, Oxford, 1966).

[19] M. Ryan, *Hamiltonian Cosmology* (Springer-Verlag, New York, 1972).

[20] C.W. Misner, K.S. Thorne, and J.A. Wheeler, *Gravitation* (WH Freeman & Company, New York, 1973).

[21] R. d'Inverno, *Introducing Einstein's Relativity* (Clarendon Press, Oxford, 1992).

[22] B. Doubrovine, S. Novikov, et A. Fomenko, *Géométrie Contemporaine: Méthodes et Applications* (Mir, Moscou, 1982), Vol. 1.

[23] V.A. Belinskii, I.M. Khalatnikov, and E.M. Lifshitz, 'Oscillatory approach to a singular point in the relativistic cosmology', Adv. Phys. **19**, 525 (1970).

[24] C.W. Misner, 'Mixmaster universe', Phys. Rev. Lett. **22**, 1071 (1969).

[25] M. Weaver, J. Isenberg, and B.K. Berger, 'Mixmaster behavior in inhomogeneous cosmological spacetimes', Phys. Rev. Lett. **80**, 2984 (1998).

[26] T. Padmanabhan, *Structure Formation in the Universe* (Cambridge University Press, Cambridge, 1993).

[27] E. Calzetta and C. El Hasi, 'Chaotic Friedmann-Robertson-Walker cosmology', Class. Quantum Grav. **10**, 1825 (1993).

[28] W.M. Vieira and P.S. Letelier, 'Chaos around Hénon-Heiles-inspired exact perturbation of a black hole', Phys. Rev. Lett. **76**, 1409 (1996).

[29] A. Saa and R. Venegeroles, 'Chaos around the superposition of a black hole and a thin disk', Phys. Lett. A, **259**, 201 (1999).

[30] J. Koiller, J.R.T.D. Neto, and I.D. Soares, 'Homoclinic phenomena in the gravitational collapse', Phys. Lett. A **110**, 260 (1985).

[31] F. Kokubun, 'Gravitational waves from Hénon-Heiles system', Phys. Rev. D **57**, 2610 (1998).

[32] L. Bombelli and E. Calzetta, 'Chaos around a black hole', Class. Quantum Grav. **9**, 2573 (1992).

[33] P.S. Letelier and W.M. Vieira, 'Chaos in black holes surrounded by gravitational waves', Class. Quantum Grav. **14**, 1247 (1997).

[34] J.D. Barrow, 'Chaotic behaviour in general relativity', Phys. Rep. **85**, 1 (1982).

[35] A. Burd, N. Buric, and G.F.R. Ellis, 'A numerical analysis of chaotic behaviour in Bianchi IX models', Gen. Rel. Grav. **22**, 349 (1990)

[36] D. Hobill, D. Bernstein, M. Welge, and D. Simkins, ‘The mixmaster cosmology as a dynamical system’, Class. Quantum Grav. **8**, 1155 (1991).

[37] K. Ferraz, G. Francisco, and G.E.A. Matsas, ‘Chaotic and nonchaotic behavior in mixmaster dynamics’, Phys. Lett. A **156**, 407 (1991).

[38] A. Burd and R. Tavakol, ‘Invariant Lyapunov exponents and chaos in cosmology’, Phys. Rev. D **47**, 5336 (1993).

[39] M. Szydlowski, ‘Toward an invariant measure of chaotic behavior in general relativity’, Phys. Lett. A **176**, 22 (1993).

[40] M. Biesiada, ‘Searching for invariant description of chaos in general relativity’, Class. Quantum Grav. **12**, 715 (1995).

[41] G. Contopoulos, B. Grammaticos, and A. Ramani, ‘The last remake of the mixmaster universe model’, J. Phys. A **28**, 5313 (1995).

[42] N.J. Cornish and J.J. Levin, ‘Mixmaster universe is chaotic’, Phys. Rev. Lett. **78**, 998 (1997).

[43] G. Francisco and G.E.A. Matsas, ‘Qualitative and numerical study of Bianchi IX models’, Gen. Rel. Grav. **20**, 1047 (1988).

[44] M.A. Castagnino, H. Giacomini, and L. Lara, ‘Qualitative dynamical properties of a spatially closed FRW universe conformally coupled to a scalar field’, Phys. Rev. D **63**, 44003 (2001).

[45] G.A. Monerat, H.P. de Oliveira, and I.D. Soares, ‘Chaos in preinflacionary Friedmann-Robertson-Walker universes’ Phys. Rev. D. **58**, 063504 (1998).

[46] R. McGehee, ‘A stable manifold theorem for degenerate fixed points with applications to celestial mechanics’, J. Diff. Eqns. **14**, 70 (1973).

[47] Z. Xia, ‘Melnikov method and transversal homoclinic points in the restricted three-body problem’, J. Diff. Eqns. **96**, 170 (1992).

[48] H. Dankowicz and P. Holmes, 'The existence of transverse homoclinic points in the Sitnikov problem', J. Diff. Eqns. **116**, 468 (1995).

[49] J. Binney and S. Tremaine, *Galactic Dynamics* (Princeton University Press, Princeton, 1987).

[50] H.C. Ferguson, N.R. Tanvir, and T. von Hippel, 'Detection of intergalactic red-giant-branch stars in the Virgo cluster', Nature **391**, 461 (1998).

[51] A.P.S. de Moura and C. Grebogi, 'Output functions and fractal dimensions in dynamical systems', Phys. Rev. Lett. **86**, 2778 (2001).

[52] T. Tél, 'Thermodynamics of chaotic scattering at abrupt bifurcations', Phys. Rev. A **44**, 1034 (1991).

[53] H.E. Nusse and J.A. Yorke, 'A procedure for finding numerical trajectories on chaotic saddles', Physica D **36**, 137 (1989).

[54] Z. Toroczkai, G. Karolyi, A. Pentek, T. Tél, and C. Grebogi, 'Advection of active particles in open chaotic flows', Phys. Rev. Lett. **80**, 500 (1998).

[55] S. Bleher, C. Grebogi, E. Ott, and R. Brown, 'Fractal boundaries for exit in Hamiltonian-dynamics', Phys. Rev. A **38**, 930 (1988).

[56] K. Zyczkowksi and Y.C. Lai, 'Devil-staircase behavior of dynamical invariants in chaotic scattering', Physica D **142**, 197 (2000).

[57] S.T. Dembinski, A.J. Makowski, and P. Peplowski, 'Asymptotic-behavior of a particle in a uniformly expanding potential well', J. Phys. A **28**, 1449 (1995).

[58] F. Christiansen and P. Grassberger, 'Escape and sensitive dependence on initial conditions in a symplectic repeller', Phys. Lett. A **181**, 47 (1993).

A

Homoclinic crossing in open systems: Chaos in periodically perturbed monopole + quadrupolelike potentials

---

Patricio S. Letelier, Adilson E. Motter, Physical Review E **60**, 3920 (1999).

The Melnikov method is applied to periodically perturbed open systems modeled by an inverse–square–law attraction center plus a quadrupolelike term. A compactification approach that regularizes periodic orbits at infinity is introduced. The (modified) Smale-Birkhoff homoclinic theorem is used to study transversal homoclinic intersections. A larger class of open systems with degenerated (non-hyperbolic) unstable periodic orbits after regularization is also briefly considered.

PACS numbers: 05.45.-a, 45.05.+x, 95.10.Ce.

A.1 Introduction

Since the pioneering work of Poincaré [1] in celestial mechanics in which the mathematical basis of deterministic chaos in compact phase space systems was laid down, the study of homoclinic phenomena in closed systems with hyperbolic unstable periodic orbits has allowed the understanding of a rich variety of nonlinear effects in physics, chemistry, and biology [2]. Due to its universality, models in which unstable periodic orbits are subjected to small periodic perturbations has become one of the main paradigms of deterministic chaos [3]. An analytical tool to study such models is the Melnikov method [4, 5, 6] in connection with Smale-Birkhoff homoclinic theorem [7, 8], and Kolmogorov-Arnold-Moser (KAM) theory in the Hamiltonian case [9].

The Melnikov function describes the transversal distance between the stable and unstable manifolds associated to an unstable periodic orbit. Its isolated odd zeros indicate transversal intersections between these manifolds, and hence the onset of chaos [10]. Examples of applications of the Melnikov method in gravitation are the motion of particles in perturbed two- and three-dimensional Stäckel potentials [11, 12], the chaotic evolution of cosmological models [13], the study of orbits around a black hole perturbed by either gravitational radiation [14] or an external quadrupolar shell [15], and the bounded motion of particles in a periodically perturbed attractive center described by a monopole plus a quadrupolelike potential were considered in Ref. [16].

The Melnikov method has also been used in many other branches of physics. We find examples of applications of this method to the study of Josephson junctions [17, 18], planar periodic vortical flows [19], solitons [20], liquid crystals [21], and transfer dynamics of quasiparticles [22].

Even for Hamiltonian systems fundamental questions about chaos in noncompact phase space systems remain to be answered. Among the more important unsolved questions are the notion of chaos itself and the lack of an adequate theory to deal with it. Partial results obtained in this area are the fractal techniques in scattering processes [23], these are numerical techniques that present some difficulties due to the existence of different time scales for nearly bounded scattering. They are inadequate to the study of chaotic behavior arising from separatrices between bounded and unbounded orbits. Furthermore, they are unable to present a complete description of the chaotic motion as the one provided by analytical methods in the closed system case.

The aim of this paper is to study the homoclinic phenomenon for a class of open systems that by a suitable change of coordinates can be approached in terms of an adequate formulation of the Melnikov method and Smale-Birkhoff homoclinic theorem. The change of coordinates regularizes the unstable periodic orbit at infinity and it compactifies the region of interest of the phase space; however, the phase space as a whole remains noncompact. Alas the resulting unstable periodic orbit is typically nonhyperbolic and the standard stable manifold theorem, needed to state the Melnikov method [10], does not apply. McGehee [24] extended this theorem to degenerated cases in the context of the Newtonian three body problem. Xia [25], and Dankowicz and Holmes [26], among others, used McGehee's result in connection with Melnikov method and Smale-Birkhoff homoclinic theorem to study the nonintegrability of the three body problem.

Here we consider the equatorial motion of a particle moving in a potential described by a monopolar term plus a quadrupolelike contribution. This potential models the gravitational attraction of a galaxy bulge or any nonspherical celestial body; it also arises in general relativity in the study of the motion of a test particle around a Schwarzschild black hole, the quadrupole term being a general relativistic effect associated to the angular momentum of the particle in the reduced two-dimensional phase space, see for instance Ref. [27].

In Sec. A.2 the fixed saddle points associated to the monopole plus quadrupole system, as well as the coordinate transformation that regularizes these points at infinity, are studied. In the next section we present some mathematical preliminaries and the Melnikov method. The equations of motion are used to reduce this method to the analysis of simple graphics. We find that the perturbation induces transverse homoclinic orbits in some ranges of the parameters, and we apply the modified Smale-Birkhoff homoclinic theorem to verify the presence of a symbolic dynamics equivalent to a Smale horseshoe map; see Ref. [10]. In Sec. A.4 the study of the motion is completed with a presentation of Poincaré sections that reveal different levels of chaotic behavior as a function of the parameters. Finally, in the last section, we make some remarks about the class of system in which the same kind of analysis can be performed.

A.2 The homoclinic orbit and perturbations

We shall consider the orbit of a particle in a plane under the influence of a force modeled by a potential with inverse square law plus a quadrupolelike term. It is convenient to work with dimensionless quantities. The motion of the particle is described by [16]

$$H_0 = \frac{p^2}{2} + \frac{1}{2r^2} - \frac{1}{r} - \frac{\beta}{r^3} \quad \left(p = \frac{dr}{dt}\right), \tag{A.1}$$

where r, p, t, H_0, and β are dimensionless quantities proportional to, respectively, the radius, the radial momentum, the time, the Hamiltonian function, and the quadrupole moment of the attraction center. The effective potential

$$V_{eff} = \frac{1}{2r^2} - \frac{1}{r} - \frac{\beta}{r^3}, \tag{A.2}$$

is presented in Fig. A.1 for different values of the parameter $\beta \geq 0$.

The natural space to study a periodically perturbed planar system is $I\!R^2 \times S^1$, where the unstable periodic orbits have a proper meaning [10]. In the corresponding unperturbed autonomous case the phase space is in $I\!R^2$ and the unstable periodic orbits reduce to fixed saddle points. The unstable periodic orbits are also reduced to fixed saddle points for the maps defined on Poincaré sections $I\!R^2 \times \{t_0\} \subset I\!R^2 \times S^1$.

The above system presents a homoclinic loop associated to the hyperbolic fixed saddle point at $(r,p) = (r_M, 0)$, where $1/r_M = 1/6\beta + \sqrt{(1/6\beta)^2 - 1/3\beta}$, for β limited by $1/16 < \beta < 1/12$. This case is important in the study of bounded orbits and was explored in Ref. [16].

In the present work we study the instabilities of unbounded orbits, the relevant values of the parameter are $\beta = 1/16$ and $0 \leq \beta < 1/16$. Let $H_0 = 0$, if $\beta = 1/16$ the points $r = r_M = 1/4$ and $r = \infty$ on the r axis represent fixed points such that the particle takes infinity time to reach to or to depart from each of these points. For zero energy still, if $0 \leq \beta < 1/16$ the motion of the particle is restricted to the region between $r = r_-$ and $r = \infty$, where $1/r_- = 1/4\beta - \sqrt{(1/4\beta)^2 - 1/\beta}$, and only the last point represents a fixed point in this range of values of β.

Since the orbits of interest are in a semi-infinity region bounded away from the origin, we can compactify this part of the phase space with a change of the position coordinate like $r = u^\alpha$ with $\alpha < 0$. We find that the transformation $r = 1/u^2$ allows us to model the problem in a way similar to Refs. [24, 25, 26]. This new coordinate regularizes the fixed point at infinity that now is at the point $(u,p) = (0,0)$. The zero energy orbits generate a heteroclinic loop for $\beta = 1/16$ associated to the hyperbolic fixed saddle point at $(u,p) = (2,0)$ and the degenerated fixed saddle point at $(u,p) = (0,0)$, and a homoclinic loop for $0 \leq \beta < 1/16$ associated to the degenerated fixed saddle point at $(u,p) = (0,0)$. Degenerated in the sense that both eigenvalue of the linearized vector field are zero, as can be seen from the Hamiltonian equations

$$\frac{du}{dt} = -\frac{1}{2}u^3 p, \tag{A.3}$$

$$\frac{dp}{dt} = -u^4 + u^6 - 3\beta u^8. \tag{A.4}$$

The points $(u,p) = (2,0)$ and $(u,p) = (0,0)$ correspond to, respectively, the hyperbolic fixed saddle point at $(r,p) = (1/4,0)$ for $\beta = 1/16$ and the degenerated fixed saddle point at $(r,p) = (\infty,0)$ for $0 \leq \beta \leq 1/16$. The homoclinic and heteroclinic loops are defined by the intersection between the stable and unstable manifolds on the (u,p) plane. The homoclinic loop for $\beta = 1/18$ is shown in Fig. A.2 and the heteroclinic one is presented in Fig. A.3.

The explicit integration of the homoclinic and heteroclinic loops will be necessary to apply the Melnikov method and can be obtained from the first integral of motion ($H_0 = 0$). For $\beta = 0$ we find

$$t(v) = \pm\frac{(1+v)(2-v)^{1/2}}{3v^{2/3}}, \tag{A.5}$$

where $v = 1/r$, the time origin is take in the symmetry point of loop, and the sign refers to the upper $(+)$ and lower $(-)$ parts of the loop. Analogously, for $0 < \beta < 1/16$ it reads

$$t(v) = \pm\sqrt{\frac{2}{\beta}}\left\{\frac{(2v_+ + v_-)F(\delta,q) - 2(v_+ + v_-)E(\delta,q)}{3v_-^2 v_+^{3/2}} + \frac{v_+v_- + (2v_+ + v_-)v}{3v_+v_-^2}\sqrt{\frac{v_- - v}{(v_+ - v)v^3}}\right\} \tag{A.6}$$

with

$$\delta = \arcsin\sqrt{\frac{v_+(v_- - v)}{v_-(v_+ - v)}}, \qquad q = \sqrt{\frac{v_-}{v_+}}\,, \tag{A.7}$$

where $F(\delta, q)$ and $E(\delta, q)$ are elliptic integrals of first and second type in the Legendre normal form (Ref. [28], p. 224), and $v_\pm = 1/4\beta \pm \sqrt{(1/4\beta)^2 - 1/\beta}$ are the roots of $V_{eff} = 0$. Moreover, for $\beta = 1/16$ we get

$$\begin{aligned} t(v) = \pm \Bigg\{ & \frac{\sqrt{2}}{3}\left(\frac{1}{v^{3/2}} - \frac{1}{(4/3)^{3/2}}\right) + \frac{1}{2\sqrt{2}}\left(\frac{1}{\sqrt{v}} - \frac{1}{\sqrt{4/3}}\right) \\ & + \frac{1}{8\sqrt{2}} \ln\left[\left(\frac{2-\sqrt{v}}{2+\sqrt{v}}\right)\left(\frac{2+\sqrt{4/3}}{2-\sqrt{4/3}}\right)\right]\Bigg\} \end{aligned} \tag{A.8}$$

with the choice $t(4/3) = 0$, where $v = 4/3$ is the local minimum of V_{eff}.

Now, let us consider the Hamiltonian (A.1) perturbed by a periodic multipolar term of the form

$$H = H_0 + \varepsilon H_1, \tag{A.9}$$

$$H_1 = r^{-n}\cos(\Omega t) \quad (n \geq 2), \tag{A.10}$$

where $n = 2$ is dipolar, $n = 3$ is quadrupolar, etc. These perturbations can model the attraction due to a distribution of masses with periodic motions that are placed inside the planet orbit.

We shall consider our attraction center with a fix total mass. In other words, we excluded the monopolar case ($n = 1$) that represents a periodic variation of the mass.

In the next sections we study how these perturbations can affect the dynamics of the system.

A.3 Melnikov method

Powerful tools to study near integrable systems are Melnikov type of techniques that detect transversal intersections between the stable and unstable manifolds associated to a unstable periodic orbit. The presence of such transversal intersections is a guarantee of complicated dynamics and in some cases leads to a symbolic dynamics equivalent to the Smale horseshoe [10].

In order to simplify the analysis it is convenient to abstract a little from the particular problem presented above. In what follows the loops are on the X plane and the manifolds are in the (X,θ) space, where $\theta \equiv t \bmod 2\pi/\Omega$ so that $(X,\theta) \in I\!R^2 \times S^1$, and Σ_{θ_0} denotes the section $\theta = \theta_0$. We consider a Hamiltonian of the form

$$\tilde{H}(X,t) = \tilde{H}_0(X) + \varepsilon \tilde{H}_1(X,t) \quad (\tilde{H}_1 \ 2\pi/\Omega-\text{periodic in } t), \tag{A.11}$$

where $\tilde{H}_0$ is integrable with homoclinic (heteroclinic) loop Γ associated to some *hyperbolic* fixed saddle point(s). Under hyperbolicity hypothesis it can be shown that for sufficiently small ε the invariant manifolds are only deformed, and possibly their intersections become transversal, see for instance Ref. [10].

Let X_0 be a point on Γ and $X^{s/u}(\theta_0,\varepsilon)$ be points on the stable/unstable manifolds such that they are on Σ_{θ_0}, in the line perpendicular to $\Gamma \times \{\theta_0\}$ at X_0 and whose trajectories take the least amount of time to reach/depart any small neighborhood of the unstable periodic orbit. A computable measure of the transversal distance between the stable and unstable manifolds on Σ_{θ_0}, which defines the Melnikov function, is given by the zero order term of $1/\varepsilon[\tilde{H}_0(X^u(\theta_0,\varepsilon)) - \tilde{H}_0(X^s(\theta_0,\varepsilon))]$ [29]. In fact, if $X^{s/u}(t;\theta_0,\varepsilon)$ denotes the time evolution under $\tilde{H}$ such that $X^{s/u}(\theta_0;\theta_0,\varepsilon) = X^{s/u}(\theta_0,\varepsilon)$, and $X_0(t)$ denotes the time evolution under $\tilde{H}_0$ such that $X_0(0) = X_0$,

$$\begin{aligned}\tilde{H}_0(X^{s/u}(\theta_0,\varepsilon)) - \tilde{H}_0(X^{s/u}(\pm\infty;\theta_0,\varepsilon)) &= \int_{\pm\infty}^{\theta_0} \frac{d\tilde{H}_0}{dt}\left[X^{s/u}(t;\theta_0,\varepsilon)\right] dt \\ &= \int_{\pm\infty}^{\theta_0} \frac{d\tilde{H}_0}{dt}\left[X_0(t-\theta_0),t\right] dt + O(\varepsilon^2).\end{aligned} \tag{A.12}$$

Thus in the homoclinic case the Melnikov function can be written as

$$M(\theta_0) = \frac{1}{\varepsilon}\int_{-\infty}^{\infty} \frac{d\tilde{H}_0}{dt}\left[X_0(t), t+\theta_0\right] dt, \quad \left(\frac{1}{\varepsilon}\frac{d\tilde{H}_0}{dt} = \{\tilde{H}_0, \tilde{H}_1\}\right), \tag{A.13}$$

where $\{\ .\ ,\ .\ \}$ are the usual Poisson brackets.

The implicit function theorem allows us to conclude that if $M(\theta_0)$ has simple zeros, then, for sufficiently small ε the invariant manifolds intersect transversely for some θ_0. On the other hand, if $M(\theta_0)$ is bounded away from zero, then the invariant manifolds do not intersect for all θ_0.

Now let us take the map defined by system (A.3)-(A.4) on a arbitrary section. After a scale change in the p coordinate it reads

$$u_{k+1} = u_k - Cu_k^3 \left[p_k + O(4) \right], \tag{A.14}$$

$$p_{k+1} = p_k - Cu_k^3 \left[u_k + O(3) \right], \tag{A.15}$$

where $C = \sqrt{2}\pi/\Omega$. Here the standard Melnikov method breaks down because of the degeneracy of the saddle point. McGehee [24], Xia [25], Dankowicz and Holmes [26] studied systems of this class in the context of the three body problem, where they established the fundamental results needed to support the Melnikov method: structural stability of the unstable periodic orbits (trivial in our case since the degenerated unstable periodic orbit remains fixed); existence of local stable and unstable analytic manifolds C^∞ close to those of the unperturbed case [24, 26]; solutions on the perturbed and the unperturbed manifolds approach to the unstable periodic orbit at a similar rate [25, 26]. Following the proofs step-by-step we can observe that all the essential hypothesis involved to achieve their results are also satisfied by the above system. Thus these statements apply to Eqs. (A.14)-(A.15) allowing the expansion in Eq. (A.12) that justifies the use of Melnikov method in the present problem.

Another important result whose standard form assumes hyperbolicity is the Smale-Birkhoff homoclinic theorem. It was given a formulation of this theorem that is valid for the degenerated problem of Sitnikov [26], which is grounded on a suitable approximation of the linearization of the map in the neighborhood of the saddle point. Since such approximation results in the same expressions for the case of Eqs. (A.14)-(A.15), we conclude that the Smale-Birkhoff homoclinic theorem applies to the above system. Thus transversal homoclinic intersections in our problem lead to the Smale horseshoe.

Now we shall apply Melnikov method to Eq. (A.1) subjected to the perturbations (A.10). In the homoclinic case ($0 \leq \beta < 1/16$) we find for the Melnikov function

$$\begin{aligned} M(\theta_0) &= \int_{-\infty}^{+\infty} nr^{-n-1} \cos[\Omega(t+\theta_0)] \frac{dr}{dt} dt \qquad (A.16) \\ &= -2n \sin(\Omega\theta_0) K(\Omega), \\ K(\Omega) &\equiv \int_0^{v_-} v^{n-1} \sin[\Omega t(v)] dv, \qquad (A.17) \end{aligned}$$

where we have fixed $X_0 = [v(0), p(0)]$ as the symmetry point on the loop and the integrand $t(v)$ means the positive branch of Eqs. (A.5)-(A.6). Thus the Melnikov function has simple zeros as long as $K(\Omega) \neq 0$. With the change $t \to v$ we pass from an infinite interval in Eq. (A.16) to a finite one in Eq. (A.17), and it allows us to study $K(\Omega)$ using graphics. Although u ($r = 1/u^2$) is important to justify the Melnikov method, we have great freedom in the choice of a coordinate to study the results. The most simple one that is adequate to this end is the coordinate $v = 1/r$.

The integrand of $K(\Omega)$ is formed by the product of an oscillating function and a polynomial. Near the origin this oscillation is a rapid one, since $t \longrightarrow \infty$ as the particle goes to the unstable periodic orbit. In Fig. A.4 we show a graph of $\sin[\Omega t(v)]$ for $\beta = 1/25$, and several values of Ω. For $\Omega > 4$ we will have more zeros in the interval shown in the figure. For $\Omega < 1$ the curve will look like the one for $\Omega = 1$. Since the area under the curves are clearly not null the integral of $\sin[\Omega t(v)]$ is nonzero for $\beta = 1/25$ and $0 < \Omega \leq 4$. The cases of interest are $n \geq 2$, where we will have a more favorable situation. We have transverse homoclinic orbits in all these cases. To better understand this behavior we show in Fig. A.5 a graph of the integrand of $K(\Omega)$ for $\beta = 1/25$, $\Omega = 3$ and different values of n. For $0 \leq \beta < 1/16$ the graphics of $\sin[\Omega t(v)]$ will look like the one for $\beta = 1/25$, with almost the same upper bound for Ω. See for instance Fig. A.6, where we plot the graphics of $\sin[\Omega t(v)]$ for the monopolar attraction center ($\beta = 0$) for the same values of Ω employed in Fig. A.4. Therefore we have transverse homoclinic orbits for all β limited by $0 \leq \beta < 1/16$.

For these range of parameters the Smale-Birkhoff homoclinic theorem implies the existence of a hyperbolic invariant set for which the action of an Nth iterate of the map has a symbolic dynamic equivalent to that of the Smale horseshoe map. Some important consequences of this result are sensitive dependence on initial condition (a characteristic of chaos); nonexistence of real analytic integral of motion (nonintegrable system); existence of infinitely many periodic orbits with arbitrary large periods (whose number increases exponentially with the period); capture of orbits by the system (in both directions of time).

It is illustrative to see how the chaotic orbits look in the original noncompactified coordinates r, p. Due to the lack of an extra integral of motion the particle can have a highly erratic motion and have access to a two dimensional region of the phase space. The sensitive dependence on initial condition implies that the evolution of two infinitesimally near points in the space r, p can result in two completely different bounded orbits, in two completely different unbounded orbits, or even in one bounded and one unbounded orbit. Orbits that are bounded for all $t < 0$ can go to infinite for $t \longrightarrow +\infty$, and orbits of particles coming from infinite can remain bounded for all $t > 0$. However, regular orbits are also present and in particular there is a family of periodic orbits.

Let us consider the heteroclinic case $\beta = 1/16$. The Melnikov method obtained from Eq. (A.12) applies to each branch of the loop. The distance between $X^{s/u}(\pm\infty; \theta_0, \varepsilon)$ and $X^{s/u}(\pm\infty; \theta_0, 0)$ is of order $O(\varepsilon)$. Therefore $H_0(X^{s/u}(\pm\infty; \theta_0, \varepsilon))$ is of order $O(\varepsilon^2)$. Then, this term can be neglected and the Melnikov function reads

$$M(\theta_0) = 2n \sin(\Omega\theta_0) K_s(\Omega) - 2n \cos(\Omega\theta_0) K_c(\Omega), \tag{A.18}$$

$$K_s(\Omega) \equiv \int_0^{v_-} v^{n-1} \sin[\Omega t(v)] dv, \quad K_c(\Omega) \equiv \int_0^{v_-} v^{n-1} \cos[\Omega t(v)] dv. \tag{A.19}$$

The orbits in the heteroclinic loop are less symmetrical than in the homoclinic one and, consequently, the Melnikov function has simple zeros when at least one of the integrals of the previous formula is different from zero. The integrands of K_s and K_c oscillate very rapidly near the unstable periodic orbits. To better understand this behavior we show in Fig. A.7 a graphic of the positive branch of Eq. (A.8). The function $t(v)$ has small values for a large range of values of v, and hence K_c will result nonzero values for small Ω. Indeed, we show in Fig. A.8 a graph of $\cos[\Omega t(v)]$ for different values of Ω. Since cosine is an even function, the same figure is valid for the negative branch. For $\Omega > 3$ we will have more zeros in the interval $1 < v < 4$. For $\Omega < 0.5$ the curves will look like the one for $\Omega = 0.5$. For small values of n the integral K_c will be nonzero for $0 < \Omega \leq 3$. Due to the change of sign of $\cos[\Omega t(v)]$ near $v = 4$, the upper bound for Ω decrease with n. But it is clear from Fig. A.8 that for each n will exist a upper bound $\Omega_o(n) > 0$ such that K_c will be nonzero, leading to the presence of transversal heteroclinic orbits, for $0 < \Omega \leq \Omega_o(n)$.

A.4 Poincaré sections method

The system (A.9) has four parameters, β, n, Ω, and ε. In opposition to the Melnikov method, Poincaré sections method is able to predict results only for fixed values of these parameters. However, the Poincaré method can locate the regular and irregular regions and provide a qualitative idea of chaotic behavior.

The perturbed phase space is in $I\!R^2 \times S^1$ and the maps defined on different values of the angular variable $\theta = t \bmod 2\pi/\Omega$ are topologically conjugated. So we have restricted the study to sections built on $\theta = 0$, but for a large number of different values of the parameters β, n, Ω, and ε. We included Ω values which would require a more elaborate numerical computation of the Melnikov function. In Fig. A.9 we show the Poincaré sections for some select values of β, n, Ω, and ε. The general aspect of the sections is represented in this figure, with the predominance of irregular behavior near the destroyed invariant loop and the presence of a regular region near the center.

A careful analysis of the Poincaré sections reveals that chaos increases with n, which is natural since the major contribution of the perturbation comes from $v > 1$. In Figs. A.9(a) and A.9(b) we show the Poincaré sections for $n = 2$ and $n = 5$, respectively, where $\beta = 1/25$, $\Omega = 1$, and $\varepsilon = 0.003$. As a function of Ω, the most chaotic behavior occurs for frequencies of the same order of the angular frequencies of the orbits in the local minimum of V_{eff}, from $(4/3)^2$ for $\beta = 1/16$ to 1 for $\beta = 0$. It is a reasonable result since for small Ω the system is almost autonomous, and for large frequencies the particle feels only an average of the multipolar motion that goes to zero for $\Omega \longrightarrow \infty$. In Figs. A.9(a), A.9(c), and A.9(d) we show Poincaré sections for $\Omega = 1$, $\Omega = 0.1$, and $\Omega = 5$, respectively, where $\beta = 1/25$, $n = 2$, and $\varepsilon = 0.003$. Also, the chaos increases strongly with the "size" of the perturbation ε. In Figs. A.9(a) and A.9(e) we show the Poincaré sections for $\varepsilon = 0.003$ and $\varepsilon = 0.01$, respectively, where $\beta = 1/25$, $n = 2$, and $\Omega = 1$.

The form of the orbits change with β, since there is a change in the destroyed loop, but the relative chaotic area of the section is almost independent of the value of β. In Figs. A.9(a), A.9(f), and A.9(g) we show the Poincaré sections for $\beta = 1/25$, $\beta = 0$ and $\beta = 1/16$, respectively, where $n = 2$, $\Omega = 1$ and $\varepsilon = 0.003$. In particular, the case $\beta = 1/16$

presents two unstable periodic orbits and no higher chaotic behavior seems to be associated to it.

A.5 Final remarks

Making use of a compactification procedure and extensions of the standard Melnikov method and Smale-Birkhoff homoclinic theorem, we have detected transverse homoclinic and heteroclinic orbits and Smale horseshoe in periodically perturbed monopole + quadrupole-like potential. Moreover the compactified coordinates have proved useful to work out the Poincaré section method.

Although we have studied only one particular system, we stress that the approach is general and can be applied to a large class of open systems. The mathematical results depend essentially on the presence of the monopolar term in the unperturbed equations. Thus the same approach and with the same compactification applies to every inner-multipolar expansion model with nonzero monopolar contribution. In such cases we can allow non-Hamiltonian perturbations of the form $f(u, t, \varepsilon)$ in the equation corresponding to Eq. (A.4), where f is an analytic function of its variables, periodic in t, satisfying $f(u, t, 0) = 0$ and of order $O(u^6)$.

These systems represent very general situations. In the gravitational case, for instance, they can model a potential due to a mass distribution moving periodically with reflection symmetry. This includes all planar potential written as Fourier expansion in time together with an inner-multipolar expansion in space variable. A specific example is provided by a Newtonian binary system perturbed by gravitational radiation. This system models the long-term dynamical evolution of binary systems of stars due to the emission and absorption of gravitational radiation [30].

In electromagnetic systems we can have a different situation. The possible absence of monopolar contribution creates a difficulty in transforming the map equations into the analytic form (A.14)-(A.15). The solution may be found using the Cassasayas-Fontich-Nunes's result, which establishes the Melnikov method for systems with parabolic degenerated saddle points [31]. A suitable compactification to treat the electromagnetic case is under study.

Acknowledgements

The authors are thankful to CNPq and Fapesp for financial support.

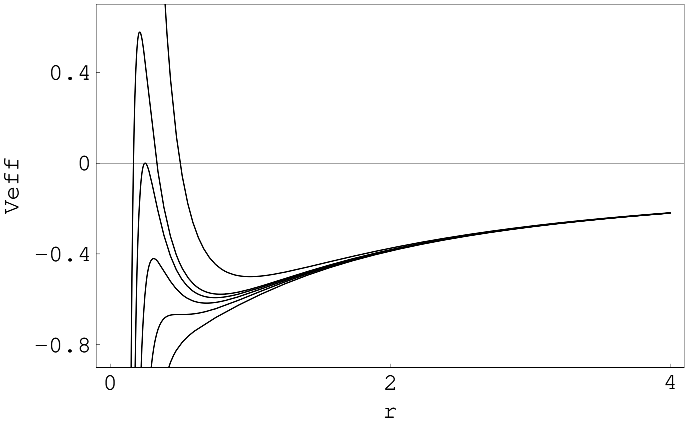

Figure A.1: The effective potential $[V_{eff}(r)]$ for $\beta = 1/10$ (bottom curve), $\beta = 1/12$, $\beta = 1/14$, $\beta = 1/16$, $\beta = 1/18$, and $\beta = 0$ (top curve), where the last one represents a monopolar potential.

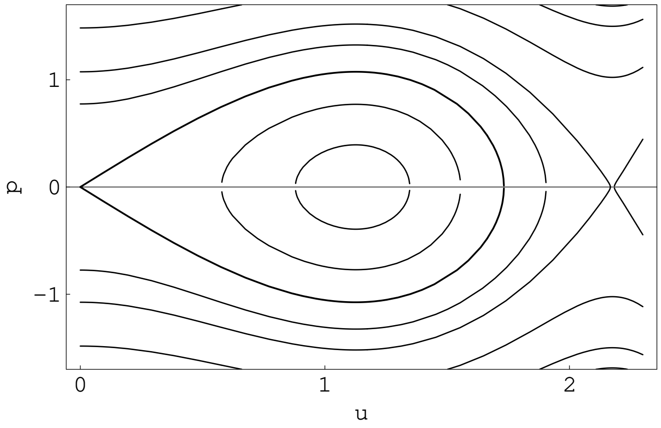

Figure A.2: The level curves of the Hamiltonian H_0 for $\beta = 1/18$. The homoclinic loop associated to $(u, p) = (0, 0)$ is the curve that contains that point.

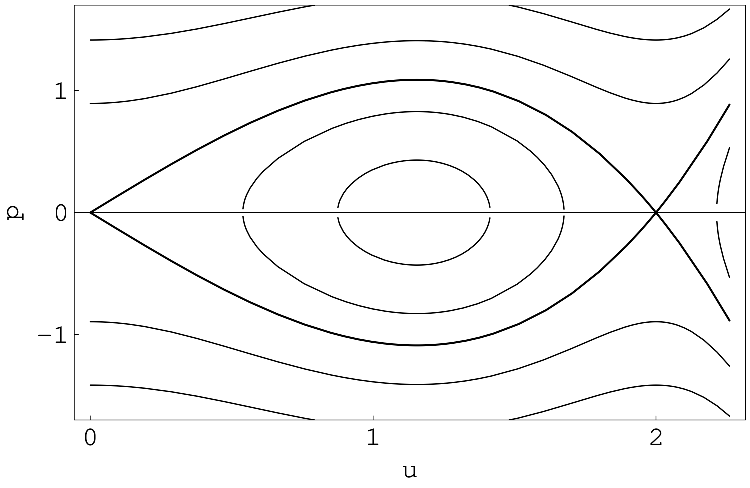

Figure A.3: The level curves of the Hamiltonian H_0 for $\beta = 1/16$. The curves that represent the invariant manifolds, which define the heteroclinic loop, associated to the points $(u, p) = (0, 0)$ and $(u, p) = (2, 0)$ are the curves that contains those points.

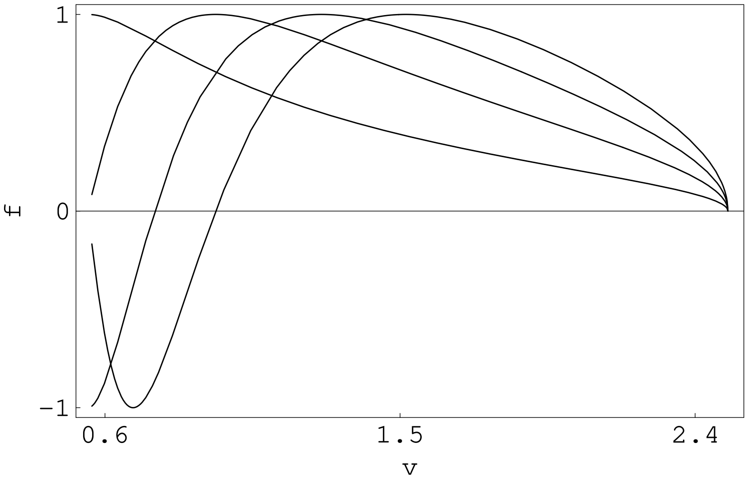

Figure A.4: $f \equiv \sin[\Omega t(v)]$ for $\beta = 1/25$, and $\Omega = 1$ (bottom curve), $\Omega = 2$, $\Omega = 3$, and $\Omega = 4$ (top curve).

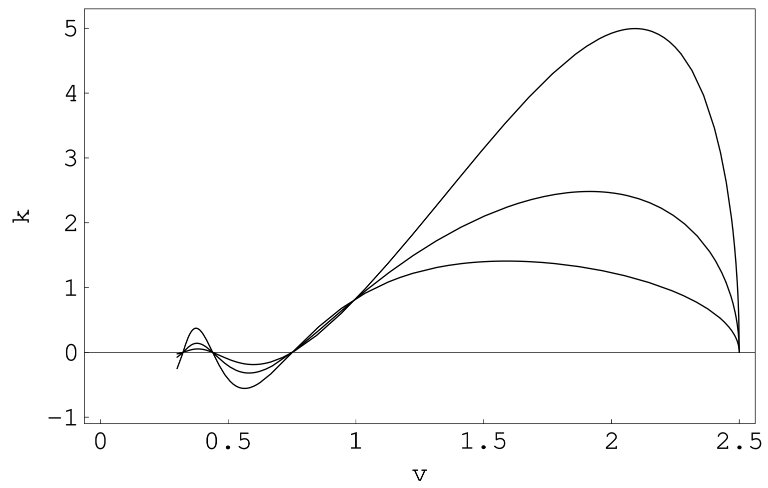

Figure A.5: The integrand $k \equiv v^{n-1} \sin[\Omega t(v)]$ of $K(\Omega)$ for $\beta = 1/25$, $\Omega = 3$, and $n = 2$ (bottom curve), $n = 3$ and $n = 4$ (top curve).

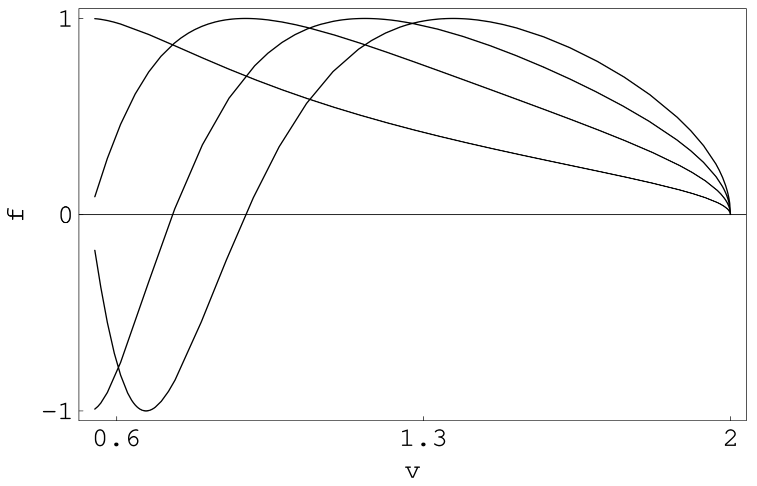

Figure A.6: $f \equiv \sin[\Omega t(v)]$ for the monopolar potential ($\beta = 0$) with $\Omega = 1$ (bottom curve), $\Omega = 2$, $\Omega = 3$, and $\Omega = 4$ (top curve).

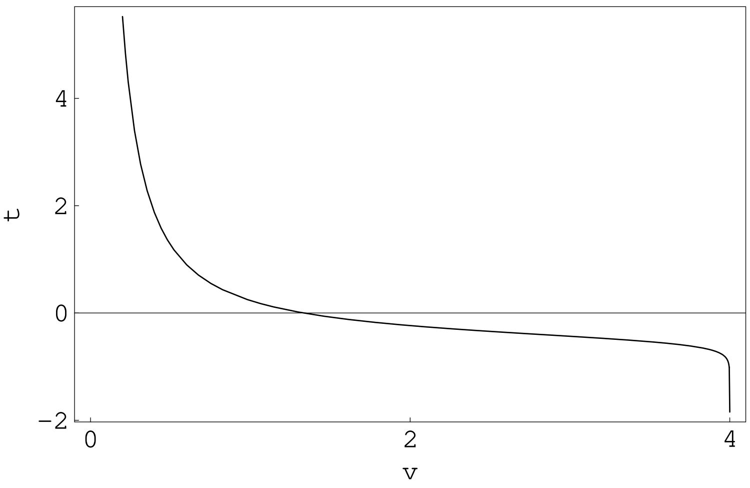

Figure A.7: The positive branch of Eq. (A.8): $t(v)$ goes to $\pm\infty$ at $v = 0$ and $v = 4$, but has small values at almost every point of the interval $0 < v < 4$.

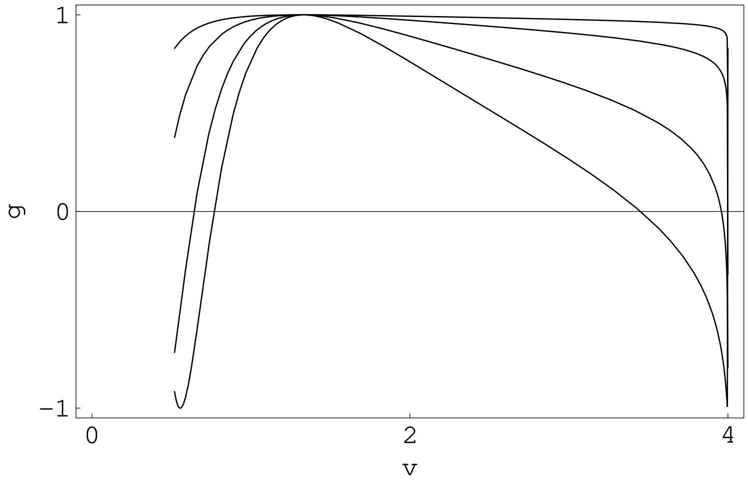

Figure A.8: $g \equiv \cos[\Omega t(v)]$ for $\beta = 1/16$, and $\Omega = 0.5$ (top curve), $\Omega = 1$, $\Omega = 2$, and $\Omega = 3$ (bottom curve).

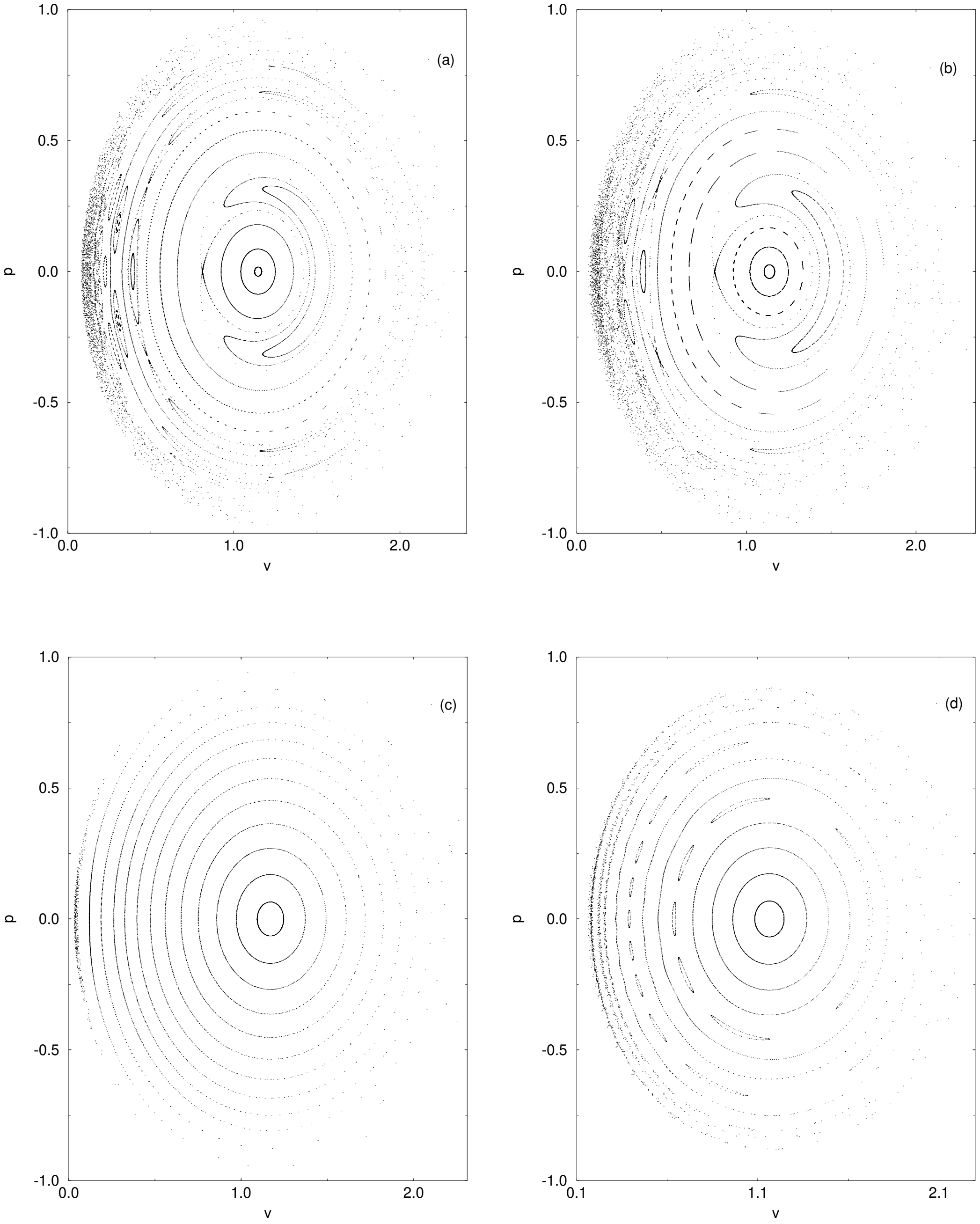

Figure A.9: The Poincaré sections for (a) $\beta = 1/25$, $n = 2$, $\Omega = 1$, and $\varepsilon = 0.003$; (b) $\beta = 1/25$, $n = 5$, $\Omega = 1$, and $\varepsilon = 0.003$; (c) $\beta = 1/25$, $n = 2$, $\Omega = 0.1$, and $\varepsilon = 0.003$; (d) $\beta = 1/25$, $n = 2$, $\Omega = 5$, and $\varepsilon = 0.003$; (e) $\beta = 1/25$, $n = 2$, $\Omega = 1$, and $\varepsilon = 0.01$; (f) $\beta = 0$, $n = 2$, $\Omega = 1$, and $\varepsilon = 0.003$; (g) $\beta = 1/16$, $n = 2$, $\Omega = 1$, and $\varepsilon = 0.003$.

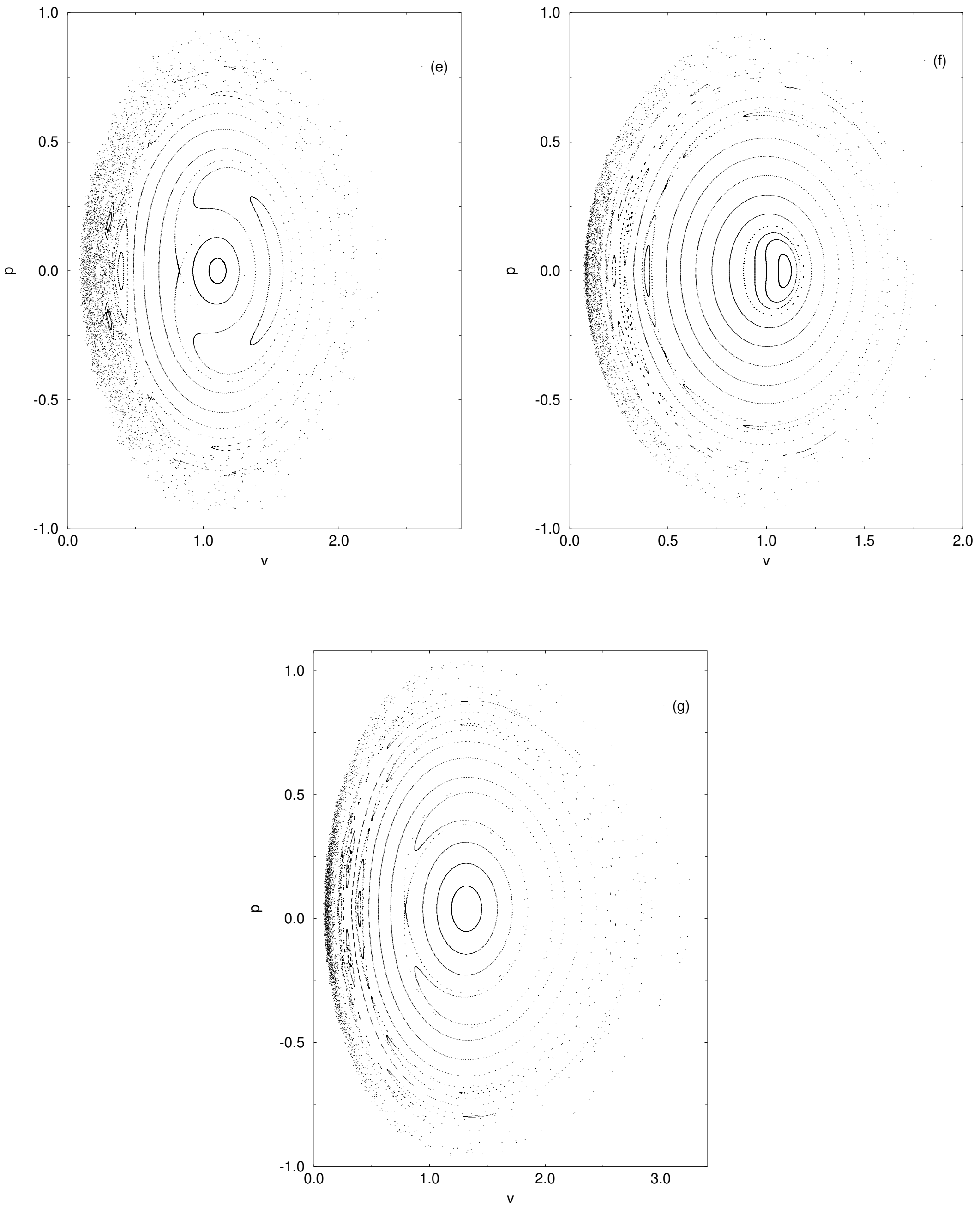

Figure A.9: (Continued).

Bibliography

---

[1] H. Poincaré, *Les Méthodes Nouvelles de la Méchanique Celeste* (Gauthier-Villars, Paris, 1899), Vols. 1-3.

[2] H. Bai-lin, *Chaos* (World Scientific, Singapore, 1982).

[3] V.I. Arnold, *Dynamical Systems*, Encyclopaedia of Mathematical Sciences Vol. III (Springer-Verlag, Berlin, 1988).

[4] H. Poincaré, Acta Math. **13**, 1 (1890).

[5] V.K. Melnikov, Trans. Moscow Math. Soc. **12**, 1 (1963).

[6] V.I. Arnold, Sov. Math. Dokl. **5**, 581 (1964).

[7] G.D. Birkhoff, *Dynamical Systems* (A.M.S. Publications, Providence, RI, 1927).

[8] S. Smale, in: *Differential and Combinatorial Topology*, edited by S.S. Carins (Princeton University Press, Princeton, 1963), p. 63.

[9] J. Moser, *Stable and Random Motions in Dynamical Systems* (Princeton University Press, Princeton, 1973) and references therein.

[10] J. Guckenheimer and P. Holmes, *Nonlinear Oscillations, Dynamical Systems, and Bifurcations of Vector Fields* (Springer-Verlag, New York, 1983).

[11] O.E. Gerhard, Astron. Astrophys. **151**, 279 (1985).

[12] O.E. Gerhard, Mon. Not. R. Astron. Soc. **222**, 287 (1986).

[13] J. Koiller, J.R.T.D. Neto, and I.D. Soares, Phys. Lett. A **110**, 260 (1985).

[14] P.S. Letelier and W.M. Vieira, Class. Quantum Grav. **14**, 1249 (1997).

[15] R. Moeckel, Commun. Math. Phys. **150**, 415 (1992).

[16] P.S. Letelier and W.M. Vieira, Phys. Lett. A **242**, 7 (1998).

[17] X. Yao, J.Z. Wu, and C.S. Ting, Phys. Rev. B **42**, 244 (1990).

[18] A. Kenfack and T.C. Kofané, Phys. Rev. B **52**, 10359 (1995).

[19] T. Ahn and S. Kim, Phys. Rev. E **49**, 2900 (1994).

[20] F.Kh. Abdullaev, S.A. Darmanyan, and B.A. Umarov, Phys. Rev. A **41**, 4498 (1990).

[21] I.W. Stewart, T. Carlsson, and F.M. Leslie, Phys. Rev. E **49**, 2130 (1994).

[22] D. Hennig and B. Esser, Phys. Rev. A **46**, 4559 (1992).

[23] E. Ott, *Chaos in Dynamical Systems* (Cambridge University Press, Cambridge, 1994).

[24] R. McGehee, J. Diff. Eqns. **14**, 70 (1973).

[25] Z. Xia, J. Diff. Eqns. **96**, 170 (1992).

[26] H. Dankowicz and P. Holmes, J. Diff. Eqns. **116**, 468 (1995).

[27] S. Chandrasekhar, *The Mathematical Theory of Black Holes* (Oxford University Press, Oxford, 1998)

[28] I.S. Gradshteyn and I.M. Ryzhik, *Table of Integrals, Series, and Products*, 4th ed. (Academic Press, London, 1965).

[29] A.M. Ozorio de Almeida, *Hamiltonian Systems: Chaos and Quantization* (Cambridge University Press, Cambridge, 1988).

[30] C. Chicone, B. Mashhoon, and D.G. Retzloff, Class. Quantum Grav. **14**, 699 (1997).

[31] J. Casasayas, E. Fontich, and A. Nunes, Nonlinear Differ. Equ. Appl. **4**, 201 (1997).

B

Hausdorff dimension of repellers in low sensitive systems

Adilson E. Motter, Patricio S. Letelier, Physics Letters A **277**, 18 (2000).

Methods to estimate the Hausdorff dimension of invariant sets of scattering systems are presented. Based on the levels' hierarchical structure of the time delay function, these techniques can be used in systems whose future-invariant-set codimensions are approximately equal to or greater than one. The discussion is illustrated by a numerical example of a scatterer built with four hard spheres located at the vertices of a regular tetrahedron.

PACS numbers: 05.45.Df.

Usually, in a scattering process almost all particles outcome asymptotically free after interacting with a potential. Some particles, however, remain in the scattering region bouncing forever under the action of the potential. The nature of these trapped orbits is in general very intricated, including fractal dimensions and chaotic behaviour. The dimension seems to be the most fundamental quantity characterizing this set. When the dimension is large enough, scattered particles may present sensitive dependence on initial conditions reminiscent of the chaotic dynamics of the trapped orbits. This phenomenon allows the computation of the *uncertainty dimension* of the bounded orbits, defined as follows. For a scattering system, colour by black initial conditions of particles scattered, for instance, to the right-hand side of the scattering centre and by white initial conditions corresponding to particles scattered to the left-hand side. An initial condition of a given colour at a distance less than ε of initial conditions of a different colour is labelled ε-uncertain. The final state (left or right) of a particle associated to an ε-uncertain initial condition is uncertain if this point is determined only within a precision of order ε. In the limit of small ε, the fraction of such ε-uncertain points is $f(\varepsilon) \sim \varepsilon^{N-D_u}$, for N denoting the dimension of the subspace where the initial conditions are taken, and D_u the corresponding uncertainty dimension of the intersection of the trapped orbits with this subspace. Therefore D_u can be computed by fitting $\ln f(\varepsilon)$ as a function of $\ln \varepsilon$. This procedure works in systems where the set of bounded orbits has dimension greater than $N-1$ in the N-dimensional subspace of initial conditions. That is supported by the fact that in this case D_u is expected to be equal to a more general concept of dimension, the *Hausdorff dimension*.

The Hausdorff dimension of a set A is defined as follows [1]: Let S_j denote a countable collection of subsets of the Euclidean space such that the diameters ϵ_j of the S_j are all less than or equal to δ, and such that the S_j are a covering of A. We define the Hausdorff sum

$$K_\delta(d) = \inf_{S_j} \sum_{j=1} (\epsilon_j)^d, \tag{B.1}$$

where the infimum is taken on the set of all the possible countable coverings of A satisfying $\epsilon_j \leq \delta$. Then we define the d-dimensional Hausdorff measure

$$K(d) = \lim_{\delta \to 0} K_\delta(d). \tag{B.2}$$

It can be shown that $K(d)$ is infinite if d is less than some critical value D_H, and is zero if d is greater than D_H. This critical value is the Hausdorff dimension of the set A.

Among the several existing concepts of dimension, the Hausdorff dimension is the one that better implement the intuitive notion of dimension that we have in mind. Unfortunately, the uncertainty methods cannot be used to estimate D_H when its value is less than or equal to $N-1$. Even when D_H is slightly greater than $N-1$, its evaluation through the numerical computation of the uncertainty dimension is highly inaccurate. The aim of these work is to present methods to compute the Hausdorff dimension of the set of trapped orbits - the future invariant set (I_f) - when uncertainty methods do not apply. The determination of this dimension is important, for instance, to understand the onset of chaos in scattering systems when a system parameter is varied.

First in this communication, we introduce a method to take into account the infimum requirement appearing in the definition of the Hausdorff dimension, that allows the direct computation of $D_H(I_f)$. Next, the Hausdorff dimension is estimated from the box-counting dimension computed by using a proper-interior-maximum-*like* procedure. Finally, we define a new dimension, the *self-similarity dimension*, which is also used to approximate $D_H(I_f)$. Our methods can be applied for $D_H(I_f) > N-1$ as well as for $D_H(I_f) \leq N-1$. The discussion is illustrated along the text by a numerical example of a simple scattering system presenting $D_H(I_f) \leq N-1$ and $D_H(I_f) > N-1$ for two ranges of values of its control parameter.

The example we shall consider is due to Chen *et al.* [2], who investigated a system consisting of a particle bouncing between four identical hard spheres placed at the vertices of a regular tetrahedron of unit edge. The centres of the spheres are located at the coordinates $(0,\ 0,\ \sqrt{2}/3)$, $(1/2,\ -1/2\sqrt{3},\ 0)$, $(-1/2,\ -1/2\sqrt{3},\ 0)$ and $(0,\ 1/\sqrt{3},\ 0)$, and their radius R is the variable parameter of the system. These authors contributed with a procedure to directly evaluate the Hausdorff dimension $\tilde{D}_H(R)$ on 1-dimensional lines. By taking lines on the plane $P = \{z = -k\ (k > R), p_x = p_y = 0, p_z = 1\}$, they computed the Hausdorff dimension $D_H(R)$ of the intersection of I_f with P, obtaining $D_H(0.48) = 1 + \tilde{D}_H(0.48) = 1.4$. It is reasonable to presume that D_H is an increasing function of R. Here we are interested in computing D_H for small values of the radius, where the dimension of $I_f \cap P$ is expected to be less than one (codimension greater than one).

We consider initial conditions (x_0, y_0) on P, and we define the time delay function $T(x_0, y_0)$ as the number of collisions of the particle with the spheres. We also introduce $C_n = \{(x_0, y_0) \mid T(x_0, y_0) \geq n\}$. C_1 is the union of 4 discs, the projection on P of the four spheres. C_2 is the union of $4 \cdot 3 = 12$ deformed discs, the projection on P of the reflection on each sphere of the other three spheres. C_3 is the union of $4 \cdot 3^2 = 36$ deformed discs, and so on. Therefore, for sufficiently small R, C_n is the union of $4 \cdot 3^{n-1}$ deformed discs. The construction of the Cantor structure of the set $I_f \cap P = \cap_{n=1}^{\infty} C_n$ can be followed in

Fig. B.1, where we show C_1, C_2, C_3 and C_4 for $R = 0.37$.

Labelling the spheres by 1, 2, 3 and 4, the left shift symbolic dynamics of the future invariant set consists of sequences $s_1 s_2 s_3 ...$ of 1, 2, 3 and 4, where s_n is the number of the sphere of the nth collision. The particle cannot collide two successive times with the same sphere, and hence the only constraint is $s_{n+1} \neq s_n$ (at least for R small enough). A relevant point here is that each one of the $4 \cdot 3^{n-1}$ deformed discs of C_n can be identified by a sequence of collisions, $c_{n,j} = [s_1 s_2 ... s_n]$ for $j = 1, 2, ..., 4 \cdot 3^{n-1}$. It allows us to define the Hausdorff sum

$$K_n(d) = \sum_{j=1}^{4 \cdot 3^{n-1}} |c_{n,j}|^d, \tag{B.3}$$

where $|c_{n,j}|$ is the diameter of $c_{n,j}$, $|c_{n,j}| = \sup_{\vec{x},\vec{y} \in c_{n,j}} |\vec{x} - \vec{y}|$, which can be easily estimated from a sample of initial conditions. The $d-$dimensional Hausdorff measure $K(d)$ is supposed to be the limit of $K_n(d)$ for $n \to \infty$. $K(d)$ is infinite for d less than the Hausdorff dimension D_H, and is zero for d greater than D_H [1]. Since it is not known how to compute $\lim_{n\to\infty} K_n(d)$ numerically, we generalise an argument due to Ref. [2]: For n sufficiently large, the sums $K_n(d)$ for different values of n will all intersect with each other at approximately the same point $d = D_H$. It provides a method to estimate the Hausdorff dimension.

In Fig. B.2 we show $\ln K_5(d)$, $\ln K_6(d)$, $\ln K_7(d)$ and $\ln K_8(d)$ for $R = 0.37$. The curves in fact intersect approximately at the same point giving $D_H(0.37) = 0.87 \pm 0.01$. In Fig. B.3 (boxes) we show a graph of D_H computed by this method for $0.37 \leq R \leq 0.48$ (it includes regions with $D_H > 1$ and with $D_H \leq 1$). In the same figure (stars) we also show the *box-counting dimension* D_c of $\cap_{m=1}^{\infty} C_m$. D_c was calculated by approximating $\cap_{m=1}^{\infty} C_m$ by C_n for a sufficiently large n. The number of squares $N(\varepsilon)$ needed to cover C_n was counted for different values of the edge length ε, and the dimension D_c was then obtained by fitting $\ln N(\varepsilon) = -D_c \ln \varepsilon$. The comparison between D_c and D_H in Fig. B.3 suggests that $D_c(R) = D_H(R)$.

Some remarks about the computation of the box-counting dimension have to be made. The accurate evaluation of D_c requires the use of relatively small values for ε. On the other hand, C_n has to reflect the fractal property of $\cap_{m=1}^{\infty} C_m$, condition satisfied if $|c_{n,j}| < \varepsilon$ for all j. It implies the need of large values for n (we used $n = 15$ in our computations), demanding great computational efforts in finding C_n when D_c is less than one. The remedy is based on the use of a modified PIM (proper-interior-maximum) procedure[1] [3]. In the first step, we start with a sample of initial conditions on P taken at the corners of a grid. From this set we store those points that are in C_1 as well as their first neighbours. We denote the stored set by $\bar{C}_1$. In the second step, we reduce the edge length of the grid and iterate only those points of the new grid that are in the region covered by $\bar{C}_1$. Then we store the points that are in C_2 together with their first neighbours. We denote this stored set by $\bar{C}_2$, and so on. After n steps we obtain the desired approximation for C_n.

Back to Fig. B.1, in the centre of the figure we see an approximately self-similar structure. Each step of the construction of the Cantor set divides one disc in three smaller deformed discs. If we assume that the self-similarity is exact, we can introduce λ_1, λ_2 and λ_3, the linear scales by which the discs are reduced in one step. Under such hypothesis we have that Hausdorff and box-counting dimensions are equal and satisfy [4]

$$\lambda_1^D + \lambda_2^D + \lambda_3^D = 1. \tag{B.4}$$

Even through the self-similarity is not exact in our case, (B.4) is expected to provide a good estimate for D_H (and D_c). Fig. B.1 also shows that the factors by which the discs are reduced are approximately the same. It allows us to take $\lambda_1 = \lambda_2 = \lambda_3 \equiv \lambda$, and we refer to the resulting dimension

$$D_s = -\frac{\ln 3}{\ln \lambda} \tag{B.5}$$

as the *self-similarity dimension.* The computation of λ can be performed by a Monte Carlo method. We determine the areas of C_n and C_{n+1}, for a sufficiently large n, by evolving a sample of random initial conditions. An estimate of λ is then given by

$$\lambda_n = \sqrt{\frac{1}{3}\frac{\text{area}(C_{n+1})}{\text{area}(C_n)}}\ . \tag{B.6}$$

---

[1] This technique can also be employed in the computation of $|c_{n,j}|$, to calculate D_H.

A better statistics is obtained by taking λ as the average on $\lambda_n, \lambda_{n+1}, ..., \lambda_{n+k}$ for an adequate k. For the tetrahedron scatterer, the value of λ is very stable in relation to n and k, what allows us to compute a well defined λ with not much computational effort. The resulting dimension is shown in Fig. B.3 (triangles) for $0.36 \leq R \leq 0.49$ and is consistent with D_H and D_c computed directly from their definitions. We believe that D_s can be used to estimate the common value of D_H and D_c in most systems where some kind of statistical self-similarity takes place. A rigorous statement in this direction requires, however, further investigations.

The dimension (D) that we computed corresponds to the intersection of the stable manifold of the invariant set (repellor) with the plane P. In the 5-dimensional energy surface, the dimension of the stable manifold will be $d_s = 3 + D$. The time reversibility of the dynamics implies that the dimension of the unstable manifold d_u will be equal to d_s. Since the invariant set is the intersection of the stable and unstable manifolds, its dimension will be $d_i = d_s + d_u - 5 = 2D + 1$. Therefore, the dimensions d_s, d_u and d_i can be calculated by computing D with the techniques employed here. In this procedure, the critical value of the radius (R_c) where $D = 1$ ($R_c \approx 0.41$, see Fig. B.3) does not play any particular role. In this context, to claim that the dynamics of the scattering systems is chaotic for $D > 1$ ($d_i > 3$) and regular for $D \leq 1$ ($d_i \leq 3$) sounds largely a matter of semantics. What is sure is that there is a chaotic set of trapped orbits whose dimension increases with the radius R. The presence of this chaotic set prevents the existence of integrals of motion besides the energy (the system is nonintegrable).

In the computation of D_H, D_c and D_s, we explored the hierarchical structure of levels of the time delay function in order to infer the dimension of its set of singularities ($\cap_{m=1}^{\infty} C_m$). The dimension of the singularities of the time delay seems to be the most fundamental quantity that we can measure to characterise invariant sets of scattering systems. The result involves no ambiguity since it will lead unequivocally to the dimension of the future invariant set. The same is not true for basin boundaries, for instance. See Fig. B.4, where we show the basins of the tetrahedron scatterer defined by particles scattered to $x \to +\infty$ and particles scattered to $x \to -\infty$, for $R = 0.48$ (a) and $R = 0.37$ (b). The basin boundaries present smooth 1-dimensional parts on arbitrarily fine scales. These smooth parts are not on the future invariant set and, although immaterial when $R = 0.48$, they do affect the basin boundary dimension when $R = 0.37$. In this case the dimension of the fractal part $(I_f \cap P)$ is less than the dimension of the smooth parts. Smooth parts also forbid the use of uncertainty methods to estimate the dimension of the future invariant set from the time delay function. In computing the uncertainty dimension of the singularities, the uncertainty method effectively computes the box-counting dimension of the set of all discontinuities. The time delay is discontinuous on the (1-dimensional) frontiers of all C_n (see Fig. B.1), what implies that the result will be always greater than or equal to 1. The same happens with scattering functions.

Finally, we remark that methods to directly estimate the Hausdorff dimension of *attractor* sets (taking into account the infimum in (B.1)) was already discussed (see [5] and references therein). The main difficulty in adapting these methods to the case of *nonattracting* sets is that they require a sample of points on the set we want to measure. Even though a simple matter in the case of attractors, the computation of these points is nontrivial for nonattracting sets. A possibility would be the use of the PIM-triple procedure [3] to find trajectories which stay near the invariant set for arbitrarily long periods of time. The resulting methods are, however, far more complicated than those introduced here.

In summary, we have presented, through an example, methods to estimate the Hausdorff dimension of nonattracting invariant sets of scattering systems. The methods apply, albeit not only, to systems with invariant set dimension so small that the uncertainty methods do not work. It includes cases where the codimension of the future invariant set is approximately equal to or greater than one. We stress that these methods are general and can be used in phase spaces of any dimension. And since they allow, in principle, the computation of arbitrarily small dimensions, these techniques should be useful to study how chaotic scattering comes about as a system parameter is varied [6]. In particular, it may be interesting in investigations about routes to chaos in three dimensional scattering.

The authors thank Fapesp and CNPq for financial support.

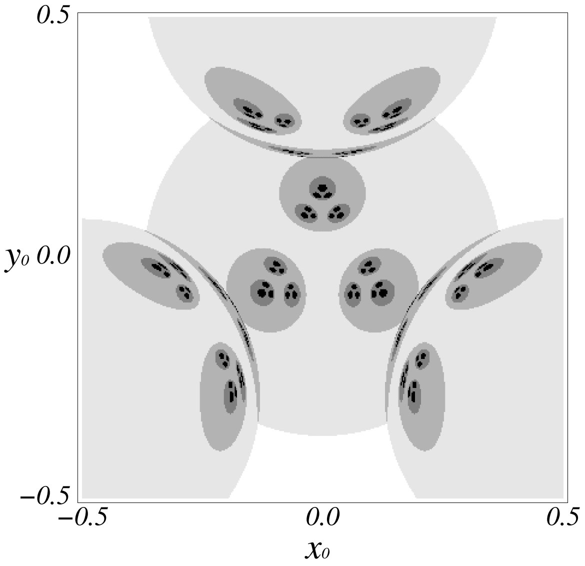

Figure B.1: C_n for $R = 0.37$: C_1 (light grey), C_2 (grey), C_3 (dark grey) and C_4 (black).

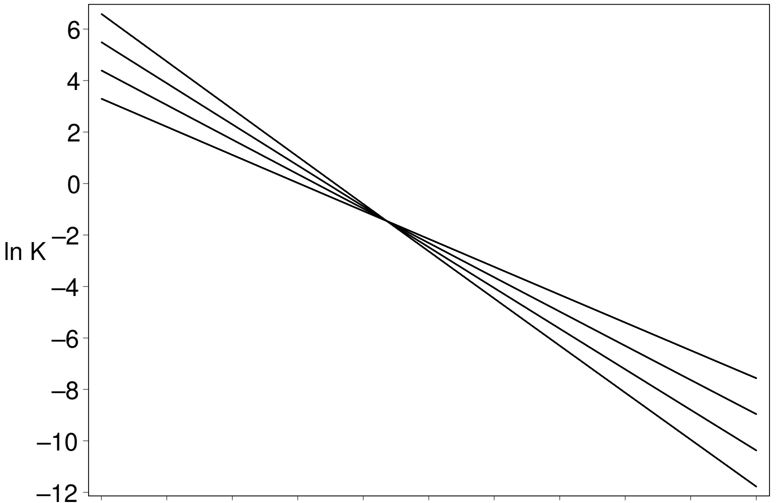

Figure B.2: $\ln K_n$ for $R = 0.37$: $n = 5$ (least inclined curve), $n = 6$, $n = 7$ and $n = 8$ (most inclined curve).

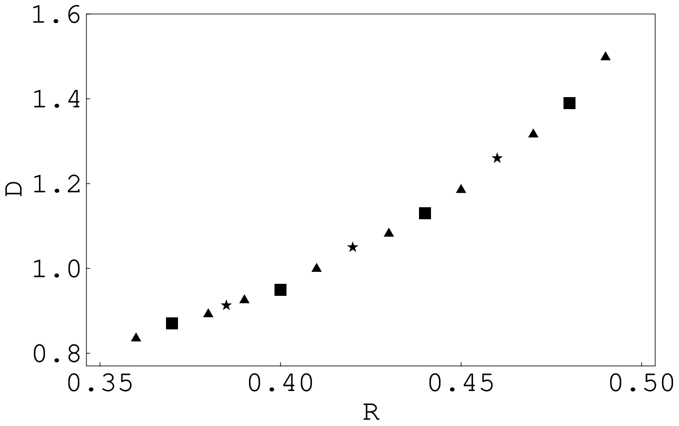

Figure B.3: Estimates of the dimension of $\cap_{m=1}^{\infty} C_m$ as a function of R: D_H (boxes), D_c (stars) and D_s (triangles). The size of the boxes, stars and triangles corresponds approximately to the statistical uncertainty of the dimension.

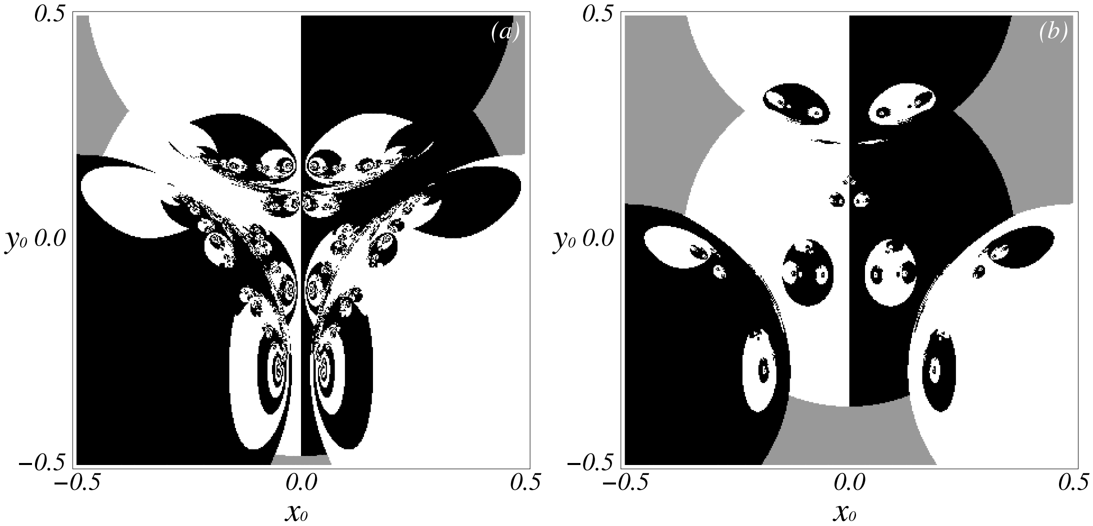

Figure B.4: Portrait of the basins of the tetrahedron scatterer for (a) $R = 0.48$ and (b) $R = 0.37$. The initial conditions were chosen on a grid of 400 × 400, on the plane P. Regions in black and white correspond to orbits that escape to $x \to +\infty$ and $x \to -\infty$, respectively. Regions in grey correspond to orbits not scattered.

Bibliography

[1] E. Ott, *Chaos in Dynamical Systems* (Cambridge University Press, Cambridge, 1994).

[2] Q. Chen, M. Ding, and E. Ott, Phys. Lett. A **145**, 93 (1990).

[3] H.E. Nusse and J.A. Yorke, Physica D **36**, 137 (1989).

[4] K. Sandau, Physica A **233**, 1 (1996).

[5] V.J. Martínez, R. Domínguez-Tenreiro, and L.J. Roy, Phys. Rev. E **47**, 735 (1993).

[6] S. Bleher, E. Ott, and C. Grebogi, Phys. Rev. Lett. **63**, 919 (1989).

C

Cusp-scaling behavior in fractal dimension of chaotic scattering

---

Adilson E. Motter, Ying-Cheng Lai, submetido à Physical Review E.

A topological bifurcation in chaotic scattering is characterized by a sudden change in the topology of the infinite set of unstable periodic orbits embedded in the underlying chaotic invariant set. We uncover a scaling law for the fractal dimension of the chaotic set for such a bifurcation. Our analysis and numerical computations in both two- and three-degrees-of-freedom systems suggest a striking feature associated with these subtle bifurcations: the dimension typically exhibits a sharp, cusp-like local minimum at the bifurcation.

PACS numbers: 05.45.-a, 05.45.Jn.

The development of nonlinear dynamics has led to new understanding of important physical processes, such as chaotic scattering [1, 2]. A scattering process is chaotic if it exhibits a sensitive dependence on initial conditions in the sense that, a small change in the input variables before the scattering can result in a large change in some output variables after the scattering. Apparently, in a scattering process, every physical trajectory is unbounded, but chaos arises because of a bounded chaotic set (chaotic saddle) in the scattering region where, for instance, the interaction between particles and potential occurs, as in a potential scattering system. Chaotic saddles are nonattracting and, dynamically, they lead to transient chaos [3]. Chaotic scattering is thus the physical manifestation of transient chaos in open Hamiltonian systems, which occurs in a variety of physical contexts [1].

An issue of fundamental importance in the study of chaotic scattering is to understand how the scattering dynamics changes characteristically as a system parameter is varied. There are three distinct classes of bifurcations in chaotic scattering: (1) routes to chaotic scattering from regular scattering, (2) metamorphic bifurcations in which the chaotic saddle suddenly changes its characteristics, and (3) topological bifurcations in which the topology of the chaotic saddle changes. Routes to chaotic scattering have been well documented, including abrupt bifurcations [4, 5] and saddle-center bifurcation followed by a cascade of period-doubling bifurcations [6]. There have also been efforts to study metamorphic bifurcations in chaotic scattering, such as crisis [7]. Topological bifurcations, characterized by topological changes in the subsets of infinite number of unstable periodic orbits (UPOs) embedded in the chaotic saddles, on the other hand, have not been well understood. One example of topological bifurcation is the massive bifurcation [8]. This type of bifurcations is *subtle* but it is expected to be important in high dimensions, as they can lead to distinct, physically observable scattering phenomena [9]. While there have been quantitative scaling results concerning both routes to chaotic scattering [4, 10] and metamorphic bifurcation [7], the understanding of topological bifurcations in chaotic scattering remains largely at the qualitative level [8], particularly in high dimensions [9].

In this Letter, we present a scaling law for the fractal dimension of the chaotic saddle in a topological bifurcation that appears to be typical in both two- [8] and three-degrees-of-freedom (DOF) [9] Hamiltonian systems. We focus on the fractal dimension because of its importance in shaping physically measurable quantities such as scattering functions, and because of the fact that most analytic scaling results associated with various routes to chaotic scattering concern fractal dimension but, to our knowledge, there has been none in the context of topological bifurcations. Because of the subtlety of a topological bifurcation, obtaining quantitative scaling laws, even numerically, is highly nontrivial. To be concrete, we state our main result in the context of potential scattering, with the particle energy E as the bifurcation parameter. Let E_c be the critical energy value at which a topological bifurcation occurs in the sense that, a class of infinite number of UPOs is destroyed and replaced by another one. The principal result of this Letter is then that, near the topological bifurcation, the fractal dimension of the set of singularities in any scattering function (to be described below) scales with the energy in the following way:

$$D - D_c \sim |E - E_c|^{D_c}, \tag{C.1}$$

where D_c is the dimension value at the bifurcation point. *The remarkable observation is that the dimension-versus-energy curve exhibits a cusp-like minimum at the bifurcation.* We establish (C.1) by a scaling argument, and we provide numerical verification using a class of 2-DOF scattering systems. We also argue that the scaling law should hold in 3-DOF systems. Our result is novel, as it represents the first, general, quantitative scaling result for topological bifurcation of chaotic scattering.

To derive the scaling law (C.1), we first consider 2-DOF potential scattering systems. Our idealized, albeit representative, scattering system consists of three potential hills in the plane, as shown in Fig. C.1. The heights E_1, E_2 and E_3 of hills 1, 2 and 3 satisfy $E_1, E_2 > E_3$. Assume that hill 3 has a circularly symmetric, quadratic maximum, and that it is close to the line connecting hills 1 and 2 so that the angle θ in the triangle formed by the centers of all three hills is greater than 90^o, as shown in Fig. C.1(a). When the particle energy E is slightly above E_3, a trapped particle can move back and forth between hills 1 and 2 following three different paths [6]: h, i, and j, as shown in Fig. C.1(a). When the energy drops below E_3, the path with greater deflection by crossing near the center of hill 3, path j, is destroyed because of the appearance of a new forbidden region around the center of hill 3, and is replaced by two new paths k, between hills 1 and 3 and between hills 2 and 3, as shown in Fig. C.1(b). For $E \approx E_3$, the UPOs that form the skeleton of the chaotic saddle are thus composed of sequences of paths h, i, j, and k. A topological bifurcation [8] occurs at $E_c = E_3$, at which the class of an infinite number of UPOs containing path j is destroyed and replaced by another class of infinite number of UPOs that contain paths k.

We focus on a fractal dimension that is physically most relevant: the dimension D of the set of singularities in a scattering function. Suppose that we launch particles toward the scatterer from a line outside the scattering region and measure a dynamical variable characterizing the outgoing particles after the scattering (*e.g.*, scattering angle), as a function of a variable characterizing the incoming particles before the scattering (*e.g.*, impact parameter). Due to chaos, such a scattering function typically contains an infinite number of singularities that constitute a fractal set, which is the set of intersecting points between the stable manifold of the chaotic saddle and the line [11]. Dynamically, the fractal set of singularities is constructed by successive interactions of the particles with the potential hills. For example, consider the interval s of the line corresponding to particles that are first deflected by hill 1, as shown in Fig. C.2. Three subintervals of this interval are then deflected by the other hills, with gaps between them corresponding to particles that are scattered to infinity right after the first interaction with hill 1. When $E > E_c$, these three subintervals are defined by particles that go from hill 1 to hill 2 along paths h, i, and j, respectively, as shown in Fig. C.2(a). When $E < E_c$, while two of the subintervals are still defined by particles that follow paths h and i, the third one is now determined by particles that go from hill 1 to hill 3 and *back* to hill 1, following path k, as shown in Fig. C.2(b). In the next step each one of the three surviving subintervals will split into three smaller subintervals, and so on. The splitting due to hill 3 is recorded at successive interactions with hills 1 and 2. This process defines a Cantor set with three linear scales corresponding to the factors by which the intervals are reduced in each step: $\alpha \approx s_h/s$, $\beta \approx s_i/s$, and $\gamma \approx s_j/s$ $(E > E_c)$ or $\gamma \approx s_k/s$ $(E < E_c)$, as shown in Fig. C.2.

To obtain the dimension D of the Cantor set, we employ the following scaling argument. Suppose that the critical energy E_c, the distance between the hills, and the effective radii of the hills at E_c are of order unity. Near the bifurcation, the deflection angle ϕ due to hill 3 of the particles corresponding to the edges of the intervals s_j and s_k, is smaller and greater than 90^o for $E \gtrsim E_c$ and $E \lesssim E_c$, respectively. In both cases, $|\tan\phi|$ is of order unity insofar as the angle θ is close neither to 90^o nor to 180^o so that $\tan(\pi - \theta) \sim \mathcal{O}(1)$ [see Figs. C.1 and C.2]. Thus, setting $|\tan\phi|$ to be of order unity provides an estimate of the width of the intervals s_j and s_k, and hence an estimate of γ. For concreteness, say the maximum of the potential hill 3 (the *bifurcation* hill) has the following quadratic form: $V = E_c[1-(r/a)^2]$. A straightforward calculation [12] indicates that, if $|\tan\phi| \sim \mathcal{O}(1)$, then the impact parameter b scales with the energy difference: $b \approx b_0|E - E_c| \equiv b_0\Delta$, where b_0 is proportional to $|\tan\phi|$. Therefore, the Cantor set is determined by the following scaling factors: α, β, and $\gamma \approx \gamma_0\Delta$, where α and β are constants, and γ_0 is constant on each side of the bifurcation. Under the approximation that there is a self-similarity in the fractal structure, the dimension D satisfies the following transcendental equation [4]: $\alpha^D + \beta^D + \gamma_0^D\Delta^D = 1$. For Δ and $\delta \equiv D - D(E_c)$ small, to the lowest order, this equation reduces to:

$$[\Delta^{D(E_c)}]^{\delta/D(E_c)} = C \times \frac{\delta/D(E_c)}{\Delta^{D(E_c)}}, \tag{C.2}$$

where C is a positive constant. An asymptotic analysis of Eq. (C.2) leads to [13] our main scaling result (C.1).

We now present numerical confirmation for the scaling law (C.1). To resolve the cusp structure implied by (C.1) is a highly nontrivial task. For numerical feasibility we thus consider a planar scattering system consisting of three non-overlapping potential hills located at the vertices (x_i, y_i) $(i = 1, 2, 3)$ of an isosceles triangle [6]. Each potential is represented by the following function: $V_i(x, y) = E_i[1 - (r_i/a_i)^2]$ for $r_i \leq a_i$, where $r_i = \sqrt{(x - x_i)^2 + (y - y_i)^2}$, and the potential is zero elsewhere. The Hamiltonian is thus: $H = |\mathbf{p}|^2/2m + V(x, y)$, where $\mathbf{p}$ is the two-dimensional momentum vector, and $V(x, y) = \sum_{i=1}^{3} V_i(x, y)$. The advantage of utilizing quadratic potential hills is that the motion of the particle inside each potential can be solved exactly, making a high-precision dimension calculation possible. In our numerical experiment, we choose the following set of parameter values: $E_1 = E_2 = 10$, $E_3 = 1$, $a_1 = a_2 = 2$, $a_3 = 1$, $(x_1, y_1) = -(x_2, y_2) = (4, 0)$, $(x_3, y_3) = (0, 2)$, and $m = 1$. A topological bifurcation thus occurs at $E_c = 1.0$. We utilize the uncertainty algorithm [14] to compute the dimension D of the set of singularities in scattering functions. For illustrative purpose, we choose the function to be the scattering angle to infinity $\psi \equiv \tan^{-1}(p_y/p_x)$ versus the location of the upward (initially) particle on the horizontal line at $y_0 = -4$. The result is shown in Fig. C.3, in which the cusp behavior is unequivocal [15]. Linear least-squares fits between $\ln[D(E) - D(E_c)]$ and $\ln|E - E_c|$ yield: $D(E) - D(E_c) = (0.093 \pm 0.005) \times (1 - E)^{0.29\pm0.03}$ for $E < E_c$ and $D(E) - D(E_c) = (0.19 \pm 0.01) \times (E - 1)^{0.31\pm0.03}$ for $E > E_c$, as shown by the inset in

Fig. C.3. The scaling exponents for both $E > E_c$ and $E < E_c$ agree well with the theoretically predicted one, the value of the dimension at E_c, which we obtain numerically: $D(E_c) = 0.314 \pm 0.005$. In addition, the proportional factor in (C.1) is greater for $E > E_c$ than for $E < E_c$, which is also expected because, theoretically, this factor is proportional to $\gamma_0^{D(E_c)}$ and γ_0 is greater in the former case. Overall, our computations lend strong credence to the validity of the scaling (C.1).

Our argument for the scaling law (C.1) can in fact be extended to chaotic scattering in 3-DOF Hamiltonian systems. As an example, we consider four potential hills but they now located in the three-dimensional physical space at the vertices of a tetrahedron, as schematically illustrated by planar projection of the hills in Fig. C.4(a) for $E > E_c$ and in Fig. C.4(b) for $E < E_c$. We focus on the dimension D of the intersecting set between the stable manifold of the chaotic saddle and a two-dimensional surface of the phase space, which is the dimension of the set of singularities in a scattering function on two variables. Arguments similar to those in the 2-DOF case can then be used to derive the scaling law (C.1) near a topological bifurcation, with the understanding that the dimension can in principle be either smaller or greater than one. When the radii of the potential hills are small, $D(E_c) < 1$ can arise, in which case $dD(E)/dE$ diverges at E_c and the dimension exhibits a cusp of the same nature as that in the 2-DOF case. If $D(E_c) > 1$, $dD(E)/dE$ goes continuously to zero as E goes to E_c, which implies that the dimension should be smooth.

Can this smooth behavior be expected for a topological bifurcation in 3-DOF scattering systems? To obtain an answer, we note the defining characteristic of a topological bifurcation: the topology of the UPOs is changed but from the standpoint of symbolic dynamics, no symbol is missing. In our 3-DOF case it means that, before the bifurcation, all UPOs corresponding to periodic sequences of the nine basic paths shown in Fig. C.4(a) must actually exist, while after the bifurcation, all those corresponding to sequences of the paths shown in Fig. C.4(b) exist. In particular the UPO represented by the sequence $\{h, j\}$ must exist when $E > E_c$. Without loss of generality, suppose that our 3-DOF system consists of three hard spheres of radius R at the vertices of a regular triangle with edge of unit length, and a smooth bifurcation hill located on the symmetrical axis perpendicular to the center of the triangle. In the inset of Fig. C.4(a) is shown the periodic orbit $\{h, j\}$ for $E > E_c$ in the limit $E \to E_c$. A necessary condition for the existence of this orbit, and hence for the occurrence of the topological bifurcation, is then $\zeta > 90^o$ [see Fig. C.4(a): the deflection angle due to hill 3 is smaller than 90^o when $E > E_c$]. In the three-dimensional physical space, however, there is an additional geometric constraint: $c > 1/2\sqrt{3}$, where c is the orthogonal distance from the center of the bifurcation hill to the lines connecting the hard spheres [Fig. C.4(a)]. We obtain numerically that the conditions $c > 1/2\sqrt{3}$ and $\zeta > 90^o$ are satisfied simultaneously only for $R < 0.39$. Numerical experiments indicate that, in this range of parameter values, $D(E_c)$ is smaller than one. It is reasonable to assume that the same is valid when the hard spheres are replaced by smooth potential hills. This implies that for a generic topological bifurcation in 3-DOF scattering systems, the cusp behavior in (C.1) is always expected [16].

In summary, our scaling analysis and numerical computations reveal a striking behavior in the fractal dimension associated with topological bifurcations in chaotic scattering: the dimension typically exhibits a cusp as a function of the bifurcation parameter, with a local minimum at the bifurcation.

A.E.M. is sponsored by FAPESP. Y.C.L. is supported by AFOSR under Grant No. F49620-98-1-0400 and by NSF under Grant No. PHY-9996454.

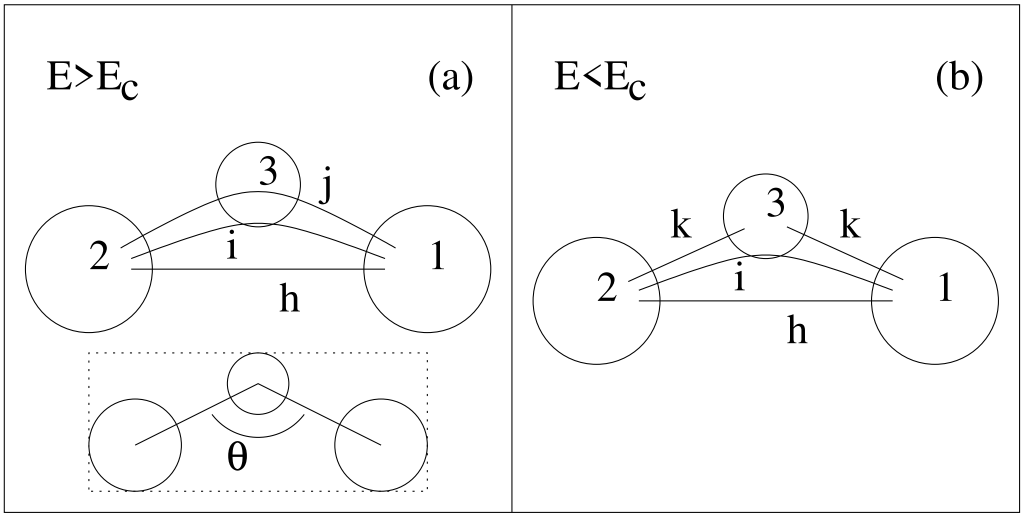

Figure C.1: A topological bifurcation in 2-DOF: basic paths composing UPOs (a) before and (b) after the bifurcation.

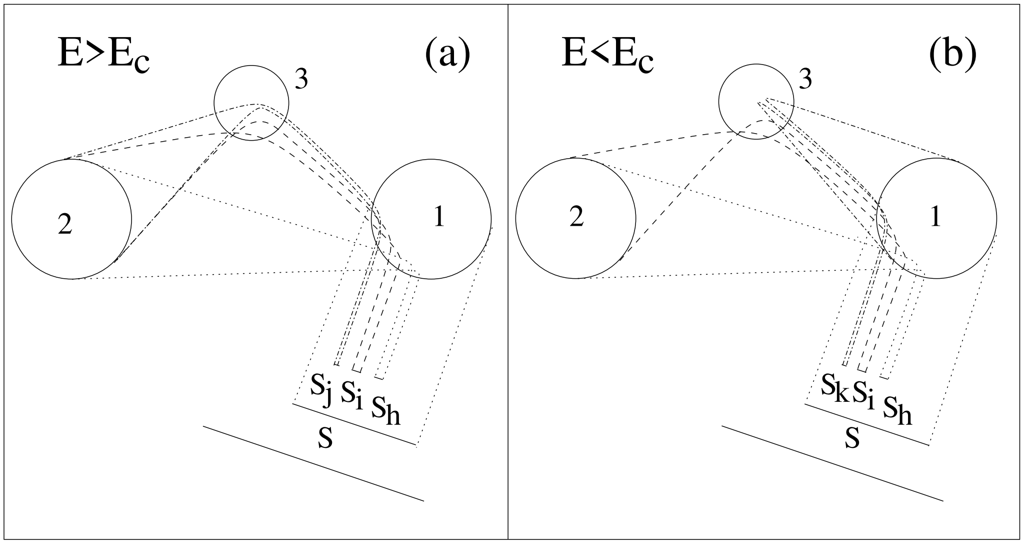

Figure C.2: Construction of the Cantor set.

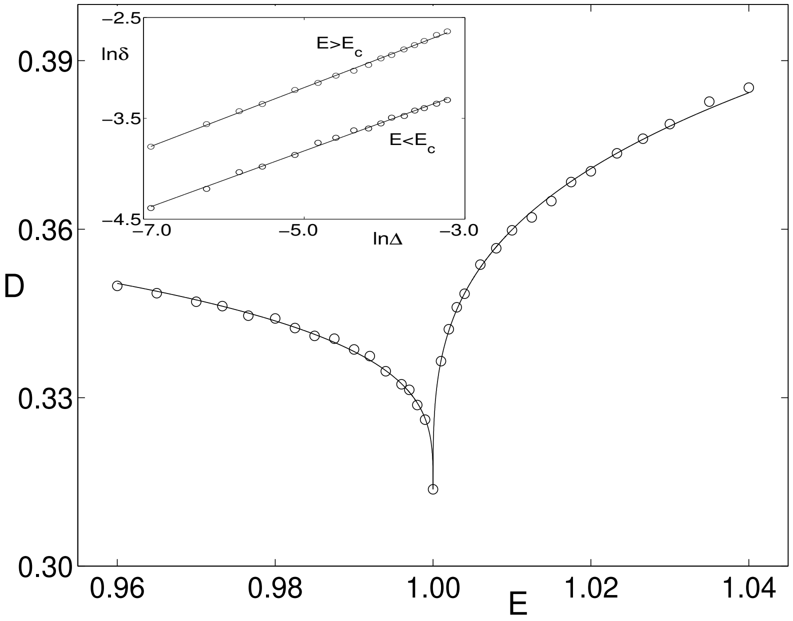

Figure C.3: Numerically obtained cusp scaling behavior in the fractal dimension about a topological bifurcation.

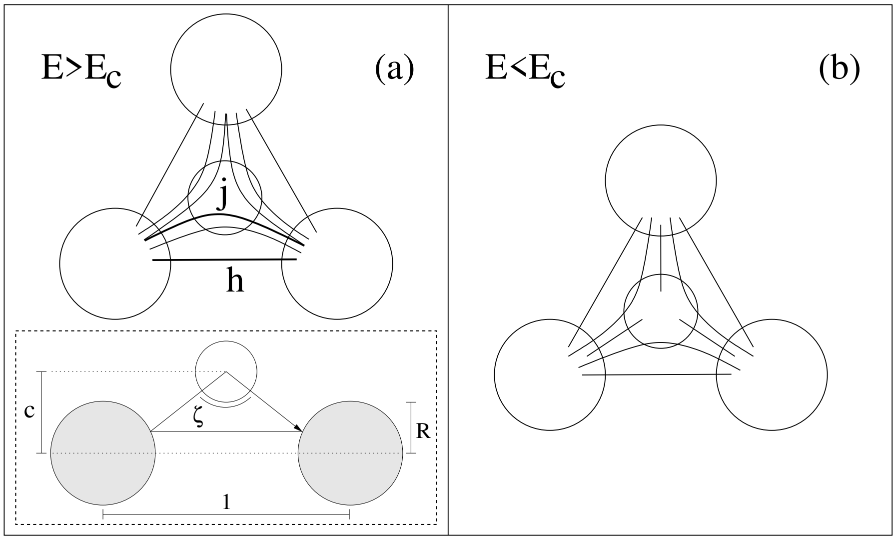

Figure C.4: A topological bifurcation in 3-DOF: basic paths (a) before and (b) after the bifurcation.

Bibliography

[1] Chaos Focus Issue **3** (4) (1993).

[2] P. Gaspard, *Chaotic Scattering and Statistical Mechanics* (Cambridge University Press, Cambridge, 1999).

[3] T. Tél, in: *Directions in Chaos*, edited by Bai-lin Hao (World Scientific, Singapore, 1990), Vol. 3.

[4] S. Bleher, C. Grebogi, and E. Ott, Physica D **46**, 87 (1990).

[5] Y.-C. Lai, Phys. Rev. E **60**, R6283 (1999).

[6] M. Ding, C. Grebogi, E. Ott, and J. A. Yorke, Phys. Rev. A **42**, 7025 (1990).

[7] Y.-C. Lai and C. Grebogi, Phys. Rev. E **49**, 3761 (1994).

[8] M. Ding, C. Grebogi, E. Ott, and J. A. Yorke, Phys. Lett. A **153**, 21 (1991); M. Ding, Phys. Rev. A **46**, 6247 (1992).

[9] A. E. Motter and P. S. Letelier, Phys. Lett. A **277**, 18 (2000); Y.-C. Lai, A. P. S. de Moura, and C. Grebogi, Phys. Rev. E **62**, 6421 (2000).

[10] T. Tél, Phys. Rev. A **44**, 1034 (1991).

[11] The dimension D is related to d, the dimension of the chaotic saddle, as: $d = 1 + 2D$.

[12] The deflection angle ϕ due to a potential of the form $V = E_c[1 - (r/a)^2]$ satisfies $\tan\phi = [b/a]/[\sqrt{(E - E_c)/E_c + (r_0/a)^2} - \sqrt{(r_0/a)^2 - (b/a)^2}]$, where b is the impact parameter and r_0 is the initial distance to the center of the hill. For $|E - E_c|/E_c \ll (r_0/a)^2$ and $b \ll r_0$ it reads: $\tan\phi \approx [2br_0/a^2]/[(E - E_c)/E_c + (b/a)^2]$. Therefore, $|\tan\phi| \sim \mathcal{O}(1)$ implies $b \approx b_0|E - E_c|$, where $b_0 = a^2|\tan\phi|/2r_0E_c$.

[13] Equation (C.2) has the following form: $x^{f(x)} = Cf(x)/x$, where $x = \Delta^{D(E_c)}$ and $f(x) = \delta/D(E_c)$. For $\lim_{x\to 0} f(x) \to 0$, the asymptotic solution is $x^{f(x)} \to G$, where G is a constant. Clearly G cannot be zero because if it were, then x goes to zero much faster than $f(x)$ does and, $f(x)/x \to \infty$, which is inconsistent with the original equation. In fact, the consistence with Eq. (C.2) implies $G = 1$, from which follows $f(x) = x/C$ and hence (C.1).

[14] S. W. McDonald, C. Grebogi, E. Ott, and J. A. Yorke, Physica D **17**, 125 (1985); A. P. S. de Moura and C. Grebogi, Phys. Rev. Lett. **86**, 2778 (2001).

[15] To obtain Fig. C.3, about 100 hours of CPU time is required on a supercomputer consisting of 17 AMD 1.2GHz CPUs.

[16] The scaling relation (C.1) is derived for nondegenerate hills. An instructive counterexample can be constructed as follows. Take the planar scattering system in Fig. C.1 and revolve it about the y-axis, which yields a 3-DOF system. The value of the dimension D is increased by 1, leading to the following scaling relation: $D - D(E_c) \sim |E - E_c|^{D(E_c)-1}$. The remarkable feature is that, despite $D(E_c) > 1$, the cusp at E_c is still present.

D

Dissipative chaotic scattering

Adilson E. Motter, Ying-Cheng Lai, Physical Review E **65**, 015205 (Rap. Commun.) (2002).

We show that weak dissipation, typical in realistic situations, can have a metamorphic consequence on nonhyperbolic chaotic scattering in the sense that the physically important particle-decay law is altered, no matter how small the amount of dissipation. As a result, the previous conclusion about the unity of the fractal dimension of the set of singularities in scattering functions, a major claim about nonhyperbolic chaotic scattering, may not be observable.

PACS numbers: 05.45.-a, 05.45.Df.

Chaotic scattering [1, 2, 3] is a physical manifestation of transient chaos [4], which is due to the existence of nonattracting chaotic invariant sets, i.e., chaotic saddles, in the phase space. As a result, a Cantor set of singularities arises in physically measurable scattering functions relating an output variable after the scattering to an input variable before the scattering [2]. Generally, the dynamics of chaotic scattering may be characterized as either *hyperbolic* or *nonhyperbolic*. In hyperbolic chaotic scattering, all the periodic orbits are unstable and there are no Kol'mogorov-Arnol'd-Moser (KAM) tori in the phase space and, as such, the survival probability of a particle in the scattering region typically decays exponentially with time. In nonhyperbolic chaotic scattering [5, 6], there are both KAM tori and chaotic sets in the phase space. Due to the stickiness effect of KAM tori, a particle initialized in the chaotic region can spend a long time in the vicinity of KAM tori, leading to an algebraic decay [7] of the survival probability of the particle in the scattering region.

A surprising result in nonhyperbolic chaotic scattering is that, because of the algebraic decay, the fractal dimension of the set of singularities in a scattering function is unity [6].

A physically important issue in the study of nonlinear dynamics is to understand how robust a phenomenon is against perturbations or deviations between the underlying mathematical model and physical reality. In the case of chaotic scattering, most of the theoretical investigations so far have been restricted to Hamiltonian or conservative systems. In a realistic situation, a small amount of dissipation can be expected. Take, for example, chaotic scattering arising in the context of particle advection in hydrodynamical flows [8]. In most existing studies, the condition of incompressibility is assumed of the underlying flow [8], which allows the problem to be casted in the context of Hamiltonian dynamics as the particle velocities can be related to flow's stream function in a way that is completely analogous to the Hamilton's equations in classical mechanics. Real hydrodynamical flows cannot be perfectly incompressible, and the effects of inertia and finite mass of the particles advected by the flow are effectively those due to friction, or dissipation [9].

The aim of this paper is to study the effect of dissipation on chaotic scattering dynamics. We first consider hyperbolic chaotic scattering and argue that weak dissipations have a negligible effect on the physical observables of chaotic scattering, such as scattering functions. We then focus on nonhyperbolic chaotic scattering and find that, in contrast to the hyperbolic case, the scattering dynamics can be altered by weak dissipation in a fundamental way. The major consequence of dissipation is that it typically converts KAM tori into periodic attractors. As a result, the underlying chaotic saddle can undergo a metamorphic bifurcation to a structurally different chaotic set, playing the role of chaotic invariant set that generates fractal basin boundaries [10]. There is an immediate transformation of the decay law of scattering particle from being algebraic in the Hamiltonian case to being exponential in the dissipative case, no matter how small the amount of dissipation. As a result, the fractal dimension of the chaotic saddle decreases from the integer value in the Hamiltonian case. These findings have striking implications to the study of chaotic scattering: they suggest that the algebraic-decay law, regarded to hold universally in nonhyperbolic chaotic scattering, is apparently structurally unstable against weak dissipations. More importantly, the previously believed integer dimensions of the chaotic saddles [6] in nonhyperbolic chaotic scattering may not be observable in realistic physical situations where dissipation is present.

We begin by presenting a picture for the formation of the fractal sets in chaotic scattering. Consider the idealized model of the hierarchical construction of Cantor sets in the unit interval. For hyperbolic scattering, an open subinterval in the middle of the unit interval is removed first. From each one of the two remaining subintervals, the same fraction from their middle is removed, and so on. Each step of this construction can be thought of as an iteration of the hyperbolic tent map with slope larger then two. The total length that remains decays exponentially with the number of iterations and the resulting Cantor set has a fractal dimension (e.g., box-counting dimension) smaller than one. For nonhyperbolic chaotic scattering, the same construction applies but the fraction removed at each step decreases with time, say, is inversely proportional to time. This simple reduction of the fraction removed captures the essence of the effect of KAM tori: their “stickiness” to particle trajectories in the phase space [6]. The remaining length decays algebraically with time and, even though the measure of the remaining set asymptotes to zero, the resulting Cantor set has dimension one [6].

How does dissipation change the above construction? The skeleton of the underlying chaotic saddle is formed by periodic orbits. When the system is hyperbolic, its structural stability guarantees the survival of all periodic orbits under small changes of the system parameters. Accordingly, the structure of the Cantor set in the presence of a small amount of dissipation is expected to be the same as before. When the dynamics is nonhyperbolic, however, qualitatively different behavior can take place. Marginally stable periodic orbits in KAM islands can become stable, turning their nearby phase-space regions into the corresponding basins of attraction [11]. This means that, part of the previous chaotic saddle now becomes part of the basins of the attractors. Most importantly for the scattering dynamics, the converted subset supports orbits in the neighborhood of the KAM islands that otherwise would be scattered after a long, algebraic time. These orbits are solely responsible for the nonhyperbolic character of the scattering in the conservative case. Due to the existence of dense orbits in the original chaotic saddle, the noncaptured part of the invariant set remains in the boundaries of basins of the periodic attractors. Therefore, the invariant set is the asymptotic limit of the boundaries between scattered and *captured* orbits, rather than those between scattered and *scattered* orbits as in the conservative case. Chaos thus occurs on the nonattracting invariant set whose stable manifold becomes the boundary separating the basins of the attractors and of the scattering trajectories. Through this simple reasoning we can see that the structure and the meaning of the Cantor set is fundamentally altered: in successive steps we remove a *constant* instead of a decreasing fraction in the middle of each interval. As a result, the scattering dynamics becomes hyperbolic with exponential decay. The dimension of the Cantor set immediately decreases from unity as a dissipation parameter is turned on. There is now more than one possible outcome: some of the removed intervals correspond to scattered orbits and the others correspond to orbits captured by the attractors. We stress that the appearance of attractors accompanied by a metamorphosis of the chaotic saddle can occur for arbitrarily small dissipation.

We now present numerical support for the effect of weak dissipation on chaotic scattering, particularly the metamorphic transformation of particle decay and fractal dimension in the nonhyperbolic case. Our model is a dissipative version of the two-dimensional area-preserving map utilized in Ref. [6] to establish the unity of the fractal dimension, a particularly convenient model for studying nonhyperbolic chaotic scattering. The map reads

$$M\begin{pmatrix} x \\ y \end{pmatrix} = \begin{cases} \lambda[x-(x+y)^2/4-\nu(x+y)] \\ \lambda^{-1}[y+(x+y)^2/4] \end{cases}, \tag{D.1}$$

where $\lambda > 1$ and $\nu \geq 0$ are parameters. The map is conservative for $\nu = 0$ and dissipative for $\nu > 0$. For $\nu = 0$, almost all orbits started from negative values of y are scattered to infinity. In this case, the dynamics is nonhyperbolic for $\lambda \lesssim 6.5$ and hyperbolic for $\lambda \gtrsim 6.5$. The computation of the particle decay and fractal dimension in nonhyperbolic scattering requires examining very small scales, which makes the numerical computation a highly nontrivial task [5]. The advantage of using map (D.1) instead of a continuous flow is that it makes high-precision computation possible. Our results are, however, expected to hold in typical nonhyperbolic systems with KAM tori.

We study map (D.1) in the nonhyperbolic regime, without and with dissipation. We set $\lambda = 4.0$. When there is no dissipation ($\nu = 0$), there is a major KAM island in the phase space, as shown in Fig. D.1(a). The fractal boundaries of the basins of scattering trajectories to infinity are also shown, which correspond to the stable manifold of the chaotic saddle in the scattering region. When dissipation is present ($\nu > 0$), the fixed point in the center of the island becomes an attractor. Dynamically, it happens because the magnitudes of the eigenvalues of periodic orbits associated with islands are one, which are reduced by dissipation in general. The basin of attraction of this attractor "captures" the island itself and orbits close to the stable manifold of the previously existing invariant set, as shown in Fig. D.1(b). The intricate character of the basin of attraction with apparent fractal boundaries comes from points of the invariant set that are arbitrarily close to the island for $\nu = 0$. The newly created basin of attraction contains these points and hence, all their preimages as well. These preimages extend in the phase space along the original stable manifold of the chaotic saddle, which is the reason that the boundaries mimic those of the original basins of scattering trajectories [Figs. D.1(a) versus D.1(b)]. Because of this similarity, the scattering functions and time-delay functions, which are physically measurable, *resemble* each other in both the conservative and weakly dissipative case, as shown, respectively, in Figs. D.1(c) and D.1(d), where the time delay of particles launched from the horizontal line $y = -2$ toward the scattering region is plotted against their x-coordinates on the line.

To examine the decay laws of the scattering particles, we approximate the survival probability of a particle in the scattering region by $R(n)$, the fraction of a large number of particles still remaining in the scattering region (defined by $\sqrt{x^2 + y^2} < r$) at time n, which are initiated in subregions close to the boundaries of the scattering basins. For convenience, we choose $r = 100$ and choose initial conditions from the horizontal line at $y_0 = -2$. When the dynamics is nonhyperbolic and conservative, the decay of $R(n)$ with time is exponential for small n and algebraic for large n, as shown in Fig. D.2(a) for

$\lambda = 4.0$: $R \sim e^{-\alpha n}$ for $n \lesssim 250$ and $R \sim n^{-\beta}$ for $n \gtrsim 250$, where $\alpha \cong 0.08$ and $\beta \cong 1.0$. In the presence of a small dissipation, the time decay becomes strictly exponential and with the same decay rate of the exponential regime of the conservative case, $\alpha \cong 0.08$, as shown in Fig. D.2(b) for $\nu = 0.001$. The original algebraic decay in the conservative case is destroyed by the dissipation because orbits with points close to the island, and that otherwise would be stuck, are captured by the periodic attractor. The decay rate in general changes under further increases of the dissipation. For $\nu = 0.01$, for instance, we obtain $\alpha \cong 0.06$. In the hyperbolic region the time decay is always exponential. For $\lambda = 8.0$, for example, the decay rate α remains essentially constant and equal to 0.9 in the range $0 \leq \nu \leq 0.01$.

The uncertainty algorithm [10] can be used to compute the fractal dimension D of the set of intersection points between the stable manifold of the chaotic saddle and a line from which scattering particles are initiated. As above, we choose the line $y_0 = -2$. In the absence of attractors, D is the dimension of the set of singularities in scattering functions. In Ref. [6], it is argued that $D = 1$ when map (D.1) is nonhyperbolic and conservative. A technical point about the numerical evaluation of the dimension in this case is that the result converges *slowly* to unity, and the convergence rate is determined by the reduction of length scales in the computation [6]. When a small amount of dissipation is present, $D + 1$ becomes the dimension of the boundaries between scattered and captured basins. The numerical convergence of D is in this case *faster* and essentially independent of the size of the interval under consideration. For $\lambda = 4.0$ and $\nu = 0.01$, we obtain $D \cong 0.8$, a well-convergent value as the length scale is reduced over six orders of magnitude. The dimension is much less sensitive to the presence of dissipation if the dynamics is hyperbolic. For $\lambda = 8.0$, for instance, we obtain $D \cong 0.44$ for both $\nu = 0$ and 0.01.

Dissipation can also lead to several coexisting attractors for some values of λ in the originally nonhyperbolic region. Periodic attractors are created through saddle-node bifurcations as λ is varied. These attractors then undergo period doubling cascades until the accumulation point where chaos appears. For small dissipation, however, the chaotic interval in the parameter space can be so small that it is difficult to detect chaotic attractors numerically. In fact, for ν on the order of 0.01 or smaller, the dynamics of map (D.1) is dominated by low-period periodic attractors. Periodic attractors of high periods either have small basins of attraction or exist in small intervals in the parameter space. Since periodic attractors result from the stabilization of periodic orbits in KAM islands, the parameter regions in which these attractors exist are approximately the same as those of the corresponding islands. In addition, the sizes of the basins are of the same order of the sizes of the original islands in the phase space [12].

In summary, our qualitative and quantitative examinations indicate that weak dissipation, no matter how small, can fundamentally alter the nature and dynamics of nonhyperbolic chaotic scattering. The algebraic-decay law, commonly believed to hold in such a case, is typically converted into an exponential-decay law in the metamorphic sense that the conversion can be induced by arbitrarily small amount of dissipation. A consequence of such a metamorphosis is that the previously claimed [6] unity of the fractal dimension of the set of singularities in scattering functions may not be physically meaningful. To our knowledge, there has been no previous attempt to address the effect of dissipation in open Hamiltonian systems, but this is a physically important issue of nonlinear dynamics that deserves further attention.

This work was supported by AFOSR under Grant No. F49620-98-1-0400. A.E.M. acknowledges financial support from FAPESP.

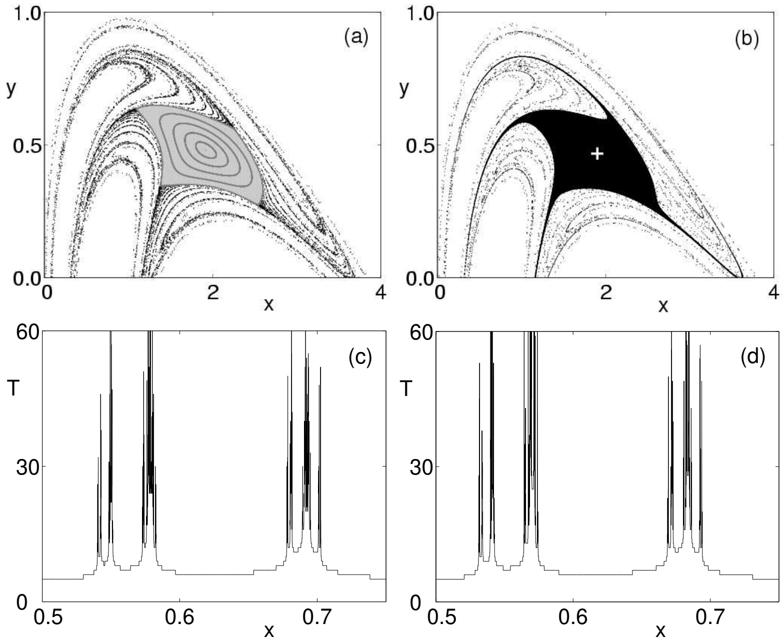

Figure D.1: Phase-space structure and time-delay function for map (D.1) with $\lambda = 4.0$. (a) $\nu = 0$: KAM island (in grey), scattered orbits (in blank), and the fractal boundaries of the scattered orbits (in black). (b) $\nu = 0.01$: captured orbits (in black) and scattered orbits (in blank). The plus sign is the fixed point attractor. (c),(d) Time delay in the conservative and dissipative cases of (a) and (b), respectively. T is the time taken by particles to reach $\sqrt{x^2+y^2} \geq 100$.

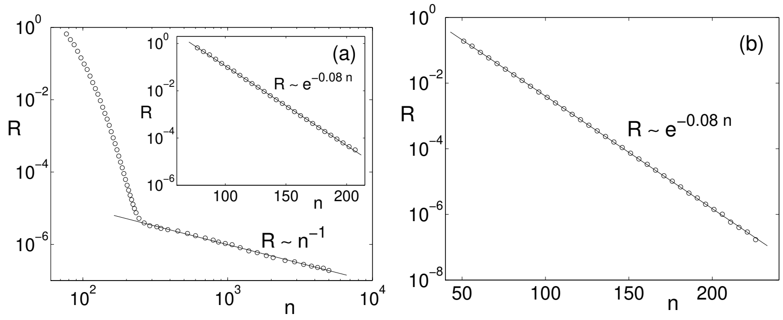

Figure D.2: Time decay for map (D.1) with $\lambda = 4.0$, in the interval $[x_0, x_0 + 10^{-7}]$. (a) $\nu = 0$, $x_0 = 0.5770050$. The inset corresponds to the initially exponential decay. (b) $\nu = 0.001$, $x_0 = 0.5760006$.

Bibliography

[1] Some representative early papers on chaotic scattering are C. Jung, J. Phys. A **19**, 1345 (1986); M. Hénon, Physica D **33**, 132 (1988); P. Gaspard and S. A. Rice, J. Chem. Phys. **90**, 2225 (1989); G. Troll and U. Smilansky, Physica D **35**, 34 (1989).

[2] For a relatively early review of chaotic scattering, see Chaos Focus Issue **3**(4) (1993).

[3] P. Gaspard, *Chaos, Scattering, and Statistical Mechanics* (Cambridge University Press, Cambridge, 1998).

[4] C. Grebogi, E. Ott, and J. A. Yorke, Physica D **7**, 181 (1983).

[5] M. Ding, C. Grebogi, E. Ott, and J. A. Yorke, Phys. Rev. A **42**, 7025 (1990); Y.-C. Lai, R. Blümel, E. Ott, and C. Grebogi, Phys. Rev. Lett. **68**, 3491 (1992).

[6] Y. T. Lau, J. M. Finn, and E. Ott, Phys. Rev. Lett. **66**, 978 (1991).

[7] C. F. F. Karney, Physica D **8**, 360 (1983); B. V. Chirikov and D. L. Shepelyansky, Physica D **13**, 394 (1984); J. Meiss and E. Ott, Physica D **20**, 387 (1986); Y.-C. Lai, M. Ding, C. Grebogi, and R. Blümel, Phys. Rev. A **46**, 4661 (1992).

[8] See, for example, B. Eckhardt and H. Aref, Philos. Trans. R. Soc. London, Ser. A **326**, 655 (1988); Á. Péntek, Z. Toroczkai, T. Tél, C. Grebogi, and J. A. Yorke, Phys. Rev. E **51**, 4076 (1995); G. Stolovitzky, T. J. Kaper, and L. Sirovich, Chaos **5**, 671 (1995).

[9] M. R. Maxey and J. J. Riley, Phys. Fluids **26**, 883 (1983).

[10] See, for example, S. W. McDonald, C. Grebogi, E. Ott, and J. A. Yorke, Physica D **17**, 125 (1985).

[11] The phenomenon of stabilization of periodic orbits induced by dissipation was previously reported in the context of multistability and complexity of *closed* systems, U. Feudel and C. Grebogi, Chaos **7**, 597 (1997).

[12] Small additive noise, another perturbation likely to appear in physical processes, does not destroy the attractors, at least for time scales achievable in numerical simulations. In the presence of uniform noise, periodic attractors become extended stochastic attractors and the fine structures of the basin boundary become smeared. Increases in the noise amplitude eventually lead to the escape of the attracted orbits after a transient period of time near the destroyed attractors.

E

Arbitrariness in defining fractal basins: Relations between open and closed systems

---

Adilson E. Motter, Patricio S. Letelier, Regular and Chaotic Dynamics **6**, 215 (2001).

A discussion about dependences of the (fractal) basin boundary dimension with the definition of the basins and the *size* of the exits is presented for systems with one or more exits. In particular, it is shown that the dimension is largely independent of the choice of the basins, and decreases with the size of the exits. Considering the limit of small exits, a strong relation between fractals in exit systems and chaos in closed systems is found. The discussion is illustrated by simple examples of one-dimensional maps.

Mathematics Subject Classification 28A80.

E.1 Introduction

Fractals have been largely applied to characterize the dynamics of systems with multiple modes of exit [1]. For instance, in the capture of orbits by attractors [2], in the scattering of particles by located [3] and by nonlocated potentials [4], and in the initial-condition sensitivities caused by chaotic transients [5]. In this context, fractal sets are: Boundaries among basins of initial conditions going out via different exits, singularities of scattering functions, or singularities of exit-time functions.

An exit system has in general either one of the two following kinds of behavior: a) The system is stable, which is the open counterpart of nonchaotic closed systems, or b) the system presents some sensitive dependence on initial conditions, the open analogous of chaotic closed systems. The behavior exhibited by the system is determined by the nature of the nonattracting invariant set of trapped orbits. More precisely, it is through the dimension of the future invariant set that the sensitivity of the system is quantified [1]. This dimension can go from zero (no instabilities) to the energy surface dimension (maximal sensitivity), relating the cause of the sensitivity (invariant sets) with the phenomenon itself (fractal structures in basin boundaries, exit-times, etc).

The aim of this paper is to discuss relations between different fractal sets, the dependence of the dimension of the basin boundaries with the definition of the basins (equivalently, the definition of the exits), and the dynamical consequences of fractals in closed (nonexit) systems. Among the motivations of this work are the so far unanswered questions: (1) How arbitrary can be the definition of the basins? A basin boundary gives information about the system when its dimension reveals the dimension of the future invariant set. Since the future invariant set and the basin boundary are in general nonidentical sets, conditions on the definition of the exits that ensure the equality of the dimensions have to be found. (2) How to study a system whose orbits "choose" the exits only after the time evolution of the initial conditions by arbitrarily large periods of time? As an example consider the orbits of light traveling around a periodically perturbed black hole [6]. By physical considerations, almost all orbits starting on a Poincaré section are (eventually) captured by the black hole or scattered to infinity. Suppose that we are interested in measuring the sensitivity of the system for these two exits by computing the dimension of the invariant orbits on the Poincaré section. For some initial conditions, the trajectory integrated on a finite period of time goes unequivocally to the black hole. Other orbits, however, remain around the black hole for a long time and it is in general difficult to determine whether the final state will be at the black hole or at infinity. This problem is a consequence of our inability in integrating the system for an infinite interval of time. (3) What sort of relation communicates fractals in exit systems with chaos in nonexit systems? Fractal structures and chaos present a number of analogous implications. For instance, both chaos and fractals prevent integrability. Accordingly, it is worth looking for a common mechanism determining fractals in open systems and chaos in closed systems.

In order to answer these questions we restrict the discussion to a class of autonomous systems for which almost all orbits of interest eventually exit, and the exits are defined regions of the phase space. For these systems, we shall consider each N-dimensional manifestly invariant part of the phase space (e.g., each energy surface), where N is refered as the effective phase space dimension.

In Section E.2 we observe that the basin boundary dimension is largely independent of the choices of the basins if the *total* exit is fixed. In this context we also discuss relations between the dimensions of different fractal sets for different concepts of dimension. The dimension decreases, however, when the total exit is enlarged. The enlargement of the exits as a technique to study systems whose capture of orbits by the exits takes arbitrarily long time is considered in Section E.3. The limit of small exits, on the other hand, reveals the chaotic or regular character of the corresponding closed system. The main result of this communication concerns the relations between fractals in exit systems and chaos in the associated nonexit systems studied in Section E.4. Finally, our conclusions are presented in the last section. The discussion is accompanied by explicit examples of one-dimensional maps. Non standard definitions used along the text are summarized in the appendix.

E.2 Invariances of fractal dimensions

Let us consider the map [1]

$$x_{n+1} = \begin{cases} 2\eta x_n, & \text{if } x_n \leq 1/2, \\ 2\eta(x_n - 1) + 1, & \text{if } x_n > 1/2, \end{cases} \tag{E.1}$$

where η is a positive parameter ($\eta > 1$ in this section). In spite of its noninversible and discontinuous character, this map can be seen as a canonical model for hyperbolic scattering systems. The noninversibility is a consequence of the reduced dimension of the model. The discontinuity would be avoided by employing a tend-like map or a logistic-like map, which is also smooth, with no relevant changes. We prefer this map, however, because of its simpler symbolic dynamics.

For a uniform distribution of initial conditions in $[0, 1]$, the decay rate with the number

n of iterations is η^{-n}. A half of the points goes to $x > 1$ and then asymptotically to $+\infty$, and the other half goes to $x < 0$ and then to $-\infty$. In Fig. E.1 we show in two different colors the basins associated to $+\infty$ and $-\infty$ as a function of η. In this figure we see the complex structure of the basin boundary (also present in any magnification), a feature of systems with sensitive dependence on initial conditions. The box-counting dimension of the basin boundary numerically estimated by a method presented in Ref. [1] is fitted by $D_c = \ln 2/\ln 2\eta$. On the other hand, since the points that go out in one iteration are those of the interval $(1/2\eta, 1 - 1/2\eta)$, we can reinterpret the total exit as being this interval. In Fig. E.2 we show the exit-time function for $\eta = 3/2$. In computing the uncertainty dimension of the singularities of the exit-time functions by the method of [7] we also obtain a curve fitted by $D_u = \ln 2/\ln 2\eta$.

The coincidence of the above fractal dimensions is due to the presence of an invariant bounded set (the future invariant set) with box-counting dimension $D_c = \ln 2/\ln 2\eta$, which is chaotic since the Lyapunov exponent $h = \ln 2\eta$ is positive. The box-counting dimension is defined by [1]

$$D_c = \lim_{\varepsilon \to 0} \frac{\ln N(\varepsilon)}{\ln 1/\varepsilon}, \tag{E.2}$$

where N is the number of ε-interval needed to cover the set. The invariant set is a Cantor set of Lebesgue measure zero obtained as follows. Remove the $1 - 1/\eta$ open interval in the middle of $[0, 1]$. From each one of the two remaining intervals remove the same fraction in their middle, and so on.

In terms of Fig. E.1, the invariant points correspond to the nonisolated points of the basin boundary for each η. A countable set of isolated points, like $x = 1/2$, are in the basin boundary but are not invariant. This set, refered here as the *intrinsic frontier*, is a consequence of the definition of the basins and, in this case, do not affect the dimension of the boundary. (The intrinsic frontier is completely avoided by coloring in black and white the points that leave $[0, 1]$ in even and odd number of iterations, respectively - see Fig. E.3.) Moreover, the basin boundary dimension remains invariant if we redefine the exits as $(1/2\eta, \lambda]$ and $(\lambda, 1 - 1/2\eta)$ for $1/2\eta < \lambda < 1 - 1/2\eta$ (Fig. E.1 corresponds to the choice $\lambda = 1/2$). In Fig. E.4 we show the basin boundary as a function of λ for $\eta = 3/2$. In spite of the morphological changes in the basins, the variation of λ just dislocates the intrinsic frontier so that the basin boundary dimension is still the dimension of the invariant set.

Let us put the above discussion in a more general context, where we consider two exits E_1 and E_2 so that $E_1 \cap E_2 = \emptyset$, $E_1 \cup E_2 = (1/2\eta, 1 - 1/2\eta)$, $\mu(E_1) \neq 0$ and $\mu(E_2) \neq 0$ (μ denotes the Lebesgue measure). The question we address is: How arbitrary can be the choices (definitions) of the exits E_1 and E_2 ? We denote by L the set of extremes of the intervals that appear in the construction of the Cantor set, by I_0 the remaining invariant set, by I the (total) invariant set[1] $L \cup I_0$, by F_1 the set of points of the intrinsic frontier in $(1/2\eta, 1 - 1/2\eta)$ (that go out in the first iteration), by F_i points of the intrinsic frontier that go out in the i^{th} iteration, by F the (total) intrinsic frontier $\cup_{i=1}^{\infty} F_i$, and by B the (total) basin boundary $F \cup I$.

Taking the Hausdorff dimension (see [1] for the definition),

$$\begin{aligned} D_H(B) &= \max\{D_H(F), D_H(I_0), D_H(L)\} \\ &= \max\{D_H(F_1), D_H(I_0)\}, \end{aligned} \tag{E.3}$$

where we used $D_H(L) = 0$ since L is a countable set, and $D_H(F) = D_H(F_1)$ because F is a countable union of similar copies of F_1 [8]. Therefore, the dimension of the basin boundary is equal to the dimension of the restricted invariant set if and only if $D_H(F_1) \leq D_H(I_0)$. When this inequality is not satisfied, the basin boundary dimension is just an effect of the definitions of the exits. In the sense of Hausdorff dimension, are good exits those ones for which $D_H(F_1) = 0$. It includes all F_1 countable, as in the case of E_1 and E_2 defined as finite unions of intervals.

Alas, in general we cannot measure D_H but D_c, where by definition $D_c(A) \geq D_H(A)$ for any set A [1]. Considering the box-counting dimension:

$$D_c(B) = \max\{D_c(F), D_c(I_0), D_c(L)\}. \tag{E.4}$$

---

[1] We call I_0 the *restricted* invariant set. The distinction between I_0 and I is in order to show that there is no relevant differences between an open total exit $(1/2\eta, 1 - 1/2\eta)$ with invariant set I and a closed total exit $[1/2\eta, 1 - 1/2\eta]$ with invariant set I_0.

From (E.2) we can show that $D_c(L) = D_c(I_0)$ and $D_c(F) = \max\{D_c(F_1), D_c(I_0)\}$. If F_1 is finite, $D_c(F_1) = 0$ and $D_c(B) = D_c(I_0)$. That is the case for the exits consisting of a finite union of intervals. One example is provided by Fig. E.4, where $F_1 = \{\lambda\}$. If F_1 is infinite, however, $D_c(F_1)$ may be positive even if F_1 is countable (see [1], p. 103). The equality, $D_c(B) = D_c(I_0)$, is satisfied whenever $D_c(F_1) \leq D_c(I_0)$. In this case we also have $D_H(B) = D_c(B) = D_H(I_0) = D_c(I_0)$. The basin boundary dimension is greater than the invariant set dimension when $D_c(F_1) > D_c(I_0)$.

In numerical computation, the box-counting dimension is estimated from the uncertainty dimension (D_u) [1, 7]. It is conjectured that typically $D_u = D_c$ in dynamical systems (see [7] and references therein). Let us argue about this identity in our example. First we consider the invariant set I. A point x_0 is ε-uncertain if $(x_0 - \varepsilon, x_0 + \varepsilon) \cap I \neq \emptyset$, and we denote by $f_I(\varepsilon)$ the fraction of points that are ε-uncertain. The dimension of the invariant set is given by

$$D_u(I) = 1 - \lim_{\varepsilon \to 0} \frac{\ln f_I(\varepsilon)}{\ln \varepsilon}\ , \tag{E.5}$$

and it follows from (E.2) that $D_u(I) = D_c(I)$. Now we consider the boundary set B for F_1 finite. Introducing the exits E_1 and E_2, a point x_0 is ε-uncertain if $x_0 - \varepsilon$ and $x_0 + \varepsilon$ go out by different exits. The fraction of uncertain points is

$$\begin{aligned} f_B(\varepsilon) &= \alpha f_I(\varepsilon) + f_F(\varepsilon) \\ &= \alpha f_I(\varepsilon) + \beta f_I(\varepsilon), \end{aligned} \tag{E.6}$$

where α and β are constants. Here, $(1-\alpha) f_I$ is the fraction of points x_0 contributing to f_I but so that $x_0 - \varepsilon$ and $x_0 + \varepsilon$ are in the same basin, and it implies the term $\alpha f_I(\varepsilon)$. The contribution of the intrinsic frontier is $f_F(\varepsilon)$, which represents the scale structure of I for F_1. It implies the term $\beta f_I(\varepsilon)$. Accordingly,

$$\begin{aligned} D_u(B) &= 1 - \lim_{\varepsilon \to 0} \frac{\ln f_B(\varepsilon)}{\ln \varepsilon} \\ &= 1 - \lim_{\varepsilon \to 0} \frac{\ln f_I(\varepsilon)}{\ln \varepsilon} \\ &= D_c(I)\ \ (= D_c(I_0)). \end{aligned} \tag{E.7}$$

This identity allows the use of the uncertainty dimension, which has nice numerical properties, to calculate the box-counting dimension.

Back to Fig. E.2, the set of singularities (S) of the exit-time function (set of point where the exit-time is infinite) corresponds to the invariant set I. For the exit-time T, a point x_0 is ε-uncertain if $T(x_0 - \varepsilon) \neq T(x_0 + \varepsilon)$. Therefore, in the computation of the uncertainty dimension we are in fact estimating the box-counting dimension of the discontinuities of the exit-time function. (In this case there is no intrinsic frontier, since the exit-time is defined with respect to the total exit.) The set of discontinuities can be identified with L, forming sequences that converge to the singularities. It implies

$$D_u(S) = D_c(L) = D_c(I). \tag{E.8}$$

Once more the uncertainty dimension is the same as the box-counting dimension.

Although discussed for a specific case, the above results are far more general since our system models a vast class of exit systems. For any system with a finite number of basins, the dimension of the union of all basin boundaries is equal to the dimension of at least one of the boundaries. So, it is enough to consider systems with only one boundary (two exits, E_1 and E_2). When the effects of the intrinsic frontier are avoided, the basin boundary has the same dimension as the future invariant set. Since the latter set does not depend on E_1 or E_2 but just on $E_T = E_1 \cup E_2$, it leads to an invariance of the dimension with the definition of the basins. Roughly speaking, in spite of possible morphological changes, the basin boundary dimension will be the same for any nonpathological couple of exits E_1' and E_2' with positive probability of being reached, as long as $E_T = E_1' \cup E_2'$. Then, there is usually great freedom in defining the exits for a fixed total exit. This invariance of fractal dimension allows us to choose among several alternatives the best one to measure the invariant set dimension and hence the sensitivity of the system. Also, it gives us confidence that the result reflect a true dynamical property of the system and not an immaterial effect.

In this section we studied measurements of fractal dimensions when the total exit is fixed and, therefore, the invariant set is fixed. Next, in Sections E.3 and E.4, we discuss the complementary situation, that is, variations of the invariant set (and of its dimension) under changes of the total exit.

E.3 Dependences with the total exit

A fundamental feature of map (E.1) is the monotonous increase of the (future) invariant set dimension with the reduction of the parameter η. For $\eta > 1$, the invariant set is a zero measure set satisfying $D(I) \to 1$ for $\eta \to 1$. This property is very general and closely related to a conjecture of de Moura and Letelier [4] in the context of Hamiltonian systems: The dimension of the invariant set of a chaotic scattering system goes to the effective phase space dimension when the energy tends to the escape energy. In both cases the reduction of a parameter, η or the energy, blinds the exits and increases the number of oscillations of typical orbits before going out. Accordingly, it "fattens" the invariant set, increasing its dimension.

Let us consider an extension of the above situation to the one where the total exit is enlarged. Instead of $(1/2\eta, 1 - 1/2\eta)$ (the natural exit determined by points that go to $\pm\infty$) we define the new total exit $(1/2\eta - \alpha, 1 - 1/2\eta + \alpha)$ for $0 < \alpha < 1/2\eta$ and $\eta > 1$. The invariant set $I(\eta, \alpha)$ will be in $[0, 1/2\eta - \alpha] \cup [1 - 1/2\eta + \alpha, 1]$ and its dimension can be easily computed from the exit-time function. In Fig. E.5 we show the dimension of the invariant set as a function of α for $\eta = 1.1$. The fractal dimension is a decreasing function of α, but *not* strictly decreasing. The dimension presents a pattern of plateaux due to the existence of gaps in the invariant set. A gap $(1/2\eta - \alpha_2, 1/2\eta - \alpha_1) \cup (1 - 1/2\eta + \alpha_1, 1 - 1/2\eta + \alpha_2)$ in the invariant set $I(\eta, \alpha_1)$ implies a plateau in the interval (α_1, α_2): In increasing α the dimension changes only when the enlarged exit advances on points of the invariant set $I(\eta, \alpha)$. The result is a graph with a Devil staircase structure where the derivative is null in the complement of a Cantor set. Moreover, the limit of small α is well defined and recover the original dimension, that is, $D(I(\eta, \alpha)) \to D(I(\eta, 0)) = \ln 2 / \ln 2\eta$ for $\alpha \to 0$.

It is instructive to consider the invariant set explicitly in terms of its symbolic dynamics. A symbolic dynamics can be associated to the invariant set of map (E.1) as follows. For the exit $(1/2\eta, 1 - 1/2\eta)$, an invariant point $x_0 \in [0, 1]$ is represented by $0.\epsilon_0\epsilon_1 ... \epsilon_n ...$, where $\epsilon_n = 0$ if $M^n(x_0) \leq 1/2\eta$ and $\epsilon_n = 1$ if $M^n(x_0) \geq 1 - 1/2\eta$. The grammar of this dynamics is the Bernoulli shift grammar and $M^n(x_0)$ is represented by $0.\epsilon_n\epsilon_{n+1}...$. To simplify, suppose the exit is enlarged only on the left becoming $(1/2\eta - \beta, 1 - 1/2\eta)$, where β is so that points in $(1/2\eta - \beta, 1/2\eta)$ are represented by $0.011...1\epsilon_m\epsilon_{m+1}...$ for some integer m. The points of the invariant set with respect to the exit $(1/2\eta, 1 - 1/2\eta)$ that go out in at most $(k-1) \times m$ iterations are those points represented by sequences of 0 and 1 with the word $0\underbrace{11...1}_{m-1}$ somewhere in the first $k \times m$ letters. Subtracting these points, the number of invariant sequences with respect to $(1/2\eta, 1 - 1/2\eta)$ that remain invariant with respect to the exit $(1/2\eta - \beta, 1 - 1/2\eta)$ for $k \times m$ iterations is

$$N(k,m) = 2^{km}\left\{1 - \sum_{s=1}^{k}\left[\frac{(-1)^{s+1}}{2^{sm}}\sum_{i_s=1}^{(k-s)m+1}...\sum_{i_2=1}^{i_3}\sum_{i_1=1}^{i_2}1\right]\right\}. \tag{E.9}$$

It gives the scale of the hierarchical construction of the Cantor set structure, from which follows that the box-counting dimension of the new invariant set is

$$D_c(I(\eta,\beta)) = \lim_{k\to\infty}\frac{\ln N(k,m)}{\ln(2\eta)^{km}} . \tag{E.10}$$

For $m = 3$, the computation of the sequences in a different order leads to

$$N(k,3) = 2^{3k-1}\left\{\sum_{j=2}^{3k}a_j + \sum_{j=3}^{3k}b_j\right\}, \tag{E.11}$$

where $a_2 = b_3 = 1$,

$$a_j = -\frac{f_{j-2}}{2f_j}\sum_{i=2}^{j-1}a_i \text{ for } j \geq 3, \;\; b_j = -\frac{f_{j-1}-1}{2f_{j+1}-2}\sum_{i=3}^{j-1}b_i \text{ for } j \geq 4, \tag{E.12}$$

and $\{f_n\}$ are the Fibonacci numbers. The case $m = 2$ is trivial since $N(k,2) = 2k+1$ and the dimension of the invariant set is zero. The dimension computed from (E.9-E.12) is identical to that one computed by the uncertainty method. In Fig. E.6 we show this fractal dimension, normalized by the factor $\ln 2/\ln 2\eta$, as a function of m. The exit size is reduced as m is augmented, increasing the dimension.

The enlargement of exits is useful and sometimes necessary in numerical computation of fractal dimensions. An example is given by the orbits of light traveling around a black hole, as discussed in Section E.1. The difficulty in determining the final state (at the black hole or at infinity) is removed by enlarging the exit at infinity. The new exit may be defined as $r > r_0$, instead of $r = \infty$, where r is an adequate distance from the attractor center. The dimension so obtained is a lower bound of the exact invariant set dimension (associated to the original exits) since part of the invariant set is lost throughout the new exit.

This difficulty is present in a vast class of systems. It has frequently appeared in the literature where, in general, some kind of enlargement of the exits is implicitly taken into account. The above discussion intends to provide subsidies to clarify the effects of this procedure.

E.4 Transitions from exit to nonexit systems

Exits can be defined even when the system has no natural exits. As an example consider map (E.1) once more, but now for $\eta = 1$ (it is analogous for $1/2 < \eta < 1$). In such case the interval [0,1] is mapped to itself, and the symmetrical exit defined in Section E.3 reduces to $(1/2 - \alpha, 1/2 + \alpha)$. In Fig. E.7 we show a graph of the dimension of the (zero measure) invariant set as a function of α. The graph presents a pattern of plateaux similar to that one of Fig. E.5. In fact, it is a consequence of a simple relation existing between fractal dimensions for $\eta > 1$ and for $\eta = 1$. This relation follows from a one-to-one correspondence, via symbolic dynamics[2], between invariant sets for different values of η. In terms of symbolic dynamics, the exit $(1/2\eta - \alpha, 1 - 1/2\eta + \alpha)$ can be denoted by $E = (0.0\epsilon_1\epsilon_2... \,,\; 0.1\epsilon'_1\epsilon'_2...)$, where $\epsilon_i, \epsilon'_i \in \{0,1\}$ and $\epsilon_i + \epsilon'_i = 1$. This notation ignores the plateaux due to the original exit since $0.0\epsilon_1\epsilon_2... = \psi_\eta(\alpha)$ where the function ψ_η is constant on gaps of the original invariant set. Accordingly, from (E.2) follows that the box-counting dimensions for $\eta = 1$ and $\eta > 1$ differ just by the overall scale factor $\ln 2/\ln 2\eta$,

$$D_c(I(\eta, E)) = \frac{\ln 2}{\ln 2\eta} D_c(I(1, E)). \tag{E.13}$$

---

[2] For $\eta = 1$, all the interval $[0,1]$ is associated to the Bernoulli shift symbolic dynamics. The picture is analogous to that one for $\eta > 1$, except that the original invariant set (for $\alpha = 0$) has measure zero for $\eta > 1$ and measure one for $\eta = 1$.

(Relation (E.13) is valid for any exit, not only for the one considered here, e.g. Fig. E.6 where $d = D_c$ for $\eta = 1$.)

An important feature exhibited in Fig. E.7 is that the dimension is fractal and goes to 1 as α goes to 0. This behavior is closely related to the fact that the original map, with no exit, is chaotic: the map has a dense set of unstable periodic orbits and the Lyapunov exponent is positive ($h = \ln 2$). In order to better understand this relation, let us consider the logistic map $x_{n+1} = rx_n(1 - x_n)$ in the unit interval $[0, 1]$ for $r = 3.8$ (chaotic) and for $r = 2.8$ (nonchaotic). In Fig. E.8 we plot the exit-time function for $r = 3.8$ with respect to the exits $(0.61, 0.69)$ (Fig. E.8(a)) and $(0.63, 0.67)$ (Fig. E.8(b)). These graphics present successive steps in the construction of the Cantor structure of the invariant set. They must be compared with Fig. E.9, where we show exit-times for $r = 2.8$. The exit-time for $r = 3.8$ presents a complex structure that becomes even more complex when the exit is reduced. It reflects the increasing of the invariant set dimension: $D_u \approx 0.62$ in Fig. E.8(a), $D_u \approx 0.88$ in Fig. E.8(b), and $D_u \to 1$ in the limit of small exit. A different behavior takes place when $r = 2.8$. In fact, Figs. E.9(a) and E.9(b) show a regular exit-time where no complexity is added when the exit is reduced. In terms of invariant set dimension it means that its value is zero even in the limit of small exit. The transition of the dimension of the invariant set from small exit to no exit is, in this case, discontinuous since it jumps from 0 to 1.

The behavior described in preceding paragraphs is very general and may be summarized as follows: Chaotic nonexit systems present invariant sets with *fractal* dimension when small exits are defined[3], and the invariant set dimension tends to the effective phase space dimension when the exits are arbitrarily reduced. On the other hand, nonchaotic nonexit systems do not present any fractal structure in the invariant set when exits are introduced, and the invariant set dimension jumps (discontinuously) to the effective phase space dimension when the exits are removed[4]. We conjecture that this behavior is typical

---

[3] The exits have to be sufficiently small in order to avoid the complete outcome of the invariant set.

[4] There are pathological examples of nonchaotic systems which exhibit fractal properties when exits are created (see [9]). It happens when the invariant set of the exit system is fractal but nonchaotic. This behavior is, however, atypical.

for dynamical systems in general.

Basically, this conjecture states that chaos in closed systems and fractals in open systems are different manifestations of the same phenomenon. Chaos in closed systems is essentially determined by the presence of a somewhere dense set of unstable periodic orbits. Fractal structures in exit systems are determined by a fractal invariant set that consists of unstable periodic orbits and an uncountable number of nonperiodic orbits surrounding them. Therefore, the introduction and removal of exits leads from one situation to the other. (In most cases, because of the density property, the box-counting dimension of the periodic orbits equals the invariant set dimension in exit systems and the effective phase space dimension in closed systems.) Physically, an exit system with fractal invariant set evolves chaotically for a period of time before being scattered. When the exits are removed the system evolves chaotically forever. Conversely, chaotic nonexit systems present sensitive dependence on initial conditions. The introduction of small exits detect this sensitivity through singularities on exit-times, scattering functions, etc.

Besides the chaotic and nonchaotic behavior mentioned above the system can also experience a chaotic transient. That is the case for the period three windows of the logistic map. For $r = 3.84$ the period three orbit $\{x_n\} = \{0.1494, 0.4880, 0.9594, ...\}$ attracts all orbits of the interval $[0, 1]$ except an uncountable, zero measure set of orbits which never settle into the periodic cycle (see Ref. [1], pages 49 and 157). The invariant set dimension results $D_u \approx 0.86$ for the exit $(0.44, 0.52)$ and $D_u \approx 0.90$ when the exit (containing an attracting point) is arbitrarily reduced. In this case the limit of small exit reveals an invariant set - the set of nonattracted orbits - whose fractal dimension is less than the effective phase space dimension.

Now let us consider a couple of related works, [5] and [10]. In the former, the authors study the Sinai billiard with two holes in the external wall. They show that the boundary between the initial-condition basins defined by the two exits is fractal. In the context of our discussion, this result is a consequence of the well known chaotic dynamics of the (closed) Sinai billiard. In addition, we verified numerically that the basin boundary dimension in fact tends to the effective phase space dimension when the two exits are reduced. In the latter work, the question over whether or not the Bianchi IX cosmological model is chaotic is finally solved. The trouble with this question is that standard indicators of chaos, like Lyapunov exponents, are not invariant under space-*time* diffeomorphisms and cannot be used since the model is relativistic. Following a suggestion first made by [11], the authors show that the system is chaotic by defining three exits and measuring the basin boundary dimension. (The approximation of the dimension to the effective phase space dimension when the exits are reduced was also verified.) In that work, the relation between exit and nonexit systems together with the invariant character of fractal methods played a fundamental role in the solution of the problem.

The potential use of our conjecture as an invariant method to study chaos in closed systems of several dimensions is considered in [12].

E.5 Conclusions

We have studied, via examples, a number of questions concerning fractals in exit systems. In particular the three questions stated in Section E.1 were discussed in Sections E.2, E.3 and E.4, respectively. We observed that basin boundary dimensions are independent of the definitions of the exits since the total exit is fixed and the intrinsic frontier effects are avoided. The dimensions increase, however, with the reduction of the total exit. Our main result refers to the limit of small exits, where a distinctive behavior was found concerning whether the corresponding closed system is chaotic or not. In the former the dimension goes to the effective phase-space dimension, while in the latter it jumps avoiding noninteger values. Special attention was also given to understand the relations between the dimensions of different fractal sets, and the relations between different concepts of dimension.

Finally, we stress that most of the results presented here are also valid for nonhyperbolic systems [7]. It is the case of the invariances of fractal dimensions discussed in Section E.2, since the arbitrariness in choosing the exits is analogous in hyperbolic and nonhyperbolic systems. Concerning Section E.3, the dimension can change with the total exit when the nonhyperbolic character is lost in enlarging the exit. In such case, the behavior of hyperbolic systems discussed in Section E.3 takes place. Nonhyperbolic exit systems, however, can present invariant sets with maximal dimension (equal to the dimension of the effective phase space) [7]. In this sense, and in the context of Section E.4, the relation between closed and open nonhyperbolic systems is even stronger than in the hyperbolic analogous.

Acknowledgements

The authors thank Fapesp and CNPq for financial support.

Appendix

The following definitions refer to phase spaces of autonomous systems for both maps (discrete time) and vector fields (continuous time): (1) An *exit* E is any set of the phase space (possibly at infinity) which may be reached in a finite time or asymptotically. Orbits are considered exited when arrive at E. (2) The *total exit* E_T is the union of all exits of the system. (3) The *size* of an exit is given by its phase space volume, and an exit E is *smaller* than another exit E' if E is a proper subset of E'. The size of the total exit is defined analogously. (4) Given a set of exits $E_1, E_2, ..., E_n$, the *basin* A_i of the exit E_i is the set of all initial conditions whose time evolution reaches E_i before reaching any other exit[5]. (5) The *basin boundary* $B_{i_1,...,i_k}$ is the set of points arbitrarily close to points of A_{i_1},..., $A_{i_{k-1}}$, and A_{i_k}. (6) A *scattering function* is a function that describes the behavior of the final phase space variables (when the exits are reached) as a function of the initial ones. (7) The *exit-time function* ("time delay" in scattering processes) is a function which associates to the initial conditions the minimal time needed to reach the total exit. (8) The *nonattracting invariant set* is a set composed by nonattracting orbits that do not reach any exit (not even asymptotically) for both directions of the time. Its *stable* and *unstable manifolds*, when exist, are the future and past invariant sets, respectively.

---

[5] A_i can be defined as the closure of this set, with no relevant changes.

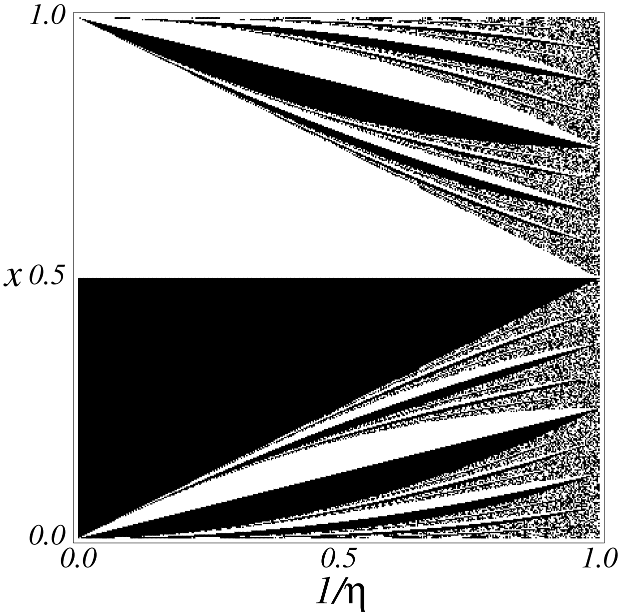

Figure E.1: Portrait of the basins of map (E.1) as a function of η. The initial conditions were chosen on a grid of 400 × 400. Regions in black and white correspond to orbits that escape to $+\infty$ and $-\infty$, respectively.

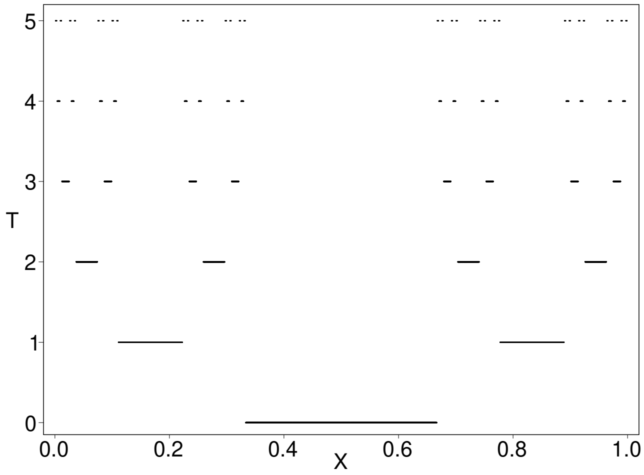

Figure E.2: Exit-time of map (E.1) for $\eta = 3/2$ and total exit $(1/2\eta, 1 - 1/2\eta)$.

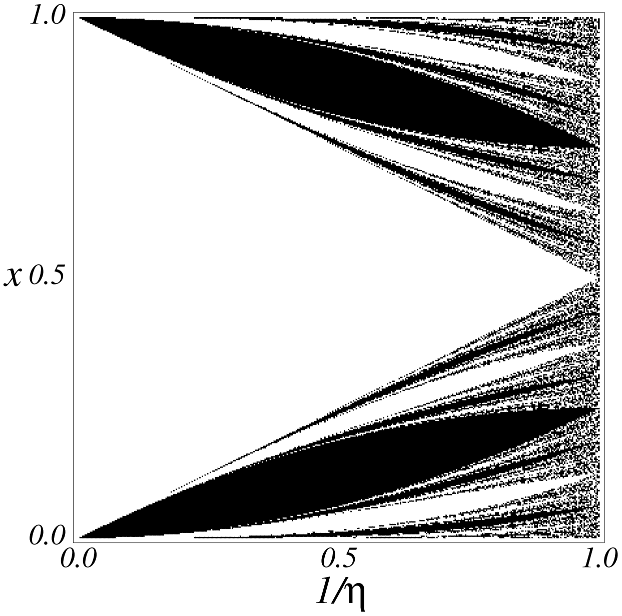

Figure E.3: Portrait of the basins of map (E.1) as a function of η. The initial conditions were chosen on a grid of 400×400. Regions in black and white correspond to orbits that escape from $[0, 1]$ in an even and an odd number of iterations, respectively.

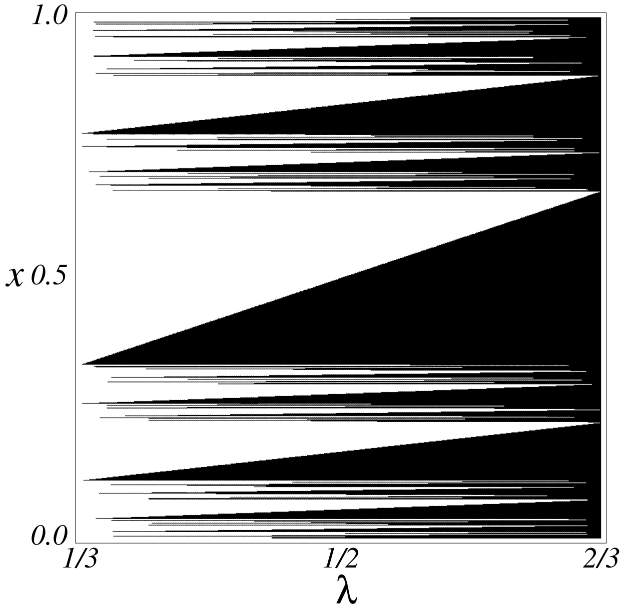

Figure E.4: Portrait of the basins for map (E.1) as a function of λ for $\eta = 3/2$. The initial conditions were chosen on a grid of 800×800. Regions in black and white correspond to orbits that escape to $(1/2\eta, \lambda]$ and $(\lambda, 1 - 1/2\eta)$, respectively.

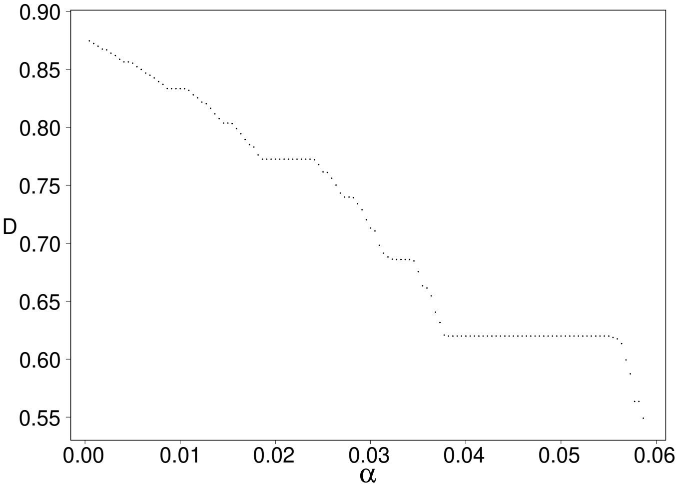

Figure E.5: Uncertainty dimension of the invariant set of map (E.1) for $\eta = 1.1$ and total exit $(1/2\eta - \alpha, 1 - 1/2\eta + \alpha)$ as a function of α.

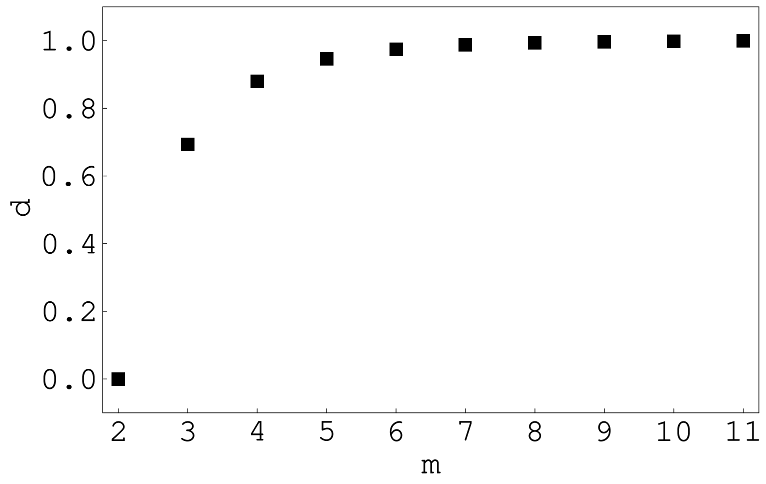

Figure E.6: The normalized box-counting dimension $d = D_c \ln 2\eta / \ln 2$ of the invariant set of map (E.1) for the total exit $(1/2\eta - \beta, 1 - 1/2\eta)$ as a function of m.

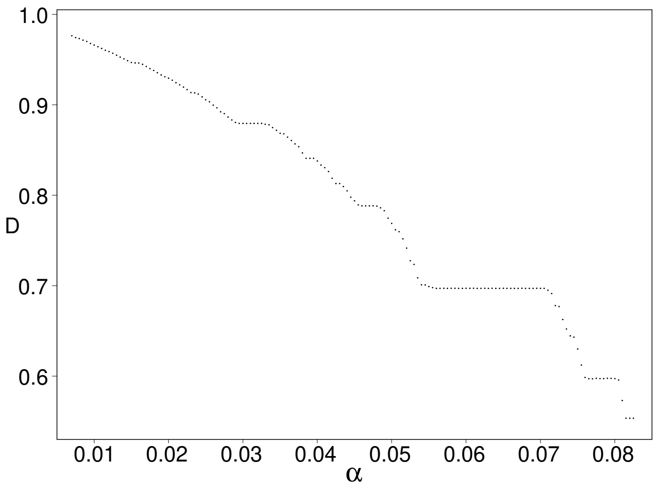

Figure E.7: Uncertainty dimension of the invariant set of map (E.1) for $\eta = 1$ and total exit $(1/2 - \alpha, 1/2 + \alpha)$ as a function of α.

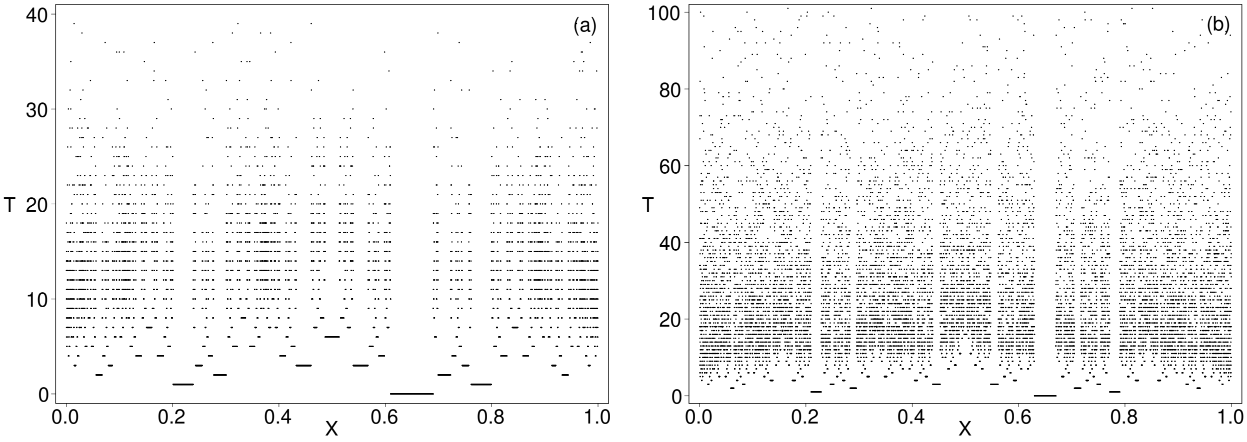

Figure E.8: Exit-time of the logistic map for $r = 3.8$ with total exit: (a) $(0.61, 0.69)$; (b) $(0.63, 0.67)$.

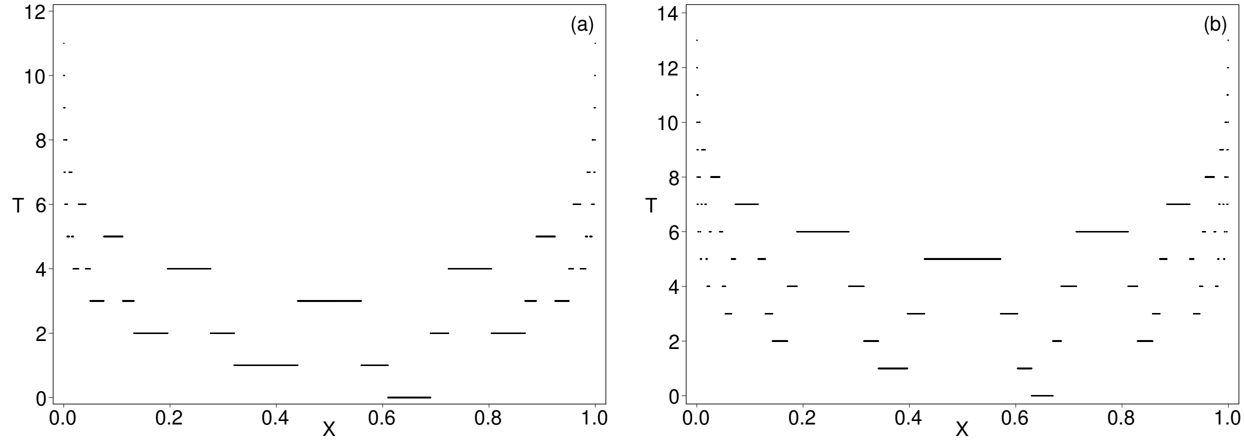

Figure E.9: Exit-time of the logistic map for $r = 2.8$ with total exit: (a) $(0.61, 0.69)$; (b) $(0.63, 0.67)$.

Bibliography

[1] E. Ott, *Chaos in Dynamical Systems* (Cambridge University Press, Cambridge, 1994).

[2] C. Grebogi, E. Kostelich, E. Ott, and J.A. Yorke, Physica D **25**, 347 (1987).

[3] Q. Chen, M. Ding, and E. Ott, Phys. Lett. A **145**, 93 (1990).

[4] A.P.S. de Moura and P.S. Letelier, Phys. Lett. A **256**, 368 (1999).

[5] S. Bleher, C. Grebogi, E. Ott, and R. Brown, Phys. Rev. A **38**, 930 (1988).

[6] S. Chandrasekhar, *The Mathematical Theory of Black Holes* (Oxford University Press, Oxford, 1992).

[7] Y.T. Lau, J.M. Finn, and E. Ott, Phys. Rev. Lett. **66**, 978 (1991).

[8] K. Sandau, Physica A **233**, 1 (1996).

[9] G. Troll, Chaos Soliton Fract. **7**, 1929 (1996).

[10] A.E. Motter and P.S. Letelier, Phys. Lett. A **285**, 127 (2001).

[11] N.J. Cornish and J.J. Levin, Phys. Rev. Lett. **78**, 998 (1997).

[12] A.E. Motter and P.S. Letelier, "A fractal method for chaos in conservative closed systems of several dimensions", nlin.CD/0101021, submitted.

F

A fractal method for chaos in conservative closed systems of several dimensions

Adilson E. Motter, Patricio S. Letelier, submetido à Physica D.

We present a fractal method to detect, locate and quantify chaos in multidimensional, conservative, closed systems. The method is invariant under space-time changes of coordinates and can be used to analyze both classical and relativistic Hamiltonian systems with more than two degrees of freedom. As an application of the method we study coupled standard maps associated with a periodically kicked rotor of $2\frac{1}{2}$ degrees of freedom.

PACS numbers: 05.45.Df, 05.45.Jn.

F.1 Introduction

In the last century the mathematical basis of deterministic chaos in compact phase space (closed) systems has become clear [1], and a number of methods have allowed the study of a vast class of particular cases. Important examples of these methods are the Melnikov method, the Poincaré section method, and the Lyapunov exponents method [1, 2]. Alas, the first and second methods are hard to be used in high dimensional systems and the Lyapunov exponents are not invariant under space-time changes of coordinates [3]. Accordingly, the majority of the coordinate invariant results obtained so far refer to systems of $1\frac{1}{2}$ or two degrees of freedom.

Fractal methods, on the other hand, are coordinate independent and can be used in any dimension. These methods have been largely applied in the characterization of the chaotic dynamics of dissipative systems, especially in the study of attractors and basin boundaries [2]. Fractal techniques have also been employed to analyze scattering processes and chaotic transients in conservative systems with exits (open systems) [4].

The aim of this communication is to propose an invariant method to detect, locate and quantify chaos in closed systems of several dimensions. More specifically, we are interested in bounded (recurrent) motions taking place in the absence of attractors and *natural* exits. The establishment of such a method is pertinent since the standard fractal methods cannot be applied to these cases. Roughly speaking, our method consists of the definition of adequate *artificial* exits in the original phase space, and the application of fractal type techniques to analyze the corresponding sets of exiting and nonexiting orbits. This *fractal method for closed systems* (FMCS) provides graphic means to locate the chaotic and regular regions on phase space slices. It also leads to an algorithm to determine the chaotic and regular fractions of the phase space volume. Different from the above mentioned methods, the FMCS can be used to study classical as well as relativistic Hamiltonian systems with more than two degrees of freedom. In some sense the FMCS may be seen as a higher-dimensional generalization of the Poincaré section method.

In this paper we first establish a conjecture that will support the FMCS. In Section F.3 we present the method divided in three parts: (*i*) to determine whether the system is chaotic or not; (*ii*) to locate the chaotic and regular regions on a two-dimensional surface of section; (*iii*) to compute the chaotic and regular fractions of the phase space volume. In Section F.4 we consider the application of the FMCS to coupled standard maps. Finally, we present our conclusions in the last Section.

F.2 Chaos and fractals

One could say that a system is chaotic if it presents both sensitive dependence on initial conditions and mixing in a nonzero volume of the phase space. This definition, however, is not adequate since it may depend on the time parametrization of the system [3, 5]. A time independent definition that solves this problem was given by Churchill [6]: The system is chaotic if it is topologically transitive and the set of (points of) compact orbits is dense, in some positive volume of the phase space. In less technical terms, we define the system as chaotic if it presents, besides transitivity [7], a somewhere dense set of infinitely many unstable periodic orbits. Chaotic systems may exhibit not only chaotic but also nonchaotic (regular) regions. This concept of chaos is consistent with the general principle that chaos prevents integrability in the chaotic regions.

We shall consider each m-dimensional manifestly invariant part of the phase space (e.g., each energy surface) of autonomous closed systems, for which we define the following: (1) An *exit* E is an m-dimensional region of the phase space, so that orbits are considered out of the system when they arrive at E. (2) The *basin* B_E is the closure of the set of initial conditions whose orbits reach E. (3) The *invariant set* I_E is the set of interior points of B_E whose orbits do not reach E.

The possible chaotic behavior of the system is determined by the nature of its invariant sets. For a small exit defined in a chaotic region [8], the Hausdorff dimension [2] of the invariant set is fractional and tends to the maximum value m (the dimension of the ambient space) when the size of the exit is arbitrarily reduced. (In the case of nonhyperbolic dynamics, the maximum value m can be obtained for exits of finite size [9].) On the other hand, invariant sets associated with exits defined in regular regions do not present any fractal structure, and their dimensions jump (discontinuously) avoiding fractional values when the exits are removed. We conjecture that this behavior is typical for dynamical systems in general [10].

This conjecture states that, in general, chaos in closed systems and fractals in exit systems are both determined by unstable periodic orbits. Fractal invariant sets are typically chaotic in exit systems and chaos in closed systems is associated with the existence of fractal invariant sets. Therefore, the introduction and removal of exits leads from one situation to the other. Physically, an exit system with fractal invariant set evolves chaotically for a period of time before being scattered. When the exits are removed the system evolves chaotically forever. Further details about this conjecture can be found in Ref. [11].

F.3 Fractal method

The above conjecture can be used to obtain a method to study chaos in conservative closed systems of several dimensions ($2\frac{1}{2}$ or more degrees of freedom in the Hamiltonian case). In what follows we present one possible implementation of such a method, the FMCS.

In order to have an insight into where to look for chaos, we consider the volume of the phase space accessed by a sample of orbits. The idea is that in a chaotic region almost all orbits access approximately the same volume (the volume of that chaotic component). Regular orbits are expected to access lower dimensional surfaces that are arranged in families (of torus in Hamiltonian systems) with increasing area.

First we divide the phase space with a grid and then we evolve a sample of random initial conditions for a large period of time, counting the number of cells of the grid visited by each orbit. In a histogram of the number of orbits as a function of the number of visited cells, peaks suggest the possible existence of chaotic regions. We take these regions as candidates for chaos. With a search program, a subregion (a ball, for example) can be located inside each of these regions. We define an exit in the subregion of the candidate region for chaos that we want to study, and we compute (numerically) the dimension of the corresponding invariant set. Then we use our conjecture to conclude whether the region is chaotic or not. That is the first part of the FMCS.

Given an exit E defined in a chaotic region, the chaotic region itself is exactly the interior of the basin of E. To locate the chaotic and regular regions on a two-dimensional surface S in the phase space, we define one exit in each chaotic component of the system. Then we take initial conditions on a grid in S and we evolve these points until the rate of orbits arriving at the exits becomes negligible. The regular regions, corresponding to points whose orbits do not reach the exits, can be appropriately plotted in a two-dimensional graph. In this graph, the chaotic regions are represented by the blank area. That is the second part of the FMCS.

A straightforward extension of the procedure in the preceding paragraph allows us to compute the chaotic and regular fractions of the phase space volume. That is the third part of the FMCS, where the chaotic regions are identified from the evolution of points randomly chosen everywhere in the phase space. The chaotic fraction (c_f) is then given by the quotient between the number of initial points in the chaotic regions and the total number of initial conditions. Naturally, the regular fraction (r_f) is determined by the condition $r_f + c_f = 1$.

Finally, consistency tests can be made in order to check the results and the hypotheses involved in the FMCS. The possibility that two or more disconnected chaotic components are associated with the same peak of the histogram, for instance, can be verified by comparing the fraction of the volume of each chaotic component with the fraction of points in the corresponding peak of the histogram. The volume of each chaotic region is limited by the corresponding fraction of visited cells. In addition, the stability of the results should be tested by taking different grid sizes, periods of evolution, exits, etc.

The last remark of this section concerns the computation of the dimension of the invariant sets. A technique that demands a small computational effort consists of computing the uncertainty dimension [9] of the set of singularities of the *escape time function* defined on a smooth (one-dimensional) curve C: the escape time $t = t(\lambda)$ is the time required by orbits from initial points $x(\lambda)$ in C to reach E, where λ parameterizes the curve; the singularities of t correspond to points whose escape time is infinite (points of the invariant set). We measure the uncertainty dimension by applying an algorithm presented in Ref. [9]. A parameter value λ_0 is called ε-uncertain if $\mid t(\lambda_0 + \varepsilon) - t(\lambda_0 - \varepsilon) \mid \geq \Delta$, where Δ is a positive number. We compute the fraction $f(\varepsilon)$ of ε-uncertain points for a large number of random values of the parameter λ, and for different values of ε going to zero. The asymptotic behavior of this function is expected to be of the form $f(\varepsilon) \approx \varepsilon^{\alpha}$ for any Δ, where α is the uncertainty exponent, and $d = 1 - \alpha$ is the uncertainty dimension. The nonfractal case corresponds to $d = 0$ and the fractal one to $0 < d \leq 1$. In the fractal case, the Hausdorff dimension [12] of the (total) invariant set is supposed to be typically equal to $D = m - 1 + d$.

F4. Example

The KAM surfaces cannot isolate the chaotic layers in nonintegrable Hamiltonian systems with three or more degrees of freedom [13]: All the chaotic volume is joined together into a single global structure or, at most, into a finite number of disjoint components. In such components, chaotic orbits are expected to get arbitrarily close to any point energetically accessible. The hypotheses of our method are therefore satisfied for each value of the energy, and the FMCS is supposed to work in Hamiltonian systems of more than two degrees of freedom. We follow with an example of a Hamiltonian-like system that has an analytical expression for its discrete form.

Section maps can be explicitly obtained for periodically kicked rotors of $2\frac{1}{2}$ degrees of freedom. A simple example is given by the time dependent Hamiltonian

$$H = \frac{I_1^2}{2m_1} + \frac{I_2^2}{2m_2} + \frac{f(\theta_1, \theta_2)}{(2\pi)^2} \sum_n \delta(t - n\tau), \tag{F.1}$$

where $\tau/m_1 = \tau/m_2 = 1$ and $f(\theta_1, \theta_2) = K \cos(2\pi\theta_1)\cos(4\pi\theta_2)$, which is equivalent to an autonomous Hamiltonian with three degrees of freedom for a fixed value of the energy. Integrating the delta function at $t = n\tau$ we obtain a four-dimensional map on $[0,1]\times[0,1]\times[0,1]\times[0,1]$:

$$I_1^{(n+1)} = I_1^{(n)} + \frac{K}{2\pi} \sin(2\pi\theta_1^{(n)}) \cos(4\pi\theta_2^{(n)}) \mod 1, \tag{F.2}$$

$$I_2^{(n+1)} = I_2^{(n)} + \frac{K}{\pi} \cos(2\pi\theta_1^{(n)}) \sin(4\pi\theta_2^{(n)}) \mod 1, \tag{F.3}$$

$$\theta_1^{(n+1)} = \theta_1^{(n)} + I_1^{(n+1)} \mod 1, \tag{F.4}$$

$$\theta_2^{(n+1)} = \theta_2^{(n)} + I_2^{(n+1)} \mod 1. \tag{F.5}$$

These expressions are coupled standard maps [13].

Let us consider system (F.2-F.5) for $K = 0.5$. We divide the phase space with a square grid of $16 \times 16 \times 16 \times 16$ (65536 cells). Then we compute the number N of cells visited by orbits from 150000 random initial points in 400000 iterations. The result is plotted in the histograms of Fig. F.1. In Fig. F.1(a) it can be seen that the histogram presents only two main peaks. In Figs. F.1(b) and F.1(c) we show refinements of each main peak. These peaks do not present smaller isolated peaks. The peak near $N = 0$ (peak I) is consistent with the hierarchical distribution expected for regular regions. The peak near $N = 64000$ (peak II), however, may be associated with chaotic regions. We define as region I and region II the sets of initial conditions associated with peak I and peak II, respectively. Considering these initial conditions we find that all the points in the ball of radius $r = 0.23$ and center $(I_1, \theta_1, I_2, \theta_2) = (0.278, 0.510, 0.450, 0.761)$ are in region II. We denote this ball by E_0, and we use it as an exit to analyze region II.

In Fig. F.2(a) we show the escape time corresponding to points randomly taken on the curve $C := \{I_1 = \theta_1 = \lambda, I_2 = \theta_2 = 0.5 \mid 0.1 < \lambda < 0.2\}$. The complicated structure of this graph is present in arbitrarily large magnifications of the interval. In Fig. F.2(b) we show a 50 times magnification that exhibits this property. That is a graphical characteristic of fractals. In fact, a numerical computation of the uncertainty exponent in the interval of Fig. F.2(a) results in $\alpha = 0.05 \pm 0.01$ for $10^{-13} < \varepsilon < 10^{-9}$ (± 0.01 represents the statistical error). In the interval of Fig. F.2(b) the exponent results in $\alpha = 0.03 \pm 0.01$ for $10^{-13} < \varepsilon < 10^{-9}$. By numerically estimating this exponent in smaller and smaller intervals, we approach asymptotically to $\alpha = 0$. It means that the uncertainty dimension corresponding to Figs. F.2(a) and F.2(b) actually results in $d \approx 1$. This result is consistent with the nonhyperbolic character of the system, since in nonhyperbolic systems the invariant set dimension is supposed to be maximal [9]. Independently of the exact value of d, the fact that $0 < d \leq 1$ is enough to conclude that region II is chaotic.

Now, let us consider the section $S := \{(I_1, \theta_1, I_2, \theta_2) \mid I_2 = \theta_2 = 0.5\}$. In order to determine the regular and chaotic regions on S, we compute the intersection between S and the basin of the exit E_0. For initial conditions taken on a grid of 400×400, to a good approximation the chaotic points correspond to orbits that outcome in less than 50000 iterations. Both chaotic and regular regions are plotted in Fig. F.3, from which some physical results can be directly obtained. For example, since the chaotic region connects line $I_1 = 0$ with line $I_1 = 1$, the periodicity in I_1 implies that the chaotic region actually runs from $I_1 = -\infty$ to $I_1 = +\infty$ [2]. Thus, the evolution of an initial condition in the chaotic region goes to arbitrarily large energies.

In addition, we compute the chaotic fraction of the phase space volume. The basin of E_0 is estimated by evolving 150000 random initial points over 50000 iterations. For $K = 0.5$ the chaotic fraction results in $c_f = 0.975 \pm 0.005$. The confidence on this result comes from the fact that no significant changes are observed for 100000 and 400000 iterations. As a function of the parameter K, the chaotic fraction goes from zero for $K = 0$ (nonchaotic) to one for $K \approx 1.1$ (completely chaotic).

F.5 Final remarks

In this communication we presented a fractal method to study chaos in closed systems of several dimension, the FMCS. The method can be applied to conservative systems in general, not necessarily Hamiltonian. The FMCS is simple from the conceptual viewpoint and is of easy numerical implementation, since it consists of the adequate definition of exits and the subsequent analysis of the corresponding basins and invariant sets.

The importance of this method is twofold: (1) In classical systems, which are provided with an absolute time parameter, it appears as a systematic method to study chaos in phase spaces of several dimensions; (2) In relativistic systems, that are invariant under space-time diffeomeophisms, this invariant method presents the nice property of avoiding coordinate effects, i.e. the results are independent of the space-time parameters used.

Finally, we consider the limitations of our method. The first one concerns the difficulty of the method in locating small chaotic regions. The method is more efficient in systems with large chaotic regions. In addition, the definition of exits completely inside the chaotic regions may be, sometimes, impossible. The difficulty is due to the presence of small regular regions embedded in the chaotic regions. The effect of these small regions is expected to be negligible, however. The last problem refers to points near the boundaries between chaotic and regular regions. Regarding these points, it is difficult to determine whether their orbits are chaotic or regular. All these problems are intrinsic of numerical methods and are also present, for instance, in the Poincaré section method.

Acknowledgements

The authors thank F. Bonjour, Y.-C. Lai, A.P.S. de Moura, T. Nishikawa, M.T. Ujevic, and R.R.D. Vilela for their valuable comments, as well as Fapesp and CNPq for financial support.

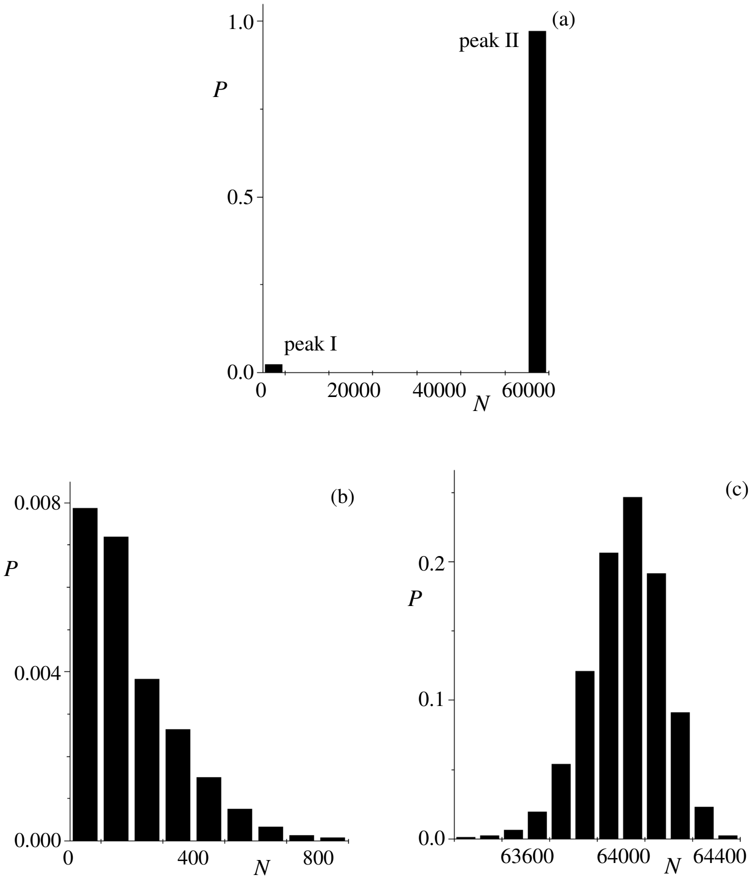

Figure F.1: Histograms of the relative number P of orbits that visit a number N of cells in a grid of $16 \times 16 \times 16 \times 16$, for $K = 0.5$. Orbits from 150000 random initial conditions were computed for 400000 iterations. (a) The histogram of all orbits. (b) Refinement of peak I. (c) Refinement of peak II.

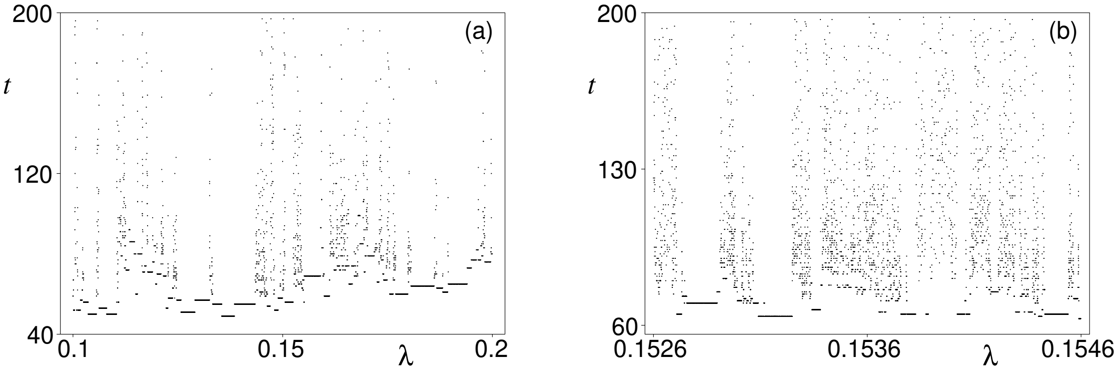

Figure F.2: Escape time relative to the exit E_0 for $K = 0.5$. (a) 10000 points randomly taken on $C := \{I_1 = \theta_1 = \lambda,\, I_2 = \theta_2 = 0.5 \mid 0.1 < \lambda < 0.2\}$. (b) A portion of (a) magnified 50 times.

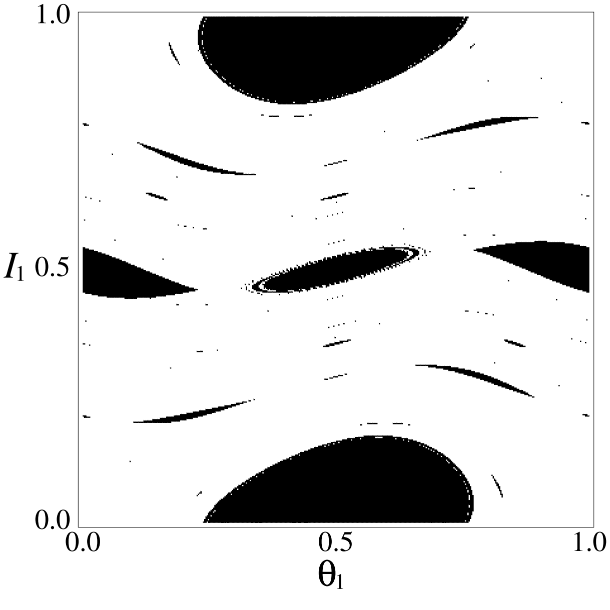

Figure F.3: Portrait of the regular (in black) and chaotic (in blank) regions on $S := \{(I_1, \theta_1, I_2, \theta_2) \mid I_2 = \theta_2 = 0.5\}$ for $K = 0.5$.

Bibliography

[1] J. Guckenheimer and P. Holmes, *Nonlinear Oscillations, Dynamical Systems, and Bifurcations of Vector Fields* (Springer-Verlag, New York, 1983).

[2] E. Ott, *Chaos in Dynamical Systems* (Cambridge University Press, Cambridge, 1994).

[3] G. Francisco and G.E.A. Matsas, Gen. Relativ. Gravit. **20**, 1047 (1988).

[4] For example, S. Bleher, C. Grebogi, E. Ott, and R. Brown, Phys. Rev. A **38**, 930 (1988); Chaos Focus Issue **3**(4) (1993).

[5] B.R. Fayad, *Analytic mixing reparametrizations of irrational flow*, Centre de Mathématiques, Ecole Polytechnique, preprint 2000-07.

[6] R.C. Churchill, in: *Deterministic Chaos in General Relativity*, edited by D. Hobill, A. Burd, and A. Coley (Plenum Press, New York, 1994).

[7] R.L. Devaney, *An Introduction to Chaotic Dynamical Systems* (Addison-Wesley, New York, 1989).

[8] The exit has to be sufficiently small in order to avoid the complete outcome of the invariant set.

[9] Y.T. Lau, J.M. Finn, and E. Ott, Phys. Rev. Lett. **66**, 978 (1991).

[10] There are pathological examples of nonchaotic systems that exhibit fractal properties when exits are created (e.g., systems with degenerate resonances on a Cantor set [G.

Troll, Chaos Soliton Fract. **7**, 1929 (1996)]). It happens when the invariant set of the exit system is fractal but nonchaotic. This behavior is, however, atypical.

[11] A.E. Motter and P.S. Letelier, Regular and Chaotic Dynamics **6**, 215 (2001).

[12] For invariant sets of dynamical systems, it is widely accepted that the Hausdorff dimension is typically equal to the box-counting dimension [2], and that the box-counting dimension is typically equal to the uncertainty dimension [9].

[13] A.J. Lichtenberg and M.A. Lieberman, *Regular and Stochastic Motion* (Springer-Verlag, New York, 1983).

Mixmaster chaos

G

Adilson E. Motter, Patricio S. Letelier, Physics Letters A **285**, 127 (2001).

The significant discussion about the possible chaotic behavior of the mixmaster cosmological model due to Cornish and Levin [N.J. Cornish, J.J. Levin, Phys. Rev. Lett. 78 (1997) 998; Phys. Rev. D 55 (1997) 7489] is revisited. We improve their method by correcting nontrivial oversights that make their work inconclusive to precisely confirm their result: "The mixmaster universe is indeed chaotic".

PACS numbers: 98.80.Hw, 05.45.Df.

The Bianchi IX (mixmaster) cosmological model was investigated by Belinskii, Khalatnikov and Lifshitz (BKL), clarifying the nature of cosmological singularities (see [1] and Refs. therein), and by Misner, in his attempt to solve the cosmological horizon problem [2]. The subsequent emergence of chaos in maps associated with this model attracted the attention of several researchers in the following years. Later, it was realized that standard chaotic indicators used in previous works, like Lyapunov exponents, were not invariant under space-*time* diffeomorphisms (see [3] for a comprehensive discussion). Since then, a number of contributions looking for coordinate independent manifestations of chaos have appeared in the literature, and the mixmaster cosmology has become one of the main paradigms of deterministic chaos in General Relativity. Even though some important results have been obtained, a satisfactory comprehension of chaos in this system remains to be achieved (see [4] for a critical review). Among the most promising proposals we mention the efforts of Szydlowski and collaborators in treating the problem in terms of (invariant) curvature [5]. This approach, however, breaks down in the mixmaster case [4]. Another significant progress was recently made by Cornish and Levin (CL) [6]. Employing fractal techniques, the authors obtained evidences of chaotic transients in the mixmaster model. However, this work is inconclusive due to conceptual flaws. Accordingly, the existence of invariant chaos in the mixmaster cosmological model is still an open question.

In dynamical systems, chaos seems to be the rule rather than the exception (at least for generic autonomous systems with three or more equations). Based on this fact, there is small risk in declaring in advance that a system is chaotic. In addition, even in nonchaotic systems, technical errors in general lead to some kind of numerical chaos. Therefore, the relevance of stating that a particular system is chaotic stays on the precision of the proof and the nature of the chaos revealed by it [7]. In the case of the mixmaster universe it also stays on the need of a proper meaning for invariant chaos in General Relativity.

The aim of this communication is to show unequivocally that the mixmaster dynamics is chaotic in a precise sense. First we review critically the work by CL, pointing out some key oversights. Second, we propose modifications and corrections of the CL's procedure. Next, this new procedure is employed to the approximate dynamics and then to the exact dynamics. From the full dynamics analysis we conclude that the mixmaster model does evolve chaotically.

The work by CL is based on the enlargement of the three outcomes of the mixmaster universe and on the study of the invariant set through fractal methods of chaotic scattering. Hence, the existence of a fractal structure in the invariant set would imply chaotic transients. First they studied an approximation of the exact dynamics, the Farey map, whose invariant set can be exhibited explicitly. For this map, the topological entropy and the information dimension of the invariant set were computed. Then, by numerically computing the information dimension for a choice of the outcomes, the full dynamics was studied. Based on the noninteger value of the resulting information dimension, the authors declared that the system is chaotic.

In checking the CL's papers we found that: (1) Concerning the Farey map, the invariant set exhibited, a Cartesian product of periodic points of the epoch-era BKL map [1], is not invariant. In contrast to the authors' belief, only points with the same period in both Cartesian components are periodic points of the Farey map. Consequently, the conclusions obtained from this 'invariant set' are wrong or at best suspicious. For instance, their result for the topological entropy is twice as bigger as the correct value because what they found was the square of the number of periodic points that really exist. (2) In the full dynamics counterpart, the information dimension was computed from the box-counting dimension of the basin boundaries, based on a result presented in Ref. [8] - the information dimension of a set may be given by the box-counting dimension of an *optimal* fraction of the set (see [9], p. 83) - that does not apply to this case since the optimal condition is not satisfied. Moreover, the initial conditions, given near the moment of maximal expansion, were parametrized by parameters from Chernoff-Barrow (CB) map and the outcomes were defined in terms of one of these parameters [10]. Since the CB map cannot be applied far away from the cosmological singularities, this parametrization is violated during the integration and is recovered only when the Kasner approximation becomes valid. Accordingly, the outcomes are not well defined for all time and they make sense only when a Kasner approximation is made. Consequently, the full dynamics analysis is not really full. (3) Both approximate and full analyses involve the idea of a *full repellor* as a set of the system itself. This concept is unclear because repellors are functions of the outcomes, and therefore are sets that are defined only after the definition of the outcomes. The origin of the problem seems to be in some confusion between nonattracting invariant sets (repellors) and the set of periodic points.

When considered the above oversights, the CL's work becomes inconclusive. In spite of that, the authors left a great contribution: the suggestion of using fractal invariant methods to investigate the mixmaster model. (Coordinate-dependent fractal techniques were introduced by Demaret and De Rop [11] to study an approximation of the Bianchi IX cosmology.) In this communication we will follow this idea as close as possible of the CL's work in order to allow a direct comparison by the reader. But different from CL, we will choose the box-counting dimension as the invariant indicator of chaos [9]. The topological entropy and the information dimension, employed by CL, are unsuitable indicators of chaos in the mixmaster system: the topological entropy is a function of the time parametrization because of its dependence on the period of the periodic points; the information dimension is difficult to be computed since it is difficult to verify the optimal condition mentioned above (we stress that CL were not able to obtain such dimension in the case of the full dynamics). The box-counting dimension, on the other hand, is diffeomorphism invariant and can be easily computed by applying the uncertainty exponent method [9].

The Einstein equations expressed in terms of the three spatial scales of the model (g_{ij}) =diag(a^2, b^2, c^2) lead to the motion equations [1]

$$(\ln a^2)'' = (b^2 - c^2)^2 - a^4, \quad et \;\; cyc., \tag{G.1}$$

together with the constraint equation

$$(\ln a^2)'(\ln b^2)' + 2a^2b^2 - a^4 + cyc. = 0. \tag{G.2}$$

A prime denotes $d/d\tau$, where $dt = abc\, d\tau$ and t is the cosmological time. It is convenient to introduce α_1, α_2 and α_3 as $\alpha^{(a)} = \ln a$, $\alpha^{(b)} = \ln b$ and $\alpha^{(c)} = \ln c$ in increasing order of the time derivatives. That is, $\dot\alpha_1 \leq \dot\alpha_2 \leq \dot\alpha_3$, where a dot denotes $d/d\Omega$ and Ω is the time $\ln(abc)/3$. The dynamics near the cosmological singularity is approximated by the CB map [10], obtained from a parametrization of the surface of section $\alpha_\kappa = 0, \dot\alpha_\kappa > 0$ by

$$\begin{array}{lll} \alpha_1 = 3\Omega q_1(u,v), & \alpha_2 = 3\Omega q_2(u,v), & \alpha_3 = 3\Omega q_3(u,v), \\ \dot\alpha_1 = 3p_1(u), & \dot\alpha_2 = 3p_2(u), & \dot\alpha_3 = 3p_3(u), \end{array} \tag{G.3}$$

where $q_1 = 1/(1+v+uv)$, $q_2 = \delta_{\kappa 3}(v+uv)/(1+v+uv)$, $q_3 = \delta_{\kappa 2}(v+uv)/(1+v+uv)$, $p_1 = -u/(1+u+u^2)$, $p_2 = \delta_{\kappa 2}(1+u)/(1+u+u^2) + \delta_{\kappa 3}(u+u^2)/(1+u+u^2)$ and $p_3 = \delta_{\kappa 2}(u+u^2)/(1+u+u^2) + \delta_{\kappa 3}(1+u)/(1+u+u^2)$, for $0 \leq u, v < \infty$. The evolution of the parameters u and v is then determined by the Farey map[1]

$$F(u,v)=\begin{cases}(u-1,v+1)\,, & \text{if } u\geq 1 \text{ (change of epoch)},\\ (u^{-1}-1,(v+1)^{-1})\,, & \text{if } u<1 \text{ (change of era)}.\end{cases} \tag{G.4}$$

The scale factors[2] $(\alpha_1,\alpha_2,\alpha_3)=(\alpha^{(\mu)},\alpha^{(\nu)},\alpha^{(\rho)})$ evolve as $\dot{\alpha}_1\leq\dot{\alpha}_2\leq\dot{\alpha}_3\longmapsto\dot{\tilde{\alpha}}_1\leq\dot{\tilde{\alpha}}_2\leq\dot{\tilde{\alpha}}_3$, where $(\tilde{\alpha}_1,\tilde{\alpha}_2,\tilde{\alpha}_3)=(\alpha^{(\nu)},\alpha^{(\mu)},\alpha^{(\rho)})$ and $\kappa=2$ except in the transition to the last epoch of each era, where $(\tilde{\alpha}_1,\tilde{\alpha}_2,\tilde{\alpha}_3)=(\alpha^{(\nu)},\alpha^{(\rho)},\alpha^{(\mu)})$ and κ becomes 3.

First let us consider the approximate dynamics in order to have some insight into the problem. In taking relative quantities in (G.3), the overall scale factor Ω is canceled, and we are led to a stationary phase space $u\times v$ where three outcomes can be identified: $(u,\alpha_3)=(\infty,\alpha^{(a)})$, $(u,\alpha_3)=(\infty,\alpha^{(b)})$ and $(u,\alpha_3)=(\infty,\alpha^{(c)})$. Since only rational values of u are led to these outcomes by forward iteration of the map, the corresponding invariant set contains almost every point of the phase space and it tells us nothing about chaos. However, some useful conclusions can be obtained if we enlarge the outcomes. It is made by defining the three outcomes for $u>u_{out}-1$ instead of $u=\infty$, which transform the system in an exit (scattering) system (the original Farey exit map was defined by CL [6]). These outcomes are equivalent to $\dot{\alpha}_3/(\dot{\alpha}_1+\dot{\alpha}_2+\dot{\alpha}_3)>\hat{p}_3(u_{out})$, where $\hat{p}_3(u)=(u+u^2)/(1+u+u^2)$. The dynamics of this exit system is determined by a nonattracting invariant set - the repellor [9]. The repellor is a zero measure set consisting of a countable number of unstable periodic orbits surrounded by an uncountable number of nonperiodic orbits. A fractional box-counting dimension for the repellor implies the exit system to be chaotic in the sense of having a chaotic transient: the system evolves chaotically for a period of time before being scattered. (This implication is of typical validity and includes the extreme case, when the box-counting

---

[1] The Farey map can be equivalently defined as

$$\bar{F}(u,v)=\begin{cases}(u-1,v+1)\,, & \text{if } u\geq 2 \text{ (change of epoch)},\\ \big((u-1)^{-1},v^{-1}+1\big)\,, & \text{if } u<2 \text{ (change of era)},\end{cases}$$

for $1\leq u,v<\infty$. Since $\bar{F}=f^{-1}oFof$ ($\bar{F}$ and F are conjugate), where $f(u,v)=(u-1,v-1)$, the parametrization corresponding to $\bar{F}$ is not just (G.3) (as used by CL) but (G.3) with q_i and p_i replaced by $\bar{q}_i=q_i of$ and $\bar{p}_i=p_i of$, for $i=1,2,3$.

[2] The indices μ,ν,ρ are permutations of a,b,c.

dimension of the repellor equals the phase space dimension. Pathological counterexamples can be constructed, but do not seem to represent realistic systems [12].) Concerning the original system, the system is typically never scattered (except for particular choices of the initial conditions) and hence it would evolve chaotically forever. Therefore, if the exit system is chaotic, the original system is also chaotic.

In Fig. G.1 we show, in three different colors, the basins of initial conditions for the outcomes defined by $u_{out} = 7$ (the same used by CL [6]). It can be shown that magnifications of the basin boundary lead to figures with the same complex structure of Fig. G.1, where the three colors (basins) are always present. The basin boundary is the future invariant set, and its box-counting dimension estimated from the uncertainty exponent method [9] results $D_0 = 1.87 \pm 0.01$. Since the repellor is the intersection of the future and the past invariant sets, it is equivalent to study any one of these sets. We prefer the future invariant set because of its easier geometric interpretation. Therefore, the above result for D_0 is enough to conclude that the original map is chaotic. In varying the outcomes, D_0 becomes an increasing function of u_{out} as showed in Fig. G.2. When the outcomes are made arbitrarily small, D_0 approaches 2. The behavior is completely different in a nonchaotic system, since in that case D_0 is integer and does not approach the phase-space dimension when the outcomes are reduced.

Now we repeat the procedure for the full dynamics. In order to allow comparisons with the approximate study, we take the initial condition defined by (G.3) for $1 < u, v < 2$ ($\kappa = 2$), $\mathrm{d}\Omega/\mathrm{d}\tau = 1$, and Ω the negative solution of the constraint equation. The integration is performed in the negative direction of Ω (approaching the singularity). Since u is not well defined during the integration, the best choice for the outcomes is $\dot{\alpha}_3/(\dot{\alpha}_1 + \dot{\alpha}_2 + \dot{\alpha}_3) > \hat{p}_3(u_{out})$. In the limit $\Omega \to -\infty$ these outcomes correspond to those defined for the Farey map. The full dynamics is, however, considered for a continuous time and the outcomes are defined not only on a surface of section. In Fig. G.3 we show the basins of initial conditions for $u_{out} = 7$. Fig. G.3 must be compared with Fig. G.1. Small differences between these figures were expected, since the latter is an asymptotic approximation while the former is exact and refers to initial conditions taken near the maximum of expansion.

The complicated structure of Fig. G.3 is also present in any magnification of the basin boundary - see Fig. G.4, where we show a 100 times magnification of Fig. G.3. The numerical computation of the box-counting dimension corresponding to $u_{out} = 7$ results $D_0 = 1.87 \pm 0.01$, consistent with the approximate value. In fact, the differences between the approximate and the full fractal dimensions are quite small, as can be seen in Fig. G.2. Moreover, the system has the so called Wada property [13]: every point on the boundary of a basin is also on the boundary of the other two basins. The corresponding fractal figures of CL do not present this property [6].

The mixmaster equations were integrated with a fifth-order adaptative stepsize Cash-Karp Runge-Kutta code [14]. The stepsize-control parameters employed in these computations were chosen so that the same results are reproduced under further increases of accuracy. This integration was also tested by checking the agreement of the results with those produced by the symplectic integration algorithm presented in Ref. [15].

From the above analysis follows that the mixmaster dynamics is in fact chaotic. This conclusion is independent of the particular space-time parameters used because D_0 is invariant under space-time diffeomorphisms. The numerical values obtained for D_0 depend on the choices made for the outcomes. But, once found a set of outcomes for which the resulting D_0 is fractional and goes to the phase space dimension in the limit "outcomes $\to 0$", the system is unequivocally chaotic.

The authors thank R.R.D. Vilela and M.T. Ujevic for their valuable comments, and also Fapesp and CNPq for financial support.

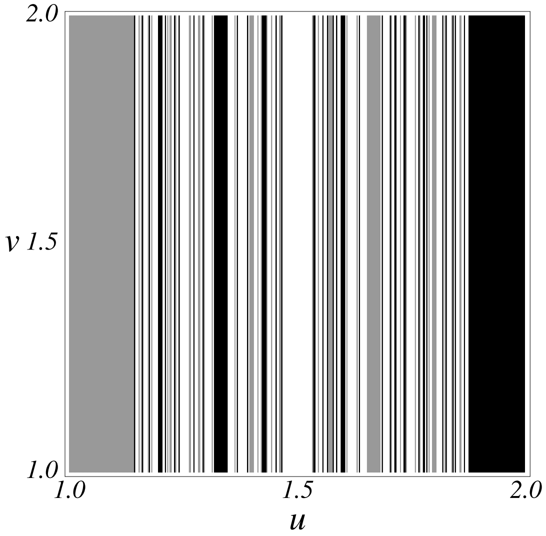

Figure G.1: Portrait of the basins of the approximate dynamics for $u_{out} = 7$. The initial conditions were chosen on a grid of 400×400, for $\alpha_1 = \alpha^{(a)}$, $\alpha_2 = \alpha^{(b)}$ and $\alpha_3 = \alpha^{(c)}$. Regions in gray, black and white correspond to orbits that escape for $\dot{\alpha}_3/(\dot{\alpha}_1 + \dot{\alpha}_2 + \dot{\alpha}_3) > 56/57$ with $\alpha_3 = \alpha^{(a)}$, $\alpha_3 = \alpha^{(b)}$ and $\alpha_3 = \alpha^{(c)}$, respectively.

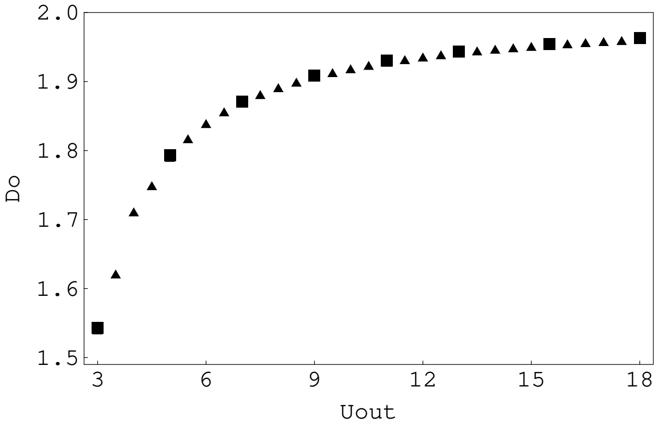

Figure G.2: Box-counting dimension (D_0) of the basin boundary (future invariant set) as a function of the outcome parameter (u_{out}) for: (a) approximate dynamics (triangles); (b) full dynamics (squares). The size of the triangles and squares corresponds approximately to the statistical uncertainty of D_0.

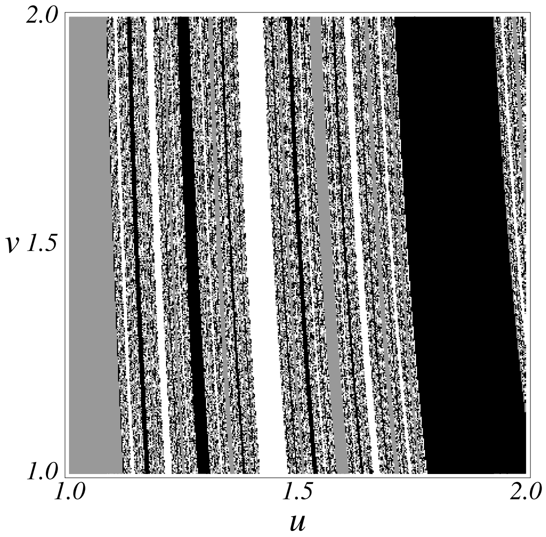

Figure G.3: Portrait of the basins of the full dynamics for $u_{out} = 7$. The initial conditions were chosen on a grid of 400×400, for $\alpha_1 = \alpha^{(a)}$, $\alpha_2 = \alpha^{(b)}$ and $\alpha_3 = \alpha^{(c)}$. Regions in gray, black and white correspond to orbits that escape for $\dot{\alpha}_3/(\dot{\alpha}_1 + \dot{\alpha}_2 + \dot{\alpha}_3) > 56/57$ with $\alpha_3 = \alpha^{(a)}$, $\alpha_3 = \alpha^{(b)}$ and $\alpha_3 = \alpha^{(c)}$, respectively.

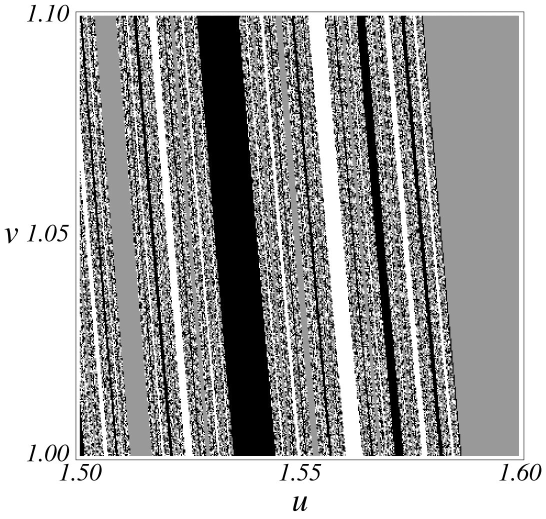

Figure G.4: A 100 times magnification of a portion of Fig. G.3.

Bibliography

[1] V.A. Belinskii, I.M. Khalatnikov, and E.M. Lifshitz, Adv. Phys. **19**, 525 (1970).

[2] C.W. Misner, Phys. Rev. Lett. **22**, 1071 (1969).

[3] *Deterministic Chaos in General Relativity*, edited by D. Hobill, A. Burd, and A. Coley (Plenum Press, New York, 1994).

[4] A. Burd, in: Ref. [3]; G. Contopoulos, B. Grammaticos, and A. Ramani, J. Phys. A **28**, 5313 (1995).

[5] M. Szydlowski and A. Lapeta, Phys. Lett. A **148**, 353 (1990); M. Szydlowski and A. Krawiec, Phys. Rev. D **53**, 6893 (1996).

[6] N.J. Cornish and J.J. Levin, Phys. Rev. Lett. **78**, 998 (1997); N.J. Cornish and J.J. Levin, Phys. Rev. D **55**, 7489 (1997).

[7] P. Holmes, Phys. Rep. **193**, 137 (1990).

[8] J.D. Farmer, E. Ott, and J.A. Yorke, Physica D **7**, 153 (1983).

[9] E. Ott, *Chaos in Dynamical Systems* (Cambridge University Press, Cambridge, 1994).

[10] D.F. Chernoff and J.D. Barrow, Phys. Rev. Lett. **50**, 134 (1983); B.K. Berger, Phys. Rev. D **49**, 1120 (1994).

[11] J. Demaret and Y. De Rop, Phys. Lett. B **299**, 223 (1993).

[12] G. Troll, Chaos Soliton Fract. **7**, 1929 (1996).

[13] D. Sweet, E. Ott, and J.A. Yorke, Nature **399**, 315 (1999).

[14] W.H. Press, S.A. Teukolsky, W.T. Vetterling, and B.P. Flannery, *Numerical Recipes in Fortran: The Art of Scientific Computing - 2nd* ed. (Cambridge University Press, Cambridge, 1997).

[15] B.K. Berger, D. Garfinkle, and E. Strasser, Class. Quantum Grav. **14**, L29 (1997).

FRW cosmologies between chaos and integrability

H

Adilson E. Motter, Patricio S. Letelier, Physical Review D **65**, 068502 (2002).

A recent paper by Castagnino, Giacomini and Lara concludes that there is no chaos in a conformally coupled closed Friedmann-Robertson-Walker universe, which is in apparent contradiction with previous works. We point out that although nonchaotic the quoted system is nonintegrable.

PACS numbers: 04.62.+v, 98.80.-k.

Castagnino, Giacomini and Lara (CGL) [1] analyzed the dynamical evolution of the spatially closed Friedmann-Robertson-Walker (FRW) cosmology conformally coupled to a massive, real, scalar field. Employing the cosmological time as the time parameter, they show that for arbitrary initial conditions the universe will collapse in a finite time and with a divergent rate of contraction. Their conclusion is that there is no chaos in the model.

The same system had been previously considered by Calzetta and El Hasi [2], who presented evidence of chaotic behavior subsequently confirmed by Bombelli, Lombardo and Castagnino [3]. Since these authors employed the conformal time in their analyses, CGL argue that the discrepancy of the results would rely on the different time parameters used – the origin of an intensive debate in the paradigmatic mixmaster model [4]. The aim of this note is to show that this is not the case and that all these fine works are in complete agreement in spite of the different choices of coordinates.

The classical theory of dynamical systems regards the study of systems of the form

$$\frac{d\mathbf{x}}{dt} = \mathbf{F}(\mathbf{x}), \tag{H.1}$$

for a fixed choice of the time parameter t. An invariant set of the phase space $\mathbf{x}$ is chaotic if it presents a *sensitive dependence on initial conditions and mixing*. This characterization is invariant under space diffeomorphisms: $\mathbf{y} = \psi(\mathbf{x})$. In general relativity, the absence of an absolute time forces us to consider system (H.1) under space-*time* diffeomorphisms: $\mathbf{y} = \psi(\mathbf{x}, t)$, $d\tau = \lambda(\mathbf{x}, t)dt$. Usually, the dynamical variables in this context are either functions of the space-time coordinates x^μ (possibly together with spins, Euler angles, etc.), when we study motions in a given background geometry, or functions of the metric $g_{\mu\nu}$ (possibly together with other fields), when we consider the evolution of the geometry itself. The study of chaos in general relativity faces both conceptual and technical difficulties. The former are associated with the dependence of classical indicators of chaos on the choice of the time parameter. This problem has been intensively discussed in the literature since Francisco and Matsas [5] showed the coordinate dependence of Lyapunov exponents. The latter difficulties are related with characteristic properties of relativistic systems. In cosmology, for example, we often meet high dimensionality, noncompacity, nonpositive kinetic energy, non-normalizable measure, nonexistence of global coordinates, nontrivial topology, singularities, etc. These properties strongly restrict the practical use of standard indicators of chaos, even if the system is treated as a classical one. The second class of difficulties is in fact the origin of most of the problems concerning chaos in cosmology, including the one discussed in this communication.

In terms of the conformal time η the system considered by CGL [1] is modeled by the $H = 0$ energy surface of the Hamiltonian

$$2H = -p_a^2 + p_\phi^2 - a^2 + \phi^2 + a^2\phi^2, \tag{H.2}$$

where a is the radius of the universe and ϕ is the reparametrized scalar field [6]. CGL proved that the dynamics is nonchaotic *if* formulated in terms of the cosmological time. Our first point is that this is also true when the dynamics is formulated in terms of the conformal time as well as in terms of any other well defined time parameter. Translating the CGL work into conformal time it follows that for every physical initial condition, $a > 0$ at $\eta = 0$, there will be a finite time η_1 such that $a \to 0$ and $a' \to C$ for $\eta \to \eta_1$, where the prime denotes $d/d\eta$ and C is a nonzero, negative, finite constant. The absence of physical meaning for a negative universe radius, $a < 0$, prevents us from extending the solutions beyond the big crunch. Since chaos is a concept associated with an infinite number of recurrences, it is clear that (H.2) regarded as a cosmological system is nonchaotic. To see the generality of this statement we can consider the Ricci scalar

$$\frac{R}{6} = m^2 \left(\frac{\phi}{a}\right)^2, \tag{H.3}$$

where m is the mass of the coupled field. From Eq. (H.2) we have $\phi'^2 + \phi^2 \to C^2$ when $a \to 0$ and $a' \to C$, which leads to two possibilities: $R \to 6m^2$ if $\phi \to 0$, and $R \to \infty$ if $\phi \to \phi_1 \neq 0$. It is easy to see from a Poincaré section defined by $a = 0$, $a' < 0$ that ϕ is typically nonzero at the big crunch, resulting in a divergent behavior for R. Such singularity is coordinate invariant and forbids physical extensions of the solutions throughout the big crunch, whatever coordinates we use.

Since there is no chaos the next question is whether or not the system is integrable. The answer comes from Refs. [2, 3], where it is shown that the universe would present chaotic regions in the phase space (p_a, p_ϕ, a, ϕ) for an *infinite* sequence of contractions and expansions [7]. This extension through $a < 0$ has no physical meaning, as mentioned before, but is an ingenious mathematical trick to obtain properties in the physical region from properties in the extended, unphysical domain. For example, chaos in the extended domain implies nonintegrability. In particular, it implies nonintegrability in the physical region defined by the first half-cycle $a > 0$, between a big bang and the following big crunch. We stress that, even though the extension of the dynamics beyond the big crunch can be performed in the conformal time formulation and not in the cosmological time approach (because of the divergence of the contraction rate), the result concerning nonintegrability in the physical region is invariant under coordinate changes. In fact, the relation between the cosmological time and the conformal time in the physical domain is $dT = ad\eta$, which is a particular case of an *autonomous* transformation of the form

$$\mathbf{y} = \psi(\mathbf{x}), \tag{H.4}$$

$$d\tau = \lambda(\mathbf{x})dt, \tag{H.5}$$

where λ is a positive function and ψ is a diffeomorphism. The integrability is coordinate invariant under this class of transformations because if $\{I_1, I_2, ...\}$ are independent integrals of motion in the original variables $(\mathbf{x}, t)$ (i.e., $\mathbf{F} \cdot \nabla I_i = 0$ and $\{\nabla I_1, \nabla I_2, ...\}$ are linearly independent) then $\{I_1 \circ \psi^{-1}, I_2 \circ \psi^{-1}, ...\}$ are independent integrals of motion in the variables $(\mathbf{y}, \tau)$. Therefore we can say that the conformally coupled FRW model (H.2) is nonintegrable in a meaningful sense. Accordingly, we cannot hope to find exact solutions for arbitrary initial conditions.

The same idea can be used to study the integrability of others FRW cosmologies, as long as we can find nonsingular coordinates to mathematically extend the solutions. In particular, this procedure works in the spatially closed cosmology conformally coupled to a scalar field, with both mass and cosmological constant terms, considered in Ref. [8]. Since it was shown that this model is chaotic in the extended domain, it follows that the system is nonintegrable in the physical region. We observe that methods based on extensions to unphysical values have been used for a long time to study integrability in cosmology. Perhaps the best known of them is the one based on the Painlevé theory of differential equations [9]. In the Painlevé analysis we look for necessary conditions for integrability (equivalently, sufficient conditions for nonintegrability) by studying critical points in the complex plane of time.

Summarizing, the dynamics of the model studied by CGL is chaotic when analyzed for an unphysical sequence of expansions and contractions of the universe, and is nonchaotic when considered for the period of time limited by a big bang and a big crunch. Nevertheless, it does not mean that the dynamics is simple since the onset of chaos in the extended domain implies nonintegrability in the physical region, which poses obstructions to the study of exact solutions. This characterization is coordinate invariant and does not rely on *natural* or *physical* choices of the time parameter, consistent with the covariant principle of general relativity.

A.E.M. thanks Y.-C. Lai for his kind hospitality at Arizona State University. This work was supported by Fapesp and CNPq.

Bibliography

[1] M.A. Castagnino, H. Giacomini, and L. Lara, Phys. Rev. D **63**, 044003 (2001).

[2] E. Calzetta and C. El Hasi, Class. Quantum Grav. **10**, 1825 (1993).

[3] L. Bombelli, F. Lombardo, and M.A. Castagnino, J. Math. Phys. **39**, 6040 (1998).

[4] A.E. Motter and P.S. Letelier, Phys. Lett. A **285**, 127 (2001).

[5] G. Francisco and G.E.A. Matsas, Gen. Relativ. Gravit. **20**, 1047 (1988).

[6] The dynamical variables have been rescaled by the mass of the field: $a \to a/m$ and $\phi \to \phi/m$.

[7] The analysis of Hamiltonian (H.2) is highly non-trivial because the kinetic energy $2K = -p_a^2 + p_\phi^2$ is not positive definite. We cannot find confined regions by analyzing the potential $2V = -a^2 + \phi^2 + a^2\phi^2$, what makes difficult the use of standard methods for chaos like Poincaré section and Lyapunov exponent methods. The authors of Refs. [2, 3] managed to apply Melnikov methods to study the effect of the coupled field. For small values of a and ϕ, the coupling term $a^2\phi^2/2$ is a small perturbation and only a small fraction of the Kolmogorov-Arnold-Moser (KAM) tori are destroyed. For large values of a and/or ϕ, the coupling term becomes significant and most of the KAM surfaces are destroyed, leading their orbits to access a higher dimensional region.

[8] E. Calzetta and C. El Hasi, Phys. Rev. D **51**, 2713 (1995).

[9] For example, G. Contopoulos, B. Grammaticos, and A. Ramani, J. Phys. A **28**, 5313 (1995); A. Helmi and H. Vucetich, Phys. Lett. A **230**, 153 (1997).